ABSTRACT

Title of Dissertation: THE INFLUENCE OF SURFACE GRAVITY WAVES ON THE PERFORMANCE AND NEAR-WAKE OF AN AXIAL-FLOW MARINE HYDROKINETIC TURBINE

Ethan Edward Lust, Doctor of Philosophy, 2017

Directed by: Professor James H. Duncan
Department of Mechanical Engineering

Surface gravity waves can significantly impact operating conditions for axial-flow marine hydrokinetic turbines, imparting unsteady velocities several orders of magnitude larger than the ambient turbulence. The complex interactions between the turbine and the wake, particularly in the presence of waves, are not well understood. Furthermore, detailed experimental data are needed for numerical model validation. Thus, the influence of surface waves on the performance and wake of a two-bladed axial-flow hydrokinetic turbine was investigated experimentally using an in-house designed and built towed Particle Image Velocimetry (PIV) system in the large towing tank facility at the U.S. Naval Academy. The turbine model has a 0.8 m diameter (D) rotor with a NACA 63_3-618 cross section that is Reynolds number independent with respect to lift coefficient in the operating range of $Re_c \approx 4x10^5$.

Performance measures (i.e. power and thrust) were taken for both the steady (no wave) and unsteady (wave) cases. Average performance parameter values for the unsteady case were found to closely match those of the steady case, regardless of selected wave parameters. However, instantaneous values were found to depart substantially from the mean value having significant implications for power quality and fatigue loading.

A wake survey was conducted under steady conditions to a downstream distance of 2D. Wake characteristics such as a decrease in the inflow velocity upstream of the turbine, wake expansion well-described by a 1/3 power law expression, a maximum velocity deficit of 2/3 the free stream velocity, and prominent turbine tip vortices were all observed. Methods developed for helicopter rotor analysis were applied to identify and characterize turbine tip vortices. Adjacent vortex filament interaction, thought to be the initial mechanism of wake break down and re-energization, was observed. A recently-developed vortex center averaging methodology was employed with new implications for the interpretation of turbulence statistics.

A wake survey was also conducted under unsteady conditions over a similar downstream range. Blade-phase averaging was shown to be a poor descriptor of wake characteristics. Blade and wave phase averaging offers a clearer picture of wake dynamics in the presence of waves. The unsteady velocities induced by the waves were shown to change the spatial characteristics of the tip vortex helix. The strong helical structure that characterizes the steady case to a distance of approximately 1D persists in the steady case, however, the unsteady vertical wave velocity appears to convect vortex filaments into the wake region, potentially enhancing kinetic energy transport and wake re-energization. A simple, potential flow-based model was proposed to simulate the behavior of the wake influenced by waves, and a parametric study employing the model provided insight as to what factors most significantly affect vortex filament position and the characteristic length scales of the wake. An additional length scale was proposed to describe the shear layer in the unsteady case and is shown to agree well with experimental observations.

THE INFLUENCE OF SURFACE GRAVITY WAVES ON THE PERFORMANCE AND NEAR-WAKE OF AN AXIAL-FLOW HYDROKINETIC TURBINE

By

Ethan Edward Lust

Dissertation submitted to the Faculty of the Graduate School of the
University of Maryland, College Park in partial fulfillment
of the requirements for the degree of
Doctor of Philosophy
2017

Advisory Committee:

Professor James H. Duncan, Chair
Professor Amir Riaz
Professor Johan Larsson
Professor Anya Jones
Professor James Baeder, Dean's Representative

DEDICATION

I was fortunate to have many exceptional teachers throughout my lengthy career as a student. One in particular will forever stand out in my memory. She changed my perceptions about what I was capable of and what I should expect from myself. I credit her with altering the trajectory of my academic career, thus altering the trajectory of my life.

Teresa Seim, thank you for caring enough to make me sit in the front row.

ACKNOWLEGEMENTS

I've come to see the pursuit of a doctorate as an apprenticeship. I can think of no one to whom I'd rather be apprenticed than Karen Flack. It gives me immense pleasure to reflect on the influence of her mentorship in everything I do. Many, many thanks.

I'd like to also thank Luksa Luznik who has been a tremendous teacher and collaborator – someone whose visceral love of fluid mechanics I deeply admire. I'm also profoundly grateful to Jim Duncan for being amenable to taking on a satellite student. His uncanny knack for making the casual suggestion which sent me into a months-long vision quest also led to some of the most thoughtful contributions to the current work.

I'll always be grateful to Jessica Walker, our visiting Fulbright scholar from Tasmania for showing me how to be a graduate researcher, Julio Barros for his many patient hours of PIV instruction and troubleshooting, and Joe Milluzo for his willingness to discuss the finer details of wake analysis and vortex hunting. Thanks also to Colin Ratcliffe for his assistance with the uncertainty analysis.

I'd like to thank the USNA hydrolab staff including John Zseleczky, Bill Beaver, Dan Rhodes, Mike Stanbro, Louise Wallendorf, and Mark Pavkov for the hundreds of hours they have invested in this project over the last six years. I'd also like to thank Brandon Stanley, Andrew Pullen, and the exceptional professionals in the USNA machine shop for their time and expertise in manufacturing the experimental apparatus.

Last but nowhere near least, I'd like to thank my darling and patient wife, Nicole for her good humor with regard to my ten-year graduate school odyssey, and our son James and our daughter Ella for spurring me on to finish.

TABLE OF CONTENTS

LIST OF FIGURES

LIST OF TABLES

Table 1: Nomenclature

a	Wave amplitude	α	Angle of attack (°)
	Induction factor: axial (a), angular (a')	$\delta_{1/2}$	Wake half width (m)
c	Blade chord (m)	$\delta_{BL,1.2}$	Shear layer half width (m)
C_D	Drag coefficient	δ_S	Maximum velocity deficit width (m)
C_L	Lift coefficient	δ_V	Steady mean vortex center width (m)
C_P	Power coefficient	δ_W	Wake width (m)
C_T	Thrust coefficient	ϵ	Mean rate of energy dissipation per
D	Turbine rotor diameter (m)	Γ	Circulation (m^2/s)
E_L	Wave energy per unit width (J/m)	γ	Specific weight (N/m^3)
g	Gravitational acceleration	η	Free surface elevation (m)
H	Wave height (m)	λ	Wavelength (m)
h	Depth (m)	μ	Absolute viscosity (kg·m/s)
I	Turbulence intensity	ν	Kinematic viscosity (m^2/s)
k	Wave number (s^{-1})	Ω	Turbine angular velocity (s^{-1})
L	Lift force (N)	ω	Wave angular frequency
L	Strut length (m)	ϕ	Angle of relative wind (°)
p_∞	Static pressure far upstream (Pa)	ϕ_b	Blade phase angle
p_v	Vapor pressure (Pa)	ϕ_w	Wave phase angle
p_{atm}	Atmospheric pressure (Pa)	ρ	Fluid density (kg/m^3)
Q	Torque (N·m)	σ	Wave angular frequency (s^{-1})
R	Blade radius (m)		Cavitation number
r	Element radius (m)	θ_P	Section blade pitch (°)
r_a	Aperiodicity	$'$	Fluctuating
r_c	Vortex core radius	$\bar{}$	Time average
Re_c	Reynolds number based on blade	$< >$	Phase average
S	Signal	$\tilde{}$	Periodic
T	Thrust (N), wave period (s)		
t	Time (s)		
	Student's-t statistic		
TSR	Tip speed ratio		
u	Horizontal velocity (m/s)		
	Elemental or standard uncertainty		
V_θ	Vortex swirl velocity (m/s)		
U	Uniform flow speed (m/s)		
	Expanded uncertainty		
U_{tow}	Towing carriage speed		
U_{rel}	Relative velocity (m/s)		
U_s	Velocity deficit (m/s)		
w	Vertical velocity (m/s)		
x	Horizontal or streamwise coordinate		
x_c	Vortex center x-coordinate (m)		
z	Vertical coordinate (z = 0 at free surf.)		
z_c	Vortex center z-coordinate (m)		

1 Introduction

According to Hermann [1], approximately 3.7 TW of tidal exergy is dissipated worldwide, 2.5 TW of which is dissipated in the shallow ocean and continental shelves. Current dissipation as a consequence of collection for energy services amounts to approximately 500 MW (0.014%). In addition to being abundant, tidal exergy is clean and sustainable.

A number of technologies have been developed to collect tidal exergy of which axial-flow (also called horizontal-axis) hydrokinetic turbine technology is the most mature based on total installed capacity [2]. Still, the amount of exergy collected is quite small compared to the considerable size of the resource. The primary reason for this is the current high relative cost of electricity as compared with other, more traditional, technologically-mature sources.

In an effort to spur development of marine hydrokinetic turbine technology and reduce the associated cost of electricity, the U.S. Department of Energy developed and promulgated six open-source marine hydrokinetic energy converter devices, including Reference Model 1 (RM1) a tidal current turbine, shown in Figure 1 and described in

Table 2. It called for industry, academic, and national lab partners to create open-source products including the development and dissemination of physical model data sets for validating design modeling tools [3]. These tools could then be used to predict turbine performance, reducing the uncertainty associated with design and development, thereby reducing the cost of implementation, and thus making the technology more cost-competitive.

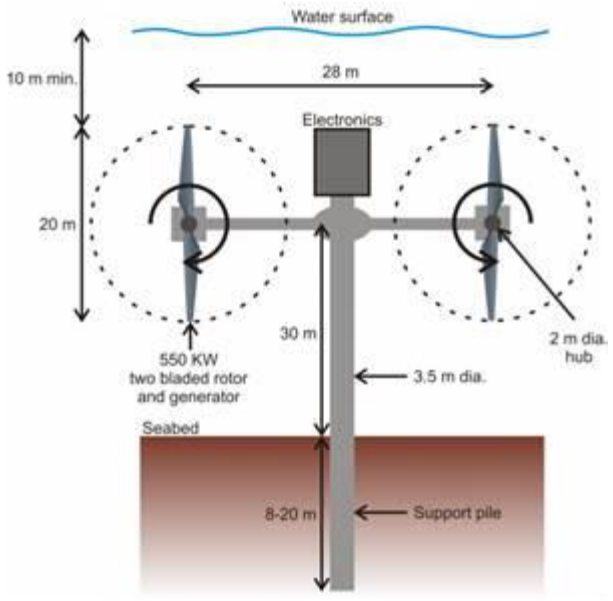

Figure 1: Reference Model 1 (RM1) promulgated by the U.S. Department of Energy [4].

Table 2: Reference Model #1 Tidal Turbine Specifications [4]

Number of blades	2
Primary blade airfoil	NACA 63_1 – 424
Rated power (kW)	550
Control	Variable speed and pitch
Rotor diameter (m)	20
Hub diameter (m)	2
Maximum rotor speed (rpm)	11.5
Flow speed (m/s)	0.5-3.0
Hub height (m)	18
Water depth (m)	33

Large scale implementation of hydrokinetic devices will require sites with an array of turbines. One of the major unanswered questions is where to position multiple turbines in an array arrangement in order to maximize power production while minimizing loading. To answer this question, the turbine wake must be characterized as the spacing and

orientation of adjacent turbines is primarily dependent on the state of the flow immediately upstream of each respective turbine.

Much of axial-flow hydrokinetic turbine research is informed by previous work on wind turbines. However, there are phenomena unique to the subsurface marine operating environment that have no direct analogy to the terrestrial environment: cavitation, the effect of the free surface above the turbine, and the unsteady velocity associated with surface waves, to name a few examples. Given the considerable difference in the density of the operating medium, the corrosive character of seawater, challenges associated with maintenance and repair, and the fatigue loading caused by variable inflow conditions, the material requirements for marine current turbines are significant. Given these considerations it is clear that characterization of the operating environment and flow field around these devices is necessary for their wide-spread adoption as a commercially viable energy resource.

The format of the following discussion reflects the step-wise evolution of the project. Chapter 2 details development of the experimental apparatus and establishment of operating conditions. It presents baseline performance characteristics for comparison to follow-on experiments. Chapter 3 compares turbine performance under steady conditions to performance in unsteady conditions. Like Chapter 2, Chapter 4 describes the development of the experimental apparatus, presents observations made under steady conditions - in this case, the velocity field in the near wake of the turbine. Like Chapter 3, Chapter 5 compares observations made under steady conditions to those made under unsteady conditions. Chapter 6 summarizes the conclusions from each of the preceding chapters and includes a discussion of the significant contributions of the work.

2 Turbine performance testing in steady conditions

2.1 Abstract

In an effort to promote the development and implementation of marine hydrokinetic energy technology, the U.S. Department of Energy promulgated Reference Model (RM1), a tidal current turbine similar in form and operation to a horizontal-axis wind turbine. A 1/25th scale model based on this design was created at the U.S. Naval Academy and tested in the large towing tank facility in order to characterize the turbine's baseline experimental performance. The model was a two-bladed, 0.8 m diameter rotor featuring a NACA 63-618 airfoil cross-section that is shown to be Reynolds number independent with respect to lift coefficient in the operating range of $Re_c \approx 4 \times 10^5$. Rotational speed, torque, and thrust were measured at a range of tip speed ratios (TSR) from approximately 6 to 11. Experimental data compared favorably with previous studies. The impact of blockage and operating depth was assessed, the likelihood of cavitation was considered, and an uncertainty analysis was conducted. Additionally, a Blade Element Momentum (BEM) model was created, and model predictions were found to be in agreement with experimental observations.

2.2 Introduction

Axial-flow marine hydrokinetic turbines convert the power of flowing water from sources such as rivers, tidal currents, or global-scale currents such as the Gulf Stream into rotational mechanical power and ultimately into electricity. A brief explanation of the process is given in [5] depicted in Figure 2, and is summarized as follows.

As the flow approaches the turbine from upstream it slows slightly[1], increasing the static pressure (shown as p_s in Figure 2) directly in front of the turbine, thus the velocity that the turbine experiences is lower than the velocity of the surrounding free stream. The flow is incompressible, thus it must expand to accommodate the slower moving flow. The flow that interacts with the turbine can be thought of as a streamtube, with an initial diameter smaller than the diameter of the turbine, D but expanding to be equal to the diameter of the turbine at the rotor disk. As the flow passes through the turbine, a change in the momentum of the flow is manifest as lift and drag force[2] on the blades. As the kinetic energy of the flow is converted, in part, to the rotational kinetic energy of the turbine, the average velocity across the streamtube continues to decrease and there is a significant drop in the static pressure, reaching a minimum directly downstream of the turbine. The static pressure recovers by further reducing the average wake velocity, U_w thus causing the wake to expand further. Wake expansion ceases when the static pressure in the wake has recoved to its far upstream value.

[1] The flow upstream of the turbine slows because the flow in the immediate upstream vicinity of the turbine is being directed from the axial direction to the tangential direction in order to conserve angular momentum. This is manifest upstream as a blockage, reducing inflow velocity and increasing static pressure.

[2] The lift and drag, components of the resultant force associated with aerodynamics or in this case hydrodynamics, are simply coordinate transforms of thrust and tangential force (torque when applied at some distance from the axis of rotation) more readily associated with mechanical power.

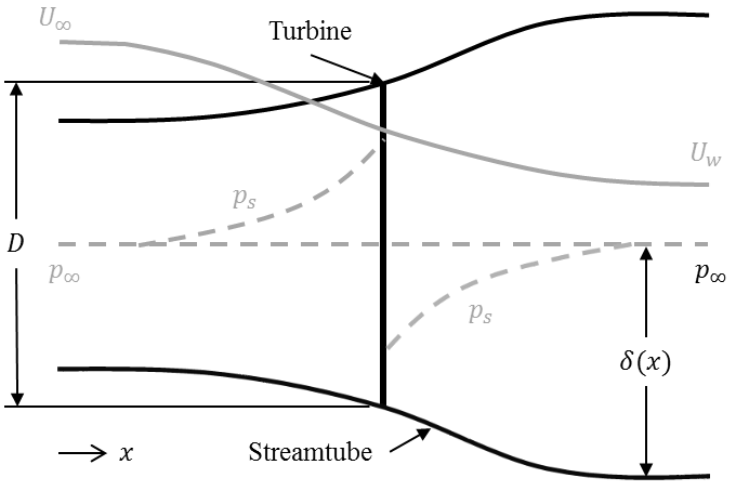

Figure 2: An energy extracting actuator disk (turbine) and stream tube (adapted from [5]).

Experimental turbine performance is generally characterized by the power coefficient:

$$C_p = \frac{P}{\frac{1}{2}\pi\rho U^3 R^2} \tag{1}$$

or the ratio of the power produced by the turbine, P to the power contained in a cylinder of water the same radius as the turbine, R flowing at a free stream speed, U. The turbine power, is equal to the torque on the turbine output shaft, Q multiplied by the rotation speed, Ω. Derived from dimensional analysis, the power coefficient is used to predict how much power a full-scale turbine would produce under given conditions, assuming complete similitude. Similarly, the thrust coefficient:

$$C_T = \frac{T}{\frac{1}{2}\pi\rho U^2 R^2} \tag{2}$$

is used to predict the thrust loading (the force acting perpendicular to the turbine rotation plane in the downstream direction) on a full-scale device.

These performance parameters are generally given as a function of the tip speed ratio:

$$TSR = \frac{R\Omega}{U} \tag{3}$$

or the ratio of the tangential speed of the turbine tip, $R\Omega$ to the free stream speed.

As stated in the introduction, the basis for nearly all marine current turbine research comes from research associated with the development of wind turbines. The classical analysis for wind turbines, itself based on the study of airplane propellers, was developed by Betz (included later in [6]) and advanced by Glauert [7, 8] in the early part of the twentieth century. In 1974, Wilson and Lissaman [9] developed Blade Element Momentum (BEM) theory, including an appendix detailing FORTRAN implementation.

BEM theory, also called strip theory, is a combination of momentum theory and blade element theory. A detailed treatment of the theory is presented in Manwell et al. [10] but is summarized here.

Momentum theory uses conservation of linear and angular momentum over the control volume surrounding the turbine (i.e. the streamtube) to determine the differential thrust dT and differential torque dQ as functions of the axial induction factor a and the angular induction factor a'. The blade is divided into elements which are normal to the span of the blade and extend radially from the blade root to tip. Essentially, each element is an airfoil with unit thickness dr. At each of these elements, or *strips*, the forces are resolved to determine the differential normal force (thrust) dF_N and the differential tangential force at radius r, dQ (torque) as a function of the angle of the relative wind ϕ, the lift coefficient C_L, and the drag coefficient C_D (Figure 3). For airfoils used in wind

turbine design $C_D \ll C_L$, thus accepted practice is to set the drag coefficient to zero when solving for the induction factors which introduces negligible errors according to Manwell. The four equations are combined into a single equation from which the lift coefficient for a blade element can be calculated in terms of the relative wind angle. Since the relative wind angle is the sum of the angle of attack α and the pitch angle for the element θ_P which is known from the blade geometry, the lift coefficient can be plotted as a function of the angle of attack.

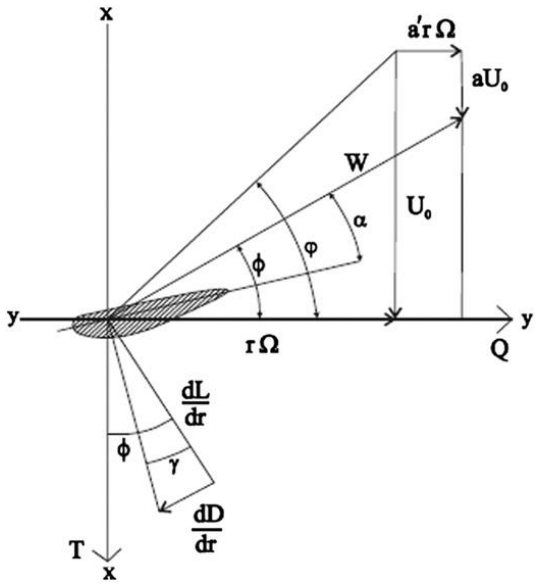

Figure 3: Hydrodynamic component forces and velocities on a blade element [11]. The mean flow direction is from top to bottom and the blade travels from right to left (clockwise when viewed from upstream).

This curve is overlaid with the empirical lift coefficient versus angle of attack curve for the airfoil section and the intersection of the two curves provides the angle of attack and lift coefficient for that blade element under the specified flow conditions. This allows for the back-calculation of the axial and angular induction factors and the differential thrust and torque. Once the differential thrust and torque values are known for each element, they

can be integrated over the radius of the blade to calculate the power and thrust coefficient for a given tip speed ratio.

Since empirical data is not available for every imaginable airfoil shape, it is also accepted practice to use an experimentally validated airfoil analysis tool such as XFOIL [12], a 2-D panel code with viscous boundary layer analysis, to provide the required lift coefficient as a function of angle of attack.

Correction factors have been developed to account for tip losses which are dependent on the number of blades, and hub losses which correct for flow around the nacelle (see Koh and Ng [13] for a review). Modifications have also been proposed to correct for the impact of biofouling [14], free-surface proximity and blockage [15], and the influence of waves [16, 17].

2.2.1 Literature review

Built upon nearly a century of horizontal-axis wind turbine research, a formidable foundation of literature specific to axial-flow marine hydrokinetic turbines has been established in the past two decades. Fraenkel [18] laid much of the groundwork for follow-on studies, summarizing the terminology and parameters used to describe turbine performance, comparing several types of marine hydrokinetic devices, estimating the recoverable energy, and comparing it to other renewable energy sources. To this, Bahaj and Myers [19] added a brief discussion of material requirements, maintenance considerations, and cavitation considerations.

Baseline performance tests were conducted for several variations of axial-flow hydrokinetic turbine [11, 20, 21, 22]. All turbines had either two or three blades

representing a trade-off between performance and durability[3]. Various airfoil cross-sections were chosen though most featured a thicker cross-section such as a NACA 6-series airfoil selected to withstand the considerably higher bending loads of the marine environment as compared to the terrestrial environment. Neither the number of blades nor the airfoil shape appeared to have much effect on the maximum performance, with peak C_P generally falling between 0.4 and 0.45.

Many of the baseline performance studies also compared experimental observations to BEM models predictions [14, 23, 24]. Predictions of C_P and C_T versus TSR generally agree well with experimental data, particularly in the region of peak performance. However, BEM theory tends to over-predict the power coefficient and under-predict the thrust coefficient at tip speed ratios above those associated with the peak power coefficient.

The impact of many permutations of turbine configuration and operating condition have also been examined. The turbine blade itself is generally designed with an optimization tool specifically intended for the task such as the U.S. National Renewable Energy Laboratory's HARP_Opt[4] or an in-house designed optimization algorithm. The resulting blade is typically both twisted (i.e. the pitch angle changes with blade radius) and tapered (i.e. the blade chord length changes with blade radius). Additionally, the effect of changing the base or root blade pitch (i.e. the angle at which the blade is attached to the turbine hub) on turbine performance has been examined in several studies [20, 21, 25].

[3] Turbine performance is impacted most significantly by solidity, or the total planform area of the turbine blades divided by the swept area of the turbine. A low solidity turbine (i.e. one that has fewer and/or smaller blades) produces moderate power but over a larger range of TSR values. A high solidity turbine (i.e. one that has more and/or larger blades) produces high power but over a comparatively narrow range of TSR values. As fewer, larger blades tend to be stronger, optimum solidity is often sacrificed for the sake of durability.

[4] Horizontal Axis Rotor Performance Optimization

Though the resulting performance depends on a number of factors such as blade geometry and model scale, generally speaking, there is an optimum root pitch angle at which the turbine achieves maximum performance. Again, regardless of the airfoil shape or the number of blades, this is typically in the range of $0.4 < C_P < 0.45$.

The impact of yaw, or the angle between the turbine axis of rotation and the free-stream flow, on turbine performance has also been examined [20, 21]. Turbine performance is shown to decrease considerably as the yaw angle increases, indicating that if possible, turbines should be designed to *weathervane* to minimize yaw angle.

As proposed, RM1 includes two counter-rotating turbines mounted to a single support pile, thus the impact of an adjacent rotor was also examined. Bahaj et al. [21] found there was no measureable interference between adjacent turbines operating as close as 0.125D measured from blade tip to blade tip.

2.2.2 Present work

The work presented in this section was published in Lust et al. [26]. The purpose of this preliminary portion of the overall research effort was to characterize the performance of the turbine, particularly in preparation for follow-on experiments. A BEM model was created, as previously described, and model predictions were compared to experimental observations. Experimental observations were also compared to the results from previous studies for verification and comparison. Operating parameters, such as minimum required operating depth, were determined as was the potential for cavitation. Finally, a detailed uncertainty analysis was conducted to identify potential opportunities for modification and improvement of the test equipment.

2.3 Experimental details

2.3.1 The Large Towing Tank Facility

Experiments were conducted in the large towing tank at the U.S. Naval Academy which measures 116 m long, 7.9 m wide, and 4.9 m deep (Figure 4). The tank features a dual-flap, servo-controlled wave maker capable of producing waves at a frequency range of 0.25 to 1.25 Hz with a maximum amplitude of 0.6 m. All experimental and data acquisition equipment was mounted to the towing carriage which has a maximum tow speed of 9.75 m/s.

Figure 4: The 380 ft. (116 m) towing tank at the U.S. Naval Academy

2.3.2 Turbine Blades

The turbine used in this experiment is a 1/25th scale, two-bladed axial-flow design measuring 0.8 m in diameter based on RM 1, promulgated by the U.S. Department of Energy (Figure 5). The blade diameter was selected to maximize the Reynolds number, as calculated using the 0.7R chord, and remain within dynamometer operating limitations. The blades are twisted from 13° at the root to 2° at the tip and tapered from a maximum chord length of 7 cm to a minimum of 2.5 cm. They were mounted just aft of a nacelle measuring 8 cm in diameter. The blades were manufactured at the U.S. Naval Academy using a 5-axis Computer Numerical Control milling machine from 6061-T6 Aluminum, selected for its excellent machinability and corrosion resistance. The blades were given a matte black anodized finish to provide contrast for imaging experiments.

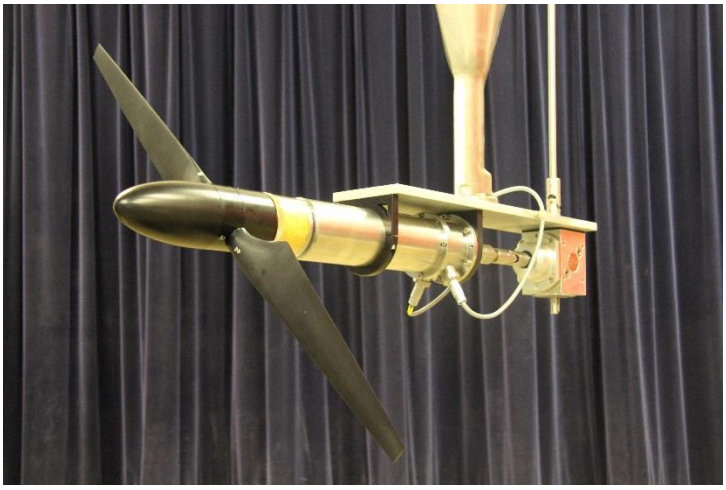

Figure 5:The two-bladed axial-flow marine hydrokinetic turbine used in the present experiment, shown mounted to the dynamometer with the data acquisition cables for thrust and torque protruding from below.

The turbine is a geometrically similar 1/25th scale model of RM1, with the exception of the airfoil shape. RM1 features a NACA 63_1-424 foil, whereas a NACA 63_3-618 was selected for this experiment for reasons discussed below.

Dynamic similarity for the model turbine is ideally achieved by matching the Reynolds number of the full size turbine because it most readily describes the flow around the turbine blades. For reference, the Reynolds number of RM 1, operating in a current of 0.5-3.0 m/s at a tip speed ratio of 7 is $2.5x10^6 – 1.5x10^7$. However, since few facilities with well-controlled flow conditions outside of field test facilities are capable of conducting experiments at this scale, reaching a Reynolds number sufficiently high to achieve independence is generally accepted as a satisfactory criterion for model similarity. In this case, independence is defined as the Reynolds number above which there is no observable change in integral performance characteristics. It should be noted that there appears to be little agreement in the literature as to what parameters to use in the calculation of the Reynolds number for a turbine. With regard to characteristic length, tip chord length, radius, and diameter are all used. Additionally, both hub velocity and relative velocity ($U_{rel} = \sqrt{U_{hub}^2 + (R\Omega)^2}$) at the blade tip are used to calculate Reynolds number. This makes direct comparison between studies difficult. It is also difficult to determine the extent to which Reynolds scaling effects may affect observations, but most agree that scaling effects are most pronounced in the near-wake where wake dynamics are a strong function of blade hydrodynamics.

Chamorro, Arndt, and Sotiropoulos [27] conducted an experimental study on a model wind turbine in order to determine what Reynolds number threshold was required for independence with respect to their turbine. Reynolds number, calculated using the

mean flow speed measured at hub height and the turbine diameter as the characteristic length, was increased until the streamwise velocity profiles and second order statistics (i.e. turbulence intensity and Reynolds stress components) collapsed onto a single profile for each respective parameter. Unfortunately, the results of this study are unique to this particular turbine geometry and the approach is useful only insofar as the achievable Reynolds number is not limited by equipment or facilities.

If the Reynolds number is used to describe the state of the flow over the blades, it makes the most sense to use the flow velocity the blade actually encounters, which is the relative velocity, U_{rel}. Similarly, the blade chord is the characteristic length that most readily describes the state of the flow over the blades. However, the relative velocity changes from blade root to tip and for tapered blades the chord length also changes. The question then becomes what relative velocity (i.e. blade radius) and chord length best describes the overall state of the flow over the turbine? It is advocated that the section of the blade that most contributes to power production should be the section at which the Reynolds number is defined. BEM theory suggests the region around 0.7R contributes most significantly to power production. A qualitative observation of the velocity deficit in the near wake of the turbine corroborates this being the radius at which the most power is extracted from the incoming flow (Figure 21). Viewed another way, sections closer to the hub have a relative velocity too low to contribute substantially to power production, and the contribution of sections near the tip are decreased by tip losses. Thus, it is advocated that the Reynolds number that best represents the achievement of dynamic similarity is calculated using the 0.7R chord length and relative velocity.

The NACA 63_3-618 airfoil section was selected for the present experiment, as opposed to the NACA 63_1-424 airfoil featured by RM1, because it has shown to be Reynolds number independent at $Re_c \approx 1 \times 10^6$ [28]. A study conducted by the authors [14] demonstrated that at $Re_c \approx 4.2 \times 10^5$ the NACA 63_3-618 airfoil was Reynolds number independent in lift and only slightly dependent in drag. Using the parameters specified previously, the Reynolds number for the present experiment was approximately 4×10^5, thus very nearly independent with respect to lift and slightly dependent with respect to drag. The impact of Reynolds number dependence in this case is likely a slightly lower prediction of power and thrust coefficient compared to the fully scale-independent turbine.

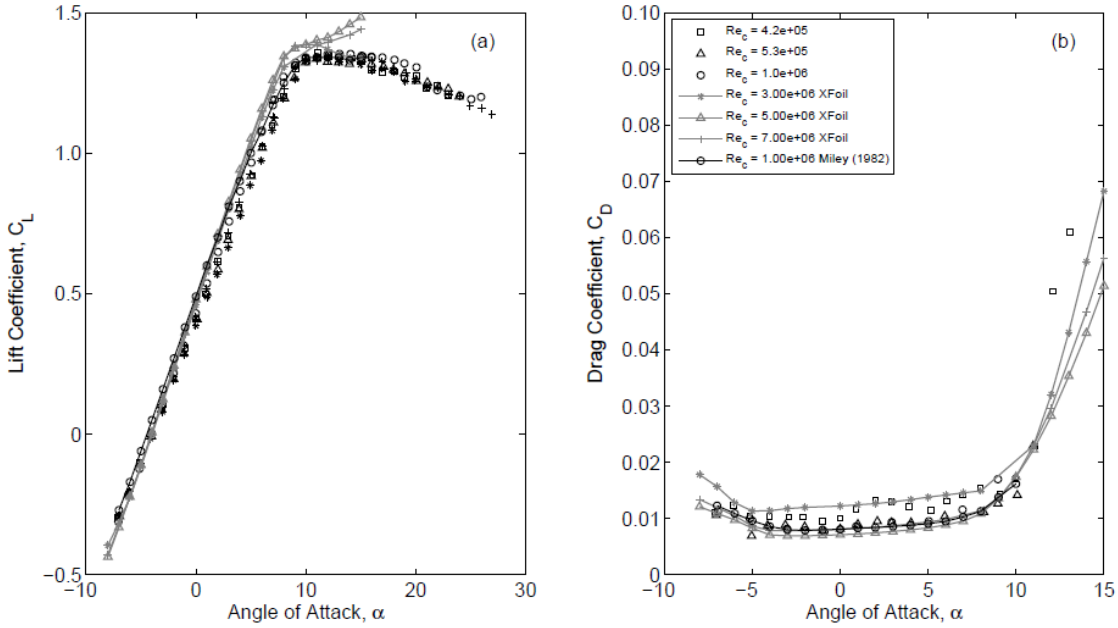

Figure 6: (a) Lift and (b) drag coefficient as a function of airfoil angle of attack and Reynolds number [14].

The turbine and dynamometer were attached to the towing carriage by one of two hydrodynamic, surface-piercing struts. Both struts had a characteristic (wet) length of 0.3 m and a maximum thickness of 0.06 m. The primary (short) strut measured 1.0 m in length and was used for turbine performance testing, in both steady and unsteady conditions, and

all wake survey experiments. The secondary (long) strut had an overall length of 1.8 m and was only used for turbine performance testing, in both steady and unsteady conditions.

2.3.3 Measurement of performance parameters

The equipment used to measure turbine performance parameters is shown in Figure 7. Thrust and torque were measured using a Cussons R46 dynamometer, mounted in line with the turbine shaft. Shaft rotation speed and blade position were measured using a BEI Sensors H35 incremental optical encoder. Additionally, an in-house designed shaft position indexing system featuring a Hall Effect sensor was used to confirm the optical encoder index signal and also provide a Transistor-Transistor Logic (TTL) signal to trigger PIV image capture. The tip speed ratio was adjusted using a pair of Placid Industries, Inc. H250 hysteresis brakes attached to the output shaft. The brakes also served to dissipate the roughly 500 W of power produced by the turbine. For experiments involving waves, the surface elevation was measured with two Senix ultrasonic optical wave height sensors. One sensor was placed at the same streamwise location as the rotor plane about two diameters from the turbine centerline on the starboard side. The second was placed about one rotor diameter forward of the turbine tip path near the wall of the towing tank. All instruments were synchronized in time. All signals (i.e. carriage speed, shaft speed, torque, and thrust) were sampled at a rate of 700 Hz. Each run, or traverse of the towing tank, provided 30-40 s of steady state data at a carriage speed of 1.68 m/s.

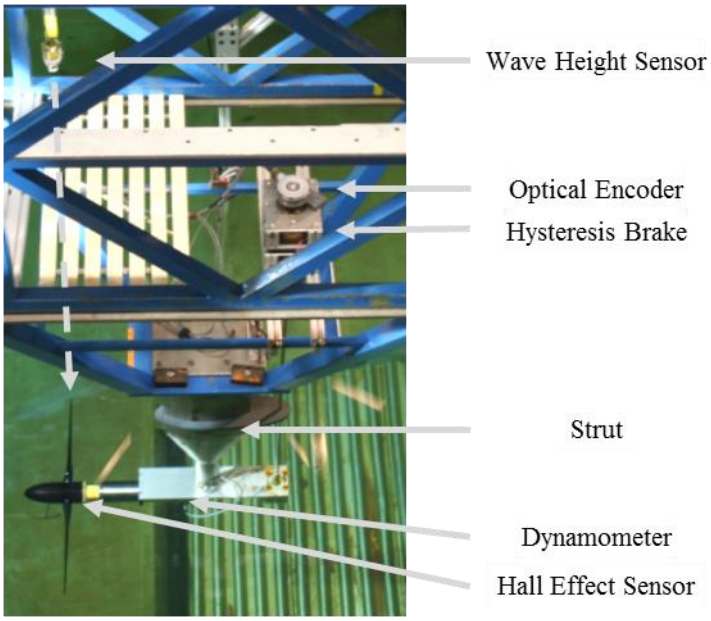

Figure 7: Test apparatus for turbine performance measurement including shaft speed, thrust, torque, and wave height. The vertical dashed line depicts the alignment of the wave height sensor with the turbine rotor plane.

Turbine wake expansion is blocked by the walls of the towing tank and the free surface causing flow to accelerate in the immediate vicinity of the turbine. This results in higher observed values for TSR, C_P, and C_T than would be observed in a free stream. Blockage correction factors for each of these performance parameters were calculated using the actuator disk model methodology detailed in Bahaj et al. [21]. For example, given an inflow speed of 1.68 m/s and a thrust coefficient of 0.84, the downstream flow speed is accelerated to 1.7 m/s and the correction factors for TSR, C_P, and C_T were 0.99, 0.98, and 0.99, respectively. Blockage effects were thus neglected.

Similarly, there is some critical distance between the turbine tip path and the free surface below which the free surface does not impact turbine performance. Maganga et al. [29] didn't note any difference in performance for a tip depth of 0.44D or greater. Bahaj, Molland, and Chaplin [21] did notice a decrease in performance when the turbine was

raised from a tip depth of 0.55D to 0.19D. Thus, free-surface effects are likely manifest at a relative depth less than 0.44D. For comparison, RM 1 is shown in Figure 1 to be placed at a relative depth of 0.5D below the mean low-low water (MLLW) line. Bahaj and colleagues theorized that the reduction in turbine power and thrust coefficient resulting from shallower operation was likely due to the blockage of wake expansion, thus a smaller velocity deficit and reduced power extracted from the flow by the turbine. In a follow-on study using an Acoustic Doppler Velocimeter (ADV) to measure the flow field around perforated disks[5] in a flume, Bahaj et al. [30] found that proximity to the flume bottom had a greater effect on wake development than the free surface.

To characterize free surface effects for the present experiment, turbine performance measurements were taken at seven relative depths from 0.1D to 0.5D in quiescent flow (i.e. flow without surface waves) at TSR values of 7. It was determined that at depths greater than 0.35D (0.28 m or approximately 11 in.) the free surface did not impact turbine performance. The turbine tip depth was set to at least 0.35D for this and all subsequent studies.

Related to considerations of turbine operations in close proximity to the free surface are considerations of cavitation. Cavitation occurs when the local pressure on the surface of the turbine blade falls to or below the vapor pressure of the surrounding water. Cavitation can degrade performance by changing local flow characteristics and can also cause damage to the turbine itself.

A number of articles describe prediction and observation of cavitation for a given blade geometry and operating condition including [21, 23]. Using the methodology

[5] Often used as a turbine surrogate.

described by Batten et al. [24] and modified in Buckland et al. [31] the critical cavitation coefficient was calculated:

$$\sigma_{crit} = \frac{p_\infty - p_v}{\frac{1}{2}\rho U_{rel}^2} \tag{4}$$

where p_∞ is the static pressure at a given depth, in absolute terms (i.e. $p_{atm} + \gamma z$), and p_v is the vapor pressure of water. The relative velocity was calculated as follows:

$$U_{rel} = \sqrt{(U_{tow}\,(1-a))^2 + (r\Omega(1+a'))^2} \tag{5}$$

The induction factors are calculated from BEM theory as previously discussed. The critical cavitation coefficient is compared to the local pressure coefficient:

$$\sigma = \frac{p_\infty - p_L}{\frac{1}{2}\rho U_{rel}^2} \tag{6}$$

where p_L is the local pressure at a given point on the surface of the turbine blade. If the local pressure coefficient is greater than or equal to the critical cavitation coefficient (i.e. if $\sigma \geq \sigma_{crit}$) cavitation will occur.

The critical cavitation coefficient was calculated for the expected worst-case conditions including minimum depth in the presence of waves and maximum turbine rotation speed at high TSR, also in the presence of waves. The in-house BEM model was used to calculate induction factors and XFoil was used to calculate the local pressure coefficient. The predicted local pressure coefficient was approximately 2/3 of the critical value, thus cavitation was not expected.

2.4 Results and discussion

Towing carriage speed, shaft speed, torque, and thrust were measured for TSR values of approximately 6 to 10. The corresponding C_P and C_T values were calculated are shown in Figure 8.

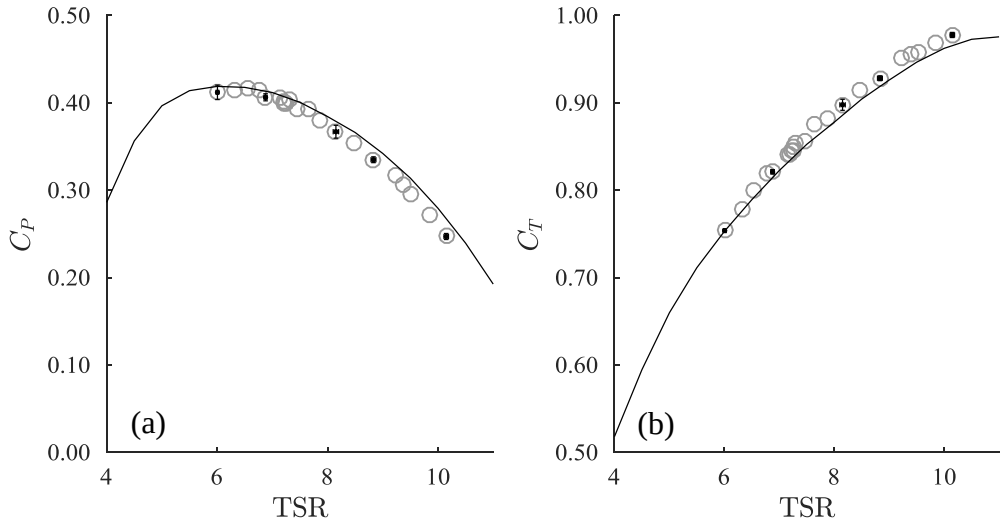

Figure 8: (a) Power coefficient and (b) thrust coefficient versus tip speed ratio, adapted from Walker et al. [14]. Open circles represent time averaged experimental results. The solid line represents blade element momentum (BEM) model predictions for a Reynolds number of 4×10^5. Error bars are included at integer values of TSR, quoted at 95% confidence.

Each marker represents the time average for a single carriage run. Towing carriage speed was set to 1.68 m/s throughout the experiment and the TSR was adjusted by increasing the voltage input to the hysteresis brakes. TSR values below 6 were unobtainable due to shaft binding at high brake torque.

At low TSR values, the angle of attack over much of the blade is high enough to be in the stall region, especially near the blade root. As TSR increases, the angle of attack decreases as does the local lift coefficient, but the relative velocity also increases resulting in increased power production up to peak performance, as shown in Figure 8a. A peak power coefficient of 0.43 was obtained at a TSR value of approximately 6.5, in close

agreement with previous studies (e.g. [21]). For TSR values above peak performance, the angle of attack is generally small, but as relative velocity continues to increase, drag also increases disproportionate to lift, degrading turbine performance. For a full-scale prototype modeled after RM1, a single turbine is predicted to produce approximately 550 kW in a mean flow of 2 m/s, in close agreement with predictions.

The thrust coefficient increases throughout the entire range of TSR values, as shown in Figure 8b. As TSR increases the relative velocity increases and the angle of attack decreases which is directly proportional to the lift coefficient. However, due to the exponential relationship between velocity and lift, the overall lift coefficient increases with increasing TSR. Also, with decreasing angle of attack, the component of the lift vector oriented parallel to the axis of rotation (i.e. thrust) also increases. At peak performance, the thrust coefficient is approximately 0.84, again in close agreement with previous studies.

An uncertainty analysis was performed using the Taylor Series Method in accordance with ISO/BIPM Guidance for Uncertainty of Measurement (GUM) [32] as described in Ratcliffe and Ratcliffe [33]. For each of the measured signals, the type A uncertainty[6] was calculated as follows. The signal, S was divided into n bins and the mean value, $\bar{S}_i$ calculated for each bin. The degrees of freedom (*dof*), equal to $n-1$, and the confidence level (in this case 95%) are used to calculate the Student's-t value. The standard type-A uncertainty for the measured value is:

$$u_A = \frac{t_{95\%,dof}}{\sqrt{n}} \sum_{i=1}^{n} \sqrt{(\bar{S}_i - \bar{S})^2} \tag{7}$$

[6] Known by convention as the *random* uncertainty, type A uncertainties are those that can be evaluated by statistical analysis.

where $\bar{S}$ is the time averaged signal. The number of bins, typically around 20, was determined using a sensitivity analysis. The type B uncertainty[7] was calculated including resolution, sensitivity, and analog-to-digital conversion elemental uncertainties. Zero offset uncertainty was addressed by recording 30 s of data prior to a run during which the turbine and towing carriage were still. This average voltage value was then subtracted from the measured signal prior to application of the calibration coefficient. Each elemental uncertainty is divided by the k-factor (in this case k = 2 for 95% confidence) to yield the standard uncertainty. All type B elemental uncertainties were combined by calculating the root of the sum of the squares (RSS). Type A and B uncertainties are also combined by calculating the RSS for each quantity. The absolute uncertainty for the measured quantities, U_M is calculated by multiplying the standard uncertainty by the k-factor (i.e. $U = uk$).

The expanded uncertainty for each calculated value, U_C (i.e. TSR, C_P, and C_T) was calculated by propagating the absolute uncertainty for each of the measured quantities as follows:

$$U_C = \left(\sum_{i=1}^{m} (U_{M,i} \frac{\partial U_C}{\partial U_{M,i}}) \right)^{\frac{1}{2}} \tag{8}$$

where m is the number of terms in the calculated value and $\partial U_C / \partial U_{M,i}$ is the sensitivity coefficient which describes how the calculated quantity changes with the measured

[7] Known by convention as the *systematic* or *bias* uncertainty, type B uncertainties are those that are evaluated by means other than statistical analysis.

quantity. The absolute and expanded uncertainties for a representative case are presented in Table 3.

Table 3: Absolute and expanded uncertainty values for a representative run, quoted at 95% confidence.

R (m)	ρ kg/m^3	U_{tow} m/s	Ω rad/s	Q N·m	T N	TSR -	C_P -	C_T -
0.3997± 2.5e-5	998.49± 0.02	1.6818± 0.001	29.806± 0.143	17.144± 0.108	625.62± 1.406	7.0830± 0.034	0.4287± 0.004	0.8827± 0.002
0.006%	0.002%	0.067%	0.481%	0.628%	0.225%	0.487%	0.944%	0.263%

All absolute uncertainty values were comparatively small, with the torque signal contributing most to the expanded uncertainty in TSR and C_P.

BEM predictions were made using an in-house code based on the methodology detailed in Manwell, McGowan, and Rogers [10] and were corrected for tip loss effects. Lift and drag data, required by the algorithm, was supplied from extensive wind tunnel testing of the NACA 63_3-618 airfoil as described in Walker et al. [14]. BEM theory, as discussed in the introduction, generally predicts the peak value of C_P and corresponding the corresponding value of C_T quite well but tends to over-predict C_P and under-predict C_T at higher TSR values. Agreement between experimental results and BEM model predictions are comparable to previous studies [24, 25].

2.5 Conclusions

A 1/25th scale axial-flow marine hydrokinetic turbine modeled after the U.S. Department of Energy's Reference Model 1 tidal current turbine was tested in the large towing tank facility at the U.S. Naval Academy. Previous tests indicate that the turbine is near Reynolds number independent in lift and only slightly dependent in drag. Baseline performance parameters such as C_P and C_T were calculated as a function of TSR and found

to be in good agreement with previous studies. A BEM model was developed and was also found to be in good agreement with experimental observations. The effect of operating depth on turbine performance was evaluated and a minimum operating depth was determined. The likelihood of cavitation was predicted using established methods and it was determined that cavitation would be unlikely for the anticipated range of depths and TSR values. An uncertainty analysis was also conducted for calculated quantities.

3 Turbine performance testing in unsteady conditions

3.1 Abstract

The installation of axial-flow marine hydrokinetic turbines has been proposed for a variety of locations, each with unique bathymetry, navigation requirements, environmental considerations, etc. Proposed installation methods include everything from fixed-position mounts such as monopiles to floating fixtures anchored to the seabed. Given the unique requirements of each installation site, the vertical placement of the turbine within the water column is a design parameter to be determined. One of the environmental factors that should be taken into consideration is the impact of surface gravity waves. Surface waves impose an unsteady velocity that can significantly impact turbine power quality and structural loading.

In support of the U.S. Department of Energy's Reference Model Project, a 1/25th scale model based on RM1 was created at the U.S. Naval Academy and tested in the large towing tank facility in order to assess the impact of surface gravity waves on turbine performance. The model was a two-bladed, 0.8 m diameter rotor featuring a NACA 63_3-618 airfoil cross-section that is shown to be near Reynolds number independent with respect to lift coefficient in the operating range of $Re_c \approx 4 \times 10^5$. Rotational speed, torque, and thrust were measured at a range of tip speed ratios (TSR) from approximately 6 to 11. Tests were performed at two rotor depths (1.3D and 2.25D) in the presence of two wave forms. The time average turbine performance characteristics were shown to be largely unchanged by depth or the presence of waves. However, tests with waves indicate large variations in thrust, rotational speed, and torque occurred with the passage of the wave. These results demonstrate the impact of surface gravity waves on power quality and

structural loading and suggest that turbines should be positioned vertically within the water column at a depth which maximizes power output while minimizing material fatigue.

3.2 Introduction

The power produced by a turbine is a function of the cube of the free stream velocity (Equation 1), thus turbines should be placed in the water column in the region with the highest average flow speed. Not accounting for any unique bathymetry, this is typically near the free surface, above the seafloor boundary layer if possible. However, the trade-off of placing a turbine in this region is that it is also the region in which the influence of surface waves is strongest.

In situ, waves are composed of a broad spectrum of heights, periods, and directions. However, for the purpose of isolating and characterizing their effect, only a single wave form was used at any given time in this study. Additionally, a limitation of towing tank experiments is that the waves can only travel head on (opposite the carriage direction) or following (in the same direction as the carriage). In the present study the wave group velocity was in the same direction as the mean current, opposite the carriage velocity.

Surface gravity waves are dispersive waves where the period, T and wavelength, λ are related, for a finite water depth, via the dispersion relation:

$$\lambda = \frac{g}{2\pi} T^2 \tanh \frac{2\pi}{\lambda} h \tag{9}$$

where g is the gravitational acceleration, and h is the mean water depth. The elevation of the free surface, η at a given point in space, x and time, t for a linear (also called Airy) wave is given by the following expression:

$$\eta = \frac{H}{2}\cos(kx - \sigma t) \tag{10}$$

where H is the significant wave height (twice the amplitude), k is the wave number equal to $2\pi/\lambda$, and σ is the wave angular frequency, equal to $2\pi/T$. The x-component or streamwise velocity, u is calculated:

$$u = \frac{H}{2}\sigma\frac{\cosh k(h+z)}{\sinh kh}\cos(kx - \sigma t) \tag{11}$$

where z is vertical distance from the free surface such that $z = -h$ at the seabed. Likewise, the vertical velocity, w is calculated:

$$w = \frac{H}{2}\sigma\frac{\sinh k(h+z)}{\sinh kh}\sin(kx - \sigma t) \tag{12}$$

Regular waves are often classified by their relative depth, h/λ. Shallow waves are defined as $h/\lambda < 0.05$, intermediate waves as $0.05 < h/\lambda < 0.5$, and deep waves as $h/\lambda > 0.5$ [34]. This classification is useful because for waves of equal height, the depth to which the effect of surface waves penetrate is inversely proportional to the relative depth, which is to say deeper waves (higher relative depth values) create less velocity shear as compared to shallower waves (lower relative depth values).

Another important parameter to consider is the wave energy per unit width:

$$E_L = \frac{1}{8}\rho g H^2 \lambda \tag{13}$$

where ρ is the density of the medium. These parameters, defined in [34] are used in the following discussion.

3.2.1 Literature review

There are few studies describing the interaction between axial-flow marine hydrokinetic turbines and waves. For various turbine geometries including scales, numbers of blades, and airfoil shapes, studies primarily focus on the impact of the two primary wave parameters: significant wave height and period on power and thrust measurements. In all cases the time average value of C_P and C_T was in close agreement with the steady case [35, 36, 37, 38, 39]. However, the instantaneous value for measured quantities – typically shaft speed, torque, and thrust, and thus their respective coefficients – was shown to vary considerably over the wave period [35, 38, 39, 40]. It is also noted in the literature that there is some impact of TSR on the range of signal response for each of the measured quantities likely related to local flow phenomena such as dynamic stall and reattachment [35, 37], though the nature of this relationship is not yet understood.

3.2.2 Present work

The purpose of this portion of the overall research effort was to characterize the performance of a large-scale model turbine in the presence of surface gravity waves. Of particular interest was the impact of turbine operating depth, which was predicted to change the wave velocity shear experienced by the turbine. Also of interest was the impact of changing wave parameters on the range of measured power and thrust. It is not yet clear which wave parameter, significant wave height, period, or a combination of parameters such as relative depth or steepness, has a more significant impact on turbine performance. It could also be that the magnitude of signal response is simply a function of the wave energy, with a more energetic wave eliciting a larger response.

3.3 Experimental details

3.3.1 Strut Length

As mentioned previously, two struts – one 1.0 m (L/D = 1.30) in length and one 1.8 m (L/D = 2.25) in length – were used for turbine performance testing in the presence of waves.

3.3.2 Wave scaling

The waves selected for this experiment were intended to represent oceanic swell typically found off the U.S. mid-Atlantic coast having a period of approximately 8 s, a wavelength of 90 m, and a significant wave height of 2 m [41]. The wavelengths were scaled to a model scale by matching the relative depth (h/λ) assuming an absolute depth at full-scale of 50 and 100 m for waves 1 and 2, respectively. Wave height was scaled using the steepness (H/λ) and was held constant for both waves in an effort to vary only one parameter (relative depth) at a time. The relative depth of wave 1 places it slightly above the limit of intermediate waves, while the relative depth of wave 2 is classified as a deep wave [34]. For each wave, the period was determined from the wavelength using the dispersion relation (Equation 9). The resulting scaled wave parameters are detailed in Table 4.

Table 4: Wave parameters for two model waves.

Wave	Relative Depth h/λ	Wavelength λ	Period T	Steepness H/λ	Height H	Energy E_L
1	0.6	8.25 m	2.3 s	0.022	0.18 m	327 J/m
2	1.2	3.99 m	1.6 s	0.022	0.09 m	40 J/m

For experiments involving wave 1, approximately 20 wave periods were observed for each traverse of the towing tank. For experiments involving wave 2, approximately 30 wave periods were observed.

Two sources of wave scattering were addressed in the experiment: waves reflected by the wave-absorbing "beach" and waves created by the surface piercing strut reflecting off the side-walls of the towing tank. Wave maker calibration experiments indicate the amplitude of beach reflected waves to be less than 5% of the height of the incident wave and were assumed to have negligible impact. This assumption is further supported by the consistent wave forms shown in Figure 9. The effect of the side-reflected waves was also neglected because if it is assumed that the waves created by the surface-piercing strut have a celerity equal to the carriage speed, the towing carriage would be 15 m further down the tank before the diffracted wave returned to the center of the tank.

To model the velocity shear induced by the waves on the turbine, linear (Airy) and non-linear (second-order Stokes) wave models were fit to the free surface elevation data as shown in Figure 9. There is close agreement between the models and the data and between the models themselves. The R^2_{adj} coefficients for both models are above 0.98. Thus, the simpler linear model was used to calculate the velocity shear, shown in Figure 10.

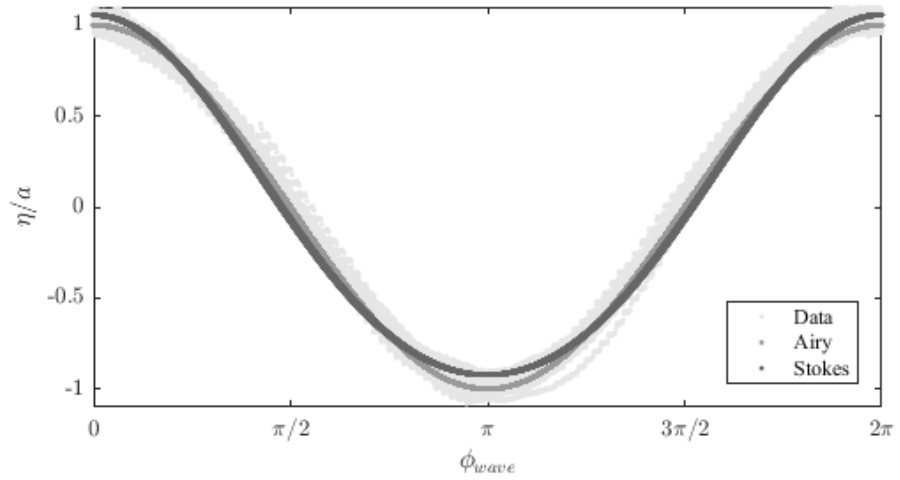

Figure 9: Wave data (light gray markers) for a representative run overlaid with a linear (Airy) wave (gray markers) and a non-linear (Stokes) wave (dark gray markers) for comparison.

Figure 10a depicts the minimum and maximum horizontal velocity profiles for wave 1 (h/λ = 0.6, shown in gray) and wave 2 (h/λ = 1.2, shown in black). For wave 1, the finite separation of the advancing and retreating wave velocity profiles at the bottom of the tank (z/h = -1) indicates that the influence of the surface waves spans the entire height of the water column, from the free surface to the bottom of the towing tank. This separation is not present in the corresponding vertical velocity profile, shown in Figure 10b. This asymmetry is indicative of the elliptical particle path of shallower waves (i.e. those with smaller relative depth). In contrast, there is no separation between the velocity profiles for wave 2 (h/λ = 1.2) at the bottom of the tank, indicating that the water in this region is undisturbed by surface waves. The comparative symmetry of the horizontal and vertical velocity profiles for wave 2 indicates the circular particle path characteristic of deep water waves.

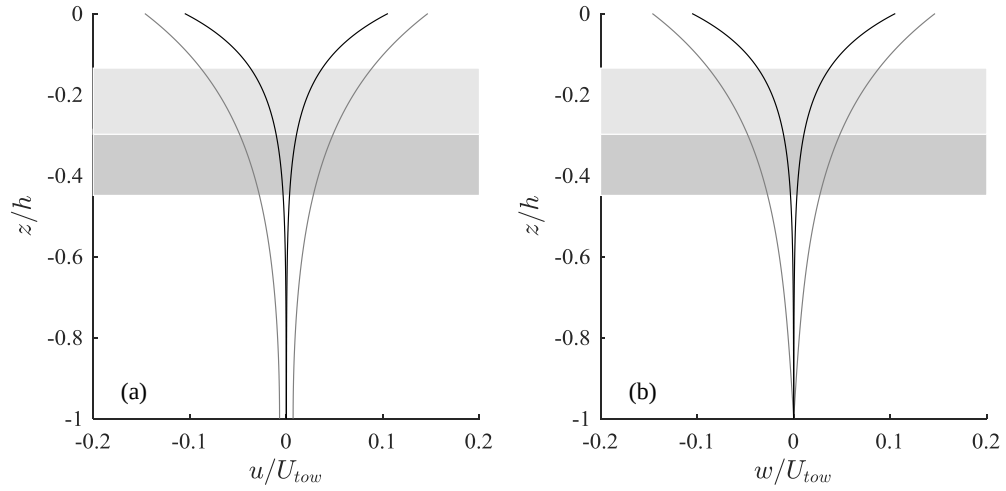

Figure 10: (a) The horizontal and (b) vertical velocity profiles for wave 1 (h/λ = 0.6, shown in gray) and 2 (h/λ = 1.2, shown in black). The light gray shaded region depicts the vertical extent of the turbine attached to the short strut and the dark gray shaded region depicts the vertical extent of the turbine attached to the long strut.

In all cases – short strut or long strut, wave 1 or wave 2 – the turbine was predicted to experience velocity shear induced by the waves. In the case of wave 1 attached to the short strut (L/D = 1.3), the maximum horizontal and vertical wave velocities experienced by the turbine were both on the order of 9% of the towing carriage speed. The associated shear was approximately 0.08 s^{-1}. For wave 2 attached to the short strut, the turbine saw a maximum horizontal and vertical wave velocity of approximately 4% of the towing carriage speed, and experienced a shear of 0.05 s^{-1}. For the long strut (L/D = 2.25), the magnitude and shear for wave 1 was reduced to 5% and 0.04 s^{-1}, respectively and 1% and 0.02 s^{-1} for wave 2, respectively.

For comparison to potential in situ conditions, Luznik et al. [41] conducted near-bottom in situ PIV measurements off the U.S. Atlantic coast in depths down to 30 m and determined the mean velocity shear ranges from 0.02 to 0.1 s^{-1} depending on a number of factors including seabed roughness, current velocity, and surface wave activity, etc. The

predictions discussed above are of the same order of magnitude giving confidence that test conditions are representative of potential field conditions in terms of wave velocity shear.

3.4 Results and discussion

Baseline performance characteristics for steady inflow (no waves) at the two different turbine immersion depths (L/D = 1.30 and 2.25) were plotted as a function of TSR and are shown in Figure 11. Each marker represents the time average value for a single carriage run. The white symbols represent data associated with the short strut and the gray symbols represent data associated with the long strut. Towing carriage speed was set to 1.68 m/s for each run and the TSR was adjusted by increasing the voltage input to the hysteresis brake. TSR values below approximately 5.5 in the no-wave case were unobtainable due to shaft binding at high brake torque. This situation was exacerbated

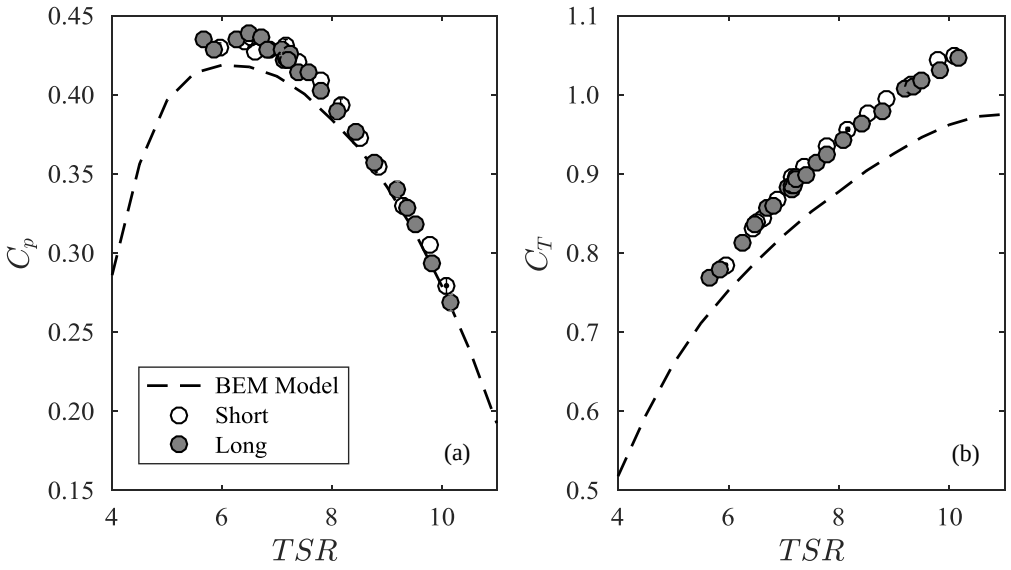

Figure 11: (a) Power coefficient and (b) thrust coefficient as a function of TSR in steady conditions (no waves) for strut lengths (L/D) of 1.3 (shown in white) and 2.25 (shown in gray). The dashed line represents BEM predictions corrected for tip-losses. Error bars depict representative uncertainty at 95% confidence.

during the wave experiments as the variable turbine torque dropped well below baseline values for a similar TSR.

There is no discernable difference between the performance observed at the two depths which is expected considering both are deeper than the critical tip depth, discussed in Chapter 2.

Turbine performance parameters C_P and C_T, each averaged in time over an entire run, are shown versus TSR in Figure 13 for all cases. Again, measurements associated the short strut are shown with white symbols. Measurements associated with the long strut are shown with gray symbols. Circles represent no-wave conditions. Squares represent experiments involving wave 1. Triangles represent experiments involving wave 2.

Wave relative depth appears to have little discernible effect on the average values of both C_P and C_T, which is consistent with results found in the literature [35, 36], so long as the turbine is not so close to the free surface as to inhibit wake expansion [30]. This is not a surprising result considering the improved performance associated with the advancing wave is likely equal to the degraded performance associated with the retreating wave, regardless of wave parameters. The time average values do appear to be sensitive to turbine depth, however, with a slight increase in power and thrust measurements observed for experiments associated with the short strut as compared to those taken from the long strut, but the difference is within the experimental uncertainty and thus cannot be discerned.

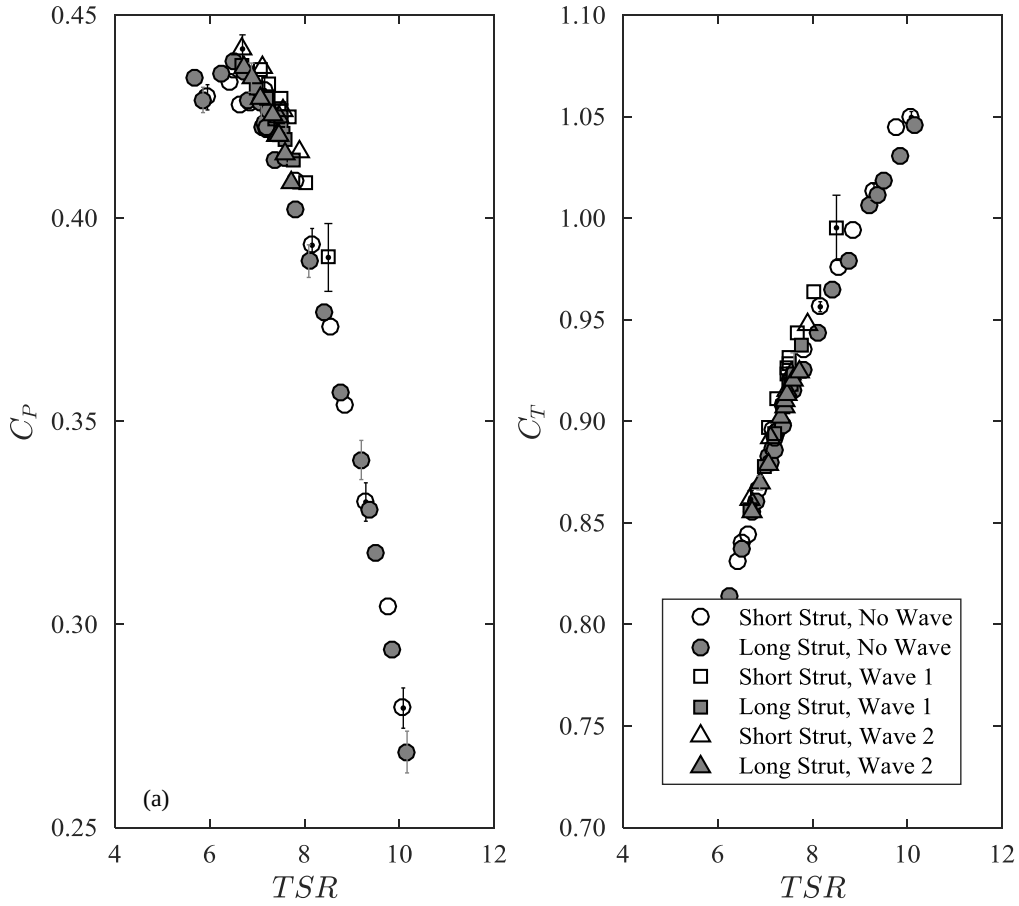

Figure 12: (a) Power and (b) thrust coefficient as a function of TSR for both strut lengths (L/D = 1.3, 2.25) in the presence of both wave forms (h/λ = 0.6, 1.2). Error bars depict representative uncertainty, quoted at 95% confidence.

The resulting overall average values for power and thrust coefficient were shown to change little with turbine depth and less still with the relative depth of the wave acting upon it. Both of these results are consistent with previous experiments [35, 36]. Power quality and fatigue loading, however, depend on the range of power and thrust experienced by the turbine. Significant variations in power coefficient result in poor electrical power quality, and significant variations in thrust require materials with a higher fatigue limit to withstand the cyclic loading. Therefore, it is prudent to consider the range of instantaneous values in addition to the overall average values.

Data from four runs representing the four combinations of strut length and wave classification were selected, each near peak power production (i.e. TSR = 7). The surface elevation was used as a basis for conditionally sampling each of the measured properties of turbine speed, torque, and thrust according to the wave phase, ϕ_w from 0 at the wave crest to π at the wave trough. This translation from the time domain to the phase domain was conducted using the Hilbert transform, defined for periodic functions. An in-depth description of this transform is given in Bendat and Piersol [42], and its application to conditional sampling of unsteady phenomena is provided in Huang et al. [43, 44] and Luznik, et al. [38]. The results of this analysis are shown for the case of L/D = 1.3 and h/λ = 0.6 in Figure 13. The overall average value, corresponding to a single symbol in Figure 12, is shown in each plot as a horizontal dashed line. The phase-average value was calculated by binning the values of the measured quantities at each degree of wave phase and calculating the bin average.

TSR, shown in Figure 13b appears to lag the wave elevation by a phase angle of $\pi/2$, which may indicate the influence of the vertical component of velocity or may be caused by the inertia of the turbine and output shaft. In this case, the TSR can be thought of as the non-dimensional shaft speed as it is multiplied by two constants: the blade radius, R and the towing carriage speed, U_{tow}. Thus, the power coefficient which is proportional to the shaft speed, as well as the torque also shows this same influence. The thrust coefficient profile, however, more closely agrees with the surface elevation, perhaps indicating a strong dependence on the horizontal component of the wave velocity.

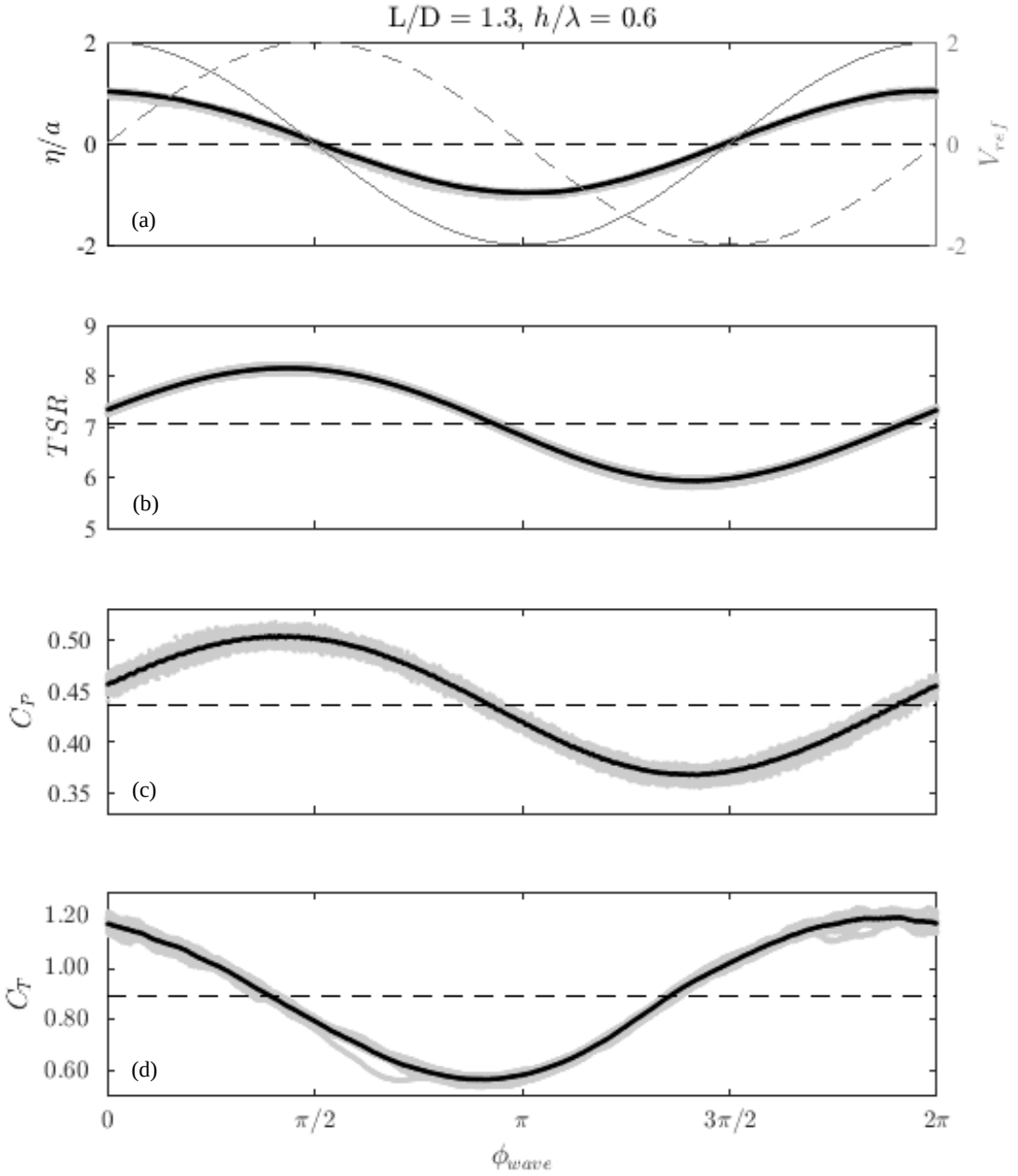

Figure 13: Wave phase averaged performance parameters in the presence of wave 1 (h/λ = 0.6) attached to the short strut (L/D = 1.3). The light gray dots indicate conditionally sampled data as a function of instantaneous wave phase calculated from surface elevation (a), the dashed horizontal line represents the average value over the entire run (corresponding to the symbols in previous figures), and the solid line indicates the phase average value for that parameter. A reference horizontal (solid gray) and vertical (dashed gray) wave component velocity is plotted in (a) for reference.

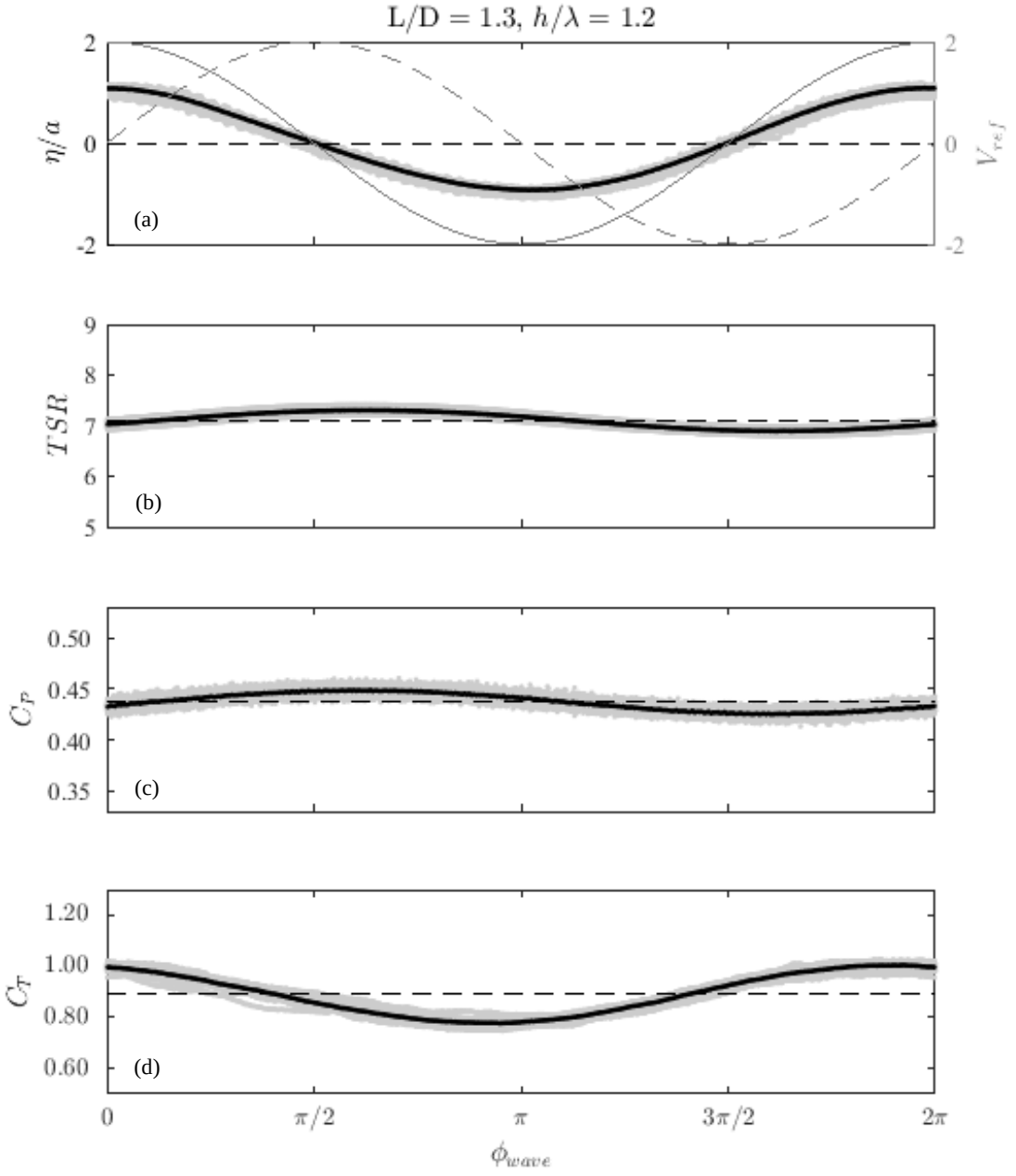

Figure 14: Wave phase averaged performance parameters in the presence of wave 2 (h/λ = 1.2) attached to the short strut (L/D = 1.3). The light gray dots indicate conditionally sampled data as a function of instantaneous wave phase calculated from surface elevation (a), the dashed horizontal line represents the average value over the entire run (corresponding to the symbols in previous figures), and the solid line indicates the phase average value for that parameter. A reference horizontal (solid gray) and vertical (dashed gray) wave component velocity is plotted in (a) for reference.

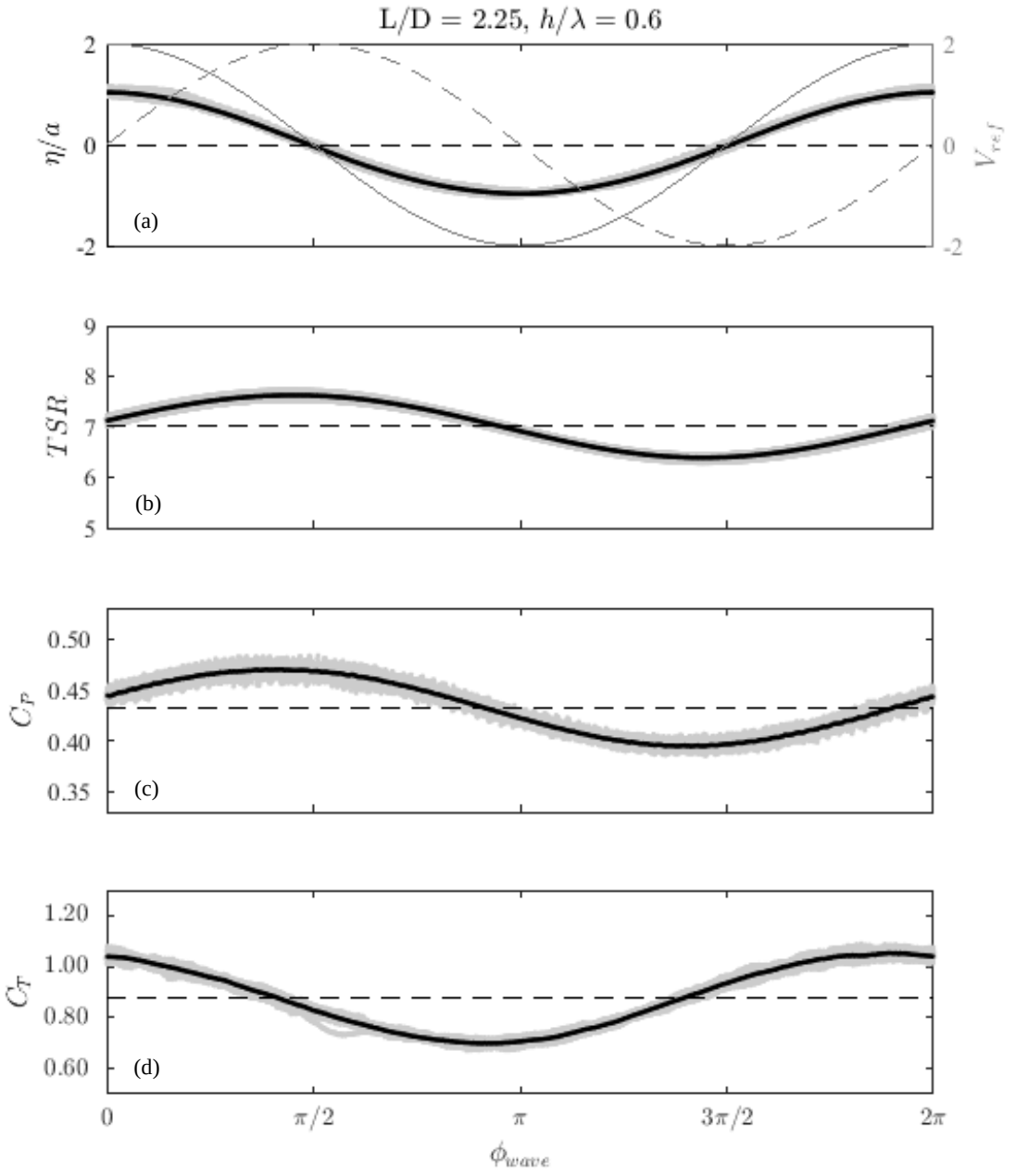

Figure 15: Wave phase averaged performance parameters in the presence of wave 1 (h/λ = 0.6) attached to the long strut (L/D = 2.25). The light gray dots indicate conditionally sampled data as a function of instantaneous wave phase calculated from surface elevation (a), the dashed horizontal line represents the average value over the entire run (corresponding to the symbols in previous figures), and the solid line indicates the phase average value for that parameter. A reference horizontal (solid gray) and vertical (dashed gray) wave component velocity is plotted in (a) for reference.

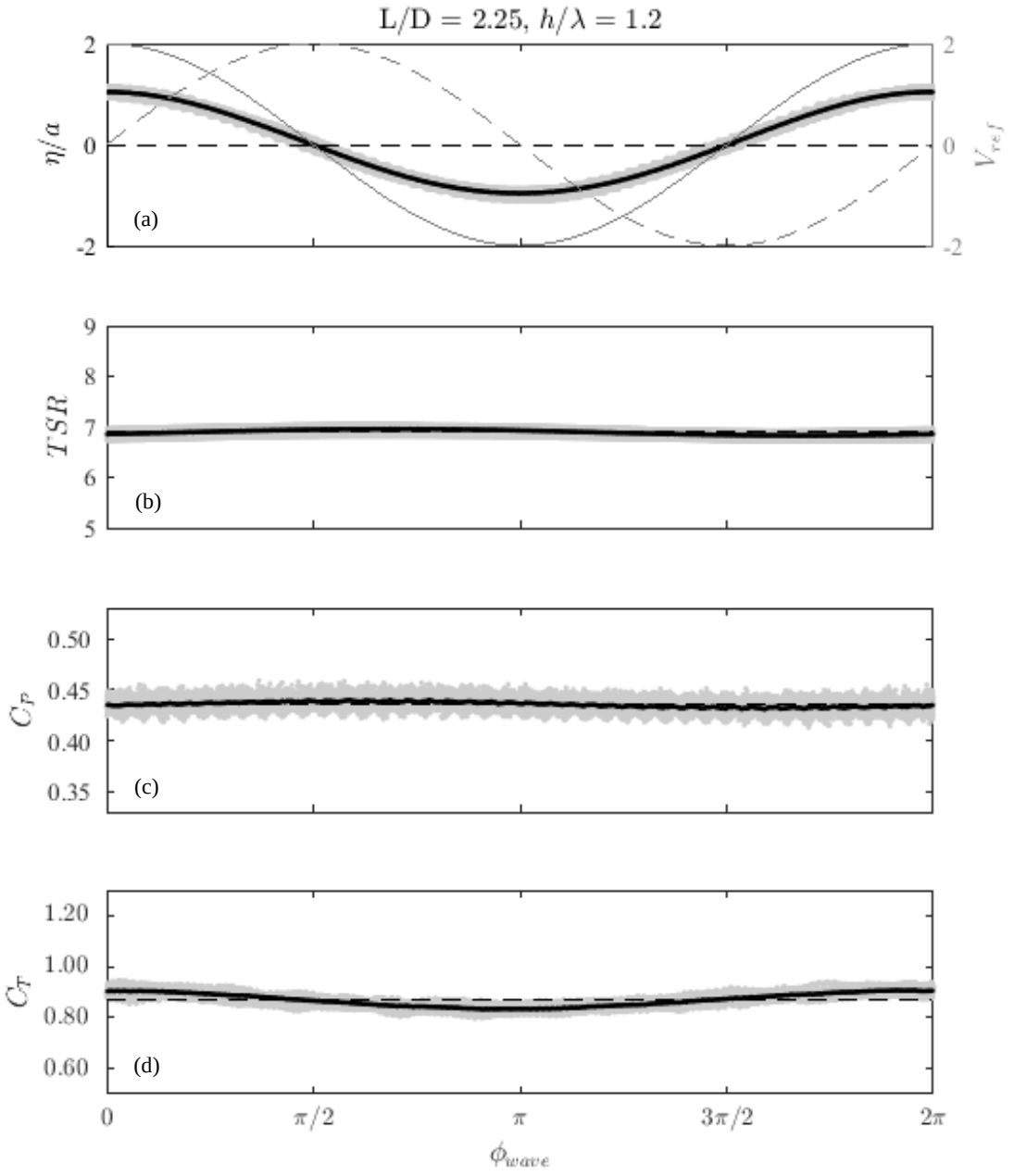

Figure 16: Wave phase averaged performance parameters in the presence of wave 2 (h/λ = 1.2) attached to the long strut (L/D = 2.25). The light gray dots indicate conditionally sampled data as a function of instantaneous wave phase calculated from surface elevation (a), the dashed horizontal line represents the average value over the entire run (corresponding to the symbols in previous figures), and the solid line indicates the phase average value for that parameter. A reference horizontal (solid gray) and vertical (dashed gray) wave component velocity is plotted in (a) for reference.

Comparing the results for the short strut in the presence of wave 1 (Figure 13) and wave 2 (Figure 14), there is a clear difference in TSR, C_P and C_T as a function of wave phase with the range for all values appreciably lower in the second case as compared to the first. This is in contrast to the close agreement of the time average values indicated in Figure 12. There is also a slight phase shift between the two cases with TSR and C_P lagging (i.e. shifted to the right) slightly in the case of wave 2 as compared to wave 1. It is hypothesized that the phase shift is related to the relative magnitude of the horizontal velocity component compared to the vertical velocity component. For wave 1, the wave with the lower relative depth, the magnitude of the maximum horizontal velocity is larger than that of the vertical velocity, whereas for wave 2, having a deeper relative depth, the magnitude of the two components is approximately equal. As the disparity between the two components increases (i.e. with an increasingly shallow wave), perhaps the influence of the vertical velocity is lessened and the maximum TSR and C_P shift toward the maximum surface elevation at $\phi_w = 0$.

Comparing short strut performance (Figure 13) to long strut performance (Figure 15) in the presence of wave 1, signal variation is clearly decreased with depth and thus velocity shear. However, unlike the previous comparison, there does not appear to be an appreciable phase shift, further supporting the hypothesis that the phase shift is a function of the ratio of horizontal to vertical velocity component rather than the magnitude of either.

Comparing short strut performance (Figure 14) to long strut performance (Figure 16) in the presence of wave 2, the variation of performance values with wave phase is

decreased to a comparatively small range indicating that the wave has little influence on turbine performance. Although it is barely perceptible as depicted in Figure 16[8], the TSR and C_P signals show the same phase as in the shallow case further supporting the hypothesis that relative depth and phase shift are correlated.

Unfortunately, the mechanism for the phase shift of any of the measured signals cannot be determined a priori as consideration must also include factors such as flow dynamics in the immediate vicinity of the turbine blades, turbine mass moment of inertia, output shaft friction, etc. The development of a relationship between turbine geometry, operating parameters, wave parameters, and performance response in terms of dimensional analysis represents an potential opportunity for future study.

[8] Axes for all four related figures were made equal to enable direct quantitative comparison.

Table 5 summarizes the results for each of the four cases presented in Figure 13 through Figure 16 for comparison. The overall average TSR value is similar for each case, as are the average C_P and C_T values. Ranges for each of the calculated quantites were calculated from the minimum and maximum phase-averaged quantities, not the minimum or maximum values for the data set. This range was then normalized by the overall average value (corresponding to the horizontal dashed line in each of the figures) to indicate variation from the mean.

Table 5: Phase-averaged performance parameters for representative runs at TSR ≈ 7.

Strut Length L/D	Wave Form h/λ	$\overline{TSR}$	TSR Range	$\overline{C_P}$	C_P Range	$\overline{C_T}$	C_T Range
1.30	0.6	7.06	8.15-5.93 (31%)	0.44	0.51-0.36 (33%)	0.89	1.20-0.57 (71%)
1.30	1.2	7.10	7.31-6.89 (6%)	0.44	0.45-0.42 (7%)	0.89	1.00-0.78 (26%)
2.25	0.6	7.01	7.62-6.39 (18%)	0.43	0.48-0.39 (20%)	0.88	1.05-0.70 (40%)
2.25	1.2	7.06	7.13-7.00 (2%)	0.43	0.45-0.41 (8%)	0.88	0.92-0.84 (9%)

For wave 1, the range of C_P is roughly half of what it is for C_T. For wave 2, C_P is approximately equivalent or less than C_T. This phenomenon – the range of C_P values being less than the range of C_T values for a given experiment – has also been noted in the literature [35, 36, 39]. This is perhaps due to the sensitivity of the normal force (i.e. lift) to the tangential force (i.e. torque) to the change in local angle of attack associated with the unsteady velocity of the wave.

It should be noted that the energy per unit length of wave 1 is over eight times that of wave 2, so the disparity of response was not unexpected. However, it should also be noted, that the maximum unsteady velocity in any case – wave 1 or 2, short strut or long – was at most 9% of the free-stream velocity. In the case of wave 1 paired with the short strut, this relatively small velocity variation had an outsized impact on C_P and C_T with variations of 33% and 71%, respectively. For comparison, in a mean current of 2 m/s, a full-scale version of wave 2 would produce a maximum horizontal velocity of 0.14 m/s or 7% of the mean current speed at a hub depth of 25 m.

3.5 Conclusions

A 1/25th scale model axial-flow hydrokinetic turbine based on RM1 was tested in the large towing tank facility at the U.S. Naval Academy to assess the impact of waves on performance. Tests were performed at two rotor depths (1.3D and 2.25D) in the presence of two distinct wave forms (h/λ = 0.6 and 1.2), both with equal steepness.

In the presence of waves, the time average value for each performance parameter, taken over the entire run, is equivalent to the same value for the no-wave case. This time-average value is not affected by the relative depth of the wave or the operating depth of the turbine for the waves and depths tested in the present experiment. However, for the purposes of evaluating the impact of waves on power quality and structural loading, the time-average value is a poor and potentially misleading indicator of operating conditions. Even in the presence of relatively small waves, the range of calculated performance values including TSR, C_P, and C_T was comparatively large. TSR and C_P showed a strong dependence on the vertical velocity, whereas C_T appeared to be influence to a greater extent by the horizontal velocity. There appears to be a relationship between wave relative depth, namely the difference in the magnitude of the horizontal velocity compared to the vertical velocity, and the relative phase of the performance value. A better understanding of this relationship could be beneficial to the design of active control systems. As noted previously in the literature, variations in C_T were generally larger than those for C_P. This may be due to the sensitivity of the normal and tangential forces to changes in the local angle of attack associated with the unsteady velocity induced by the waves.

Due to limitations imposed by the experimental apparatus, other combinations of waves could not be tested. Future work could include a series of tests in the presence of

waves with equal relative depth but different steepness, and waves of equal energy per unit width and differing relative depth. The results from such a study could parse the effect of each parameter on turbine performance.

4 Wake survey under steady conditions

4.1 Introduction

The constricting bathymetry that may make a site attractive for the installation of a marine hydrokinetic turbine array also necessarily constraints the available footprint. Therefore optimizing turbine placement in a multi-turbine array to maximize power production and minimize structural loading is critical to the cost-competitiveness of the installation. Optimal spacing is largely dependent on the characteristics of the wake produced by each turbine, specifically on the downstream distance at which the coherent turbulent structures in the wake dissipate sufficiently. The factors thought to affect wake breakdown and subsequent re-energization occur in the near wake, within the first several diameters downstream of the turbine. It is therefore imperative to better understand these mechanisms.

In this section the characteristics of the wake are explored using a variety of techniques from canonical wake studies to more recent advancements in helicopter rotor aerodynamics. It also serves as a useful benchmark against which to compare the wake characteristics of a turbine in the presence of waves.

4.2 Abstract

Flow field results are presented for the near-wake of an axial-flow hydrokinetic turbine in quiescent flow conditions. The turbine is a 1/25 scale, 0.8 m diameter, two bladed turbine based on the U.S. Department of Energy Reference Model 1 tidal current turbine. All measurements were obtained in a large tow tank facility at the United States Naval Academy with the turbine towed at a constant carriage speed, producing a nominal tip speed ratio of 7. The turbine is nearly scale independent for these conditions. The wake

velocity field data was obtained using an in-house designed and manufactured, towed, planar particle image velocimetry (PIV) system at locations within two diameters of the rotor plane. PIV ensembles were obtained for phase locked conditions with the reference blade at the horizontal position.

The present study focuses on characterizing the velocity and the mean flow structure in the near wake with emphasis on the downstream evolution of coherent tip vortices shed by the rotor blades. Wake expansion, indicated by the position of the vortex centers, follows a 1/3 power law expansion. Coherent vortices are identified up to approximately 1.6D. Beyond this location, vortex meandering precludes identification of individual vortices. The streamwise spacing between the vortex centers is constant within one diameter downstream of the rotor, with interaction of neighboring vortices modifying the spacing further downstream. Within the measurement field, the phase averaged turbulence is small and mostly due to the aperiodicity or meandering of the vortex cores.

4.2.1 Literature review

A number of experimental studies have focused on wake velocity measurements in the vicinity of a single axial flow turbine. Results show that the influence of the turbine appears to extend as far as two rotor diameters (2D) upstream of the rotor plane [45]. Flow swirling in this region has also been observed, prior to passing through the rotor plane [46]. Downstream of the turbine, observations confirm Froude's theory which predicts the velocity in the near wake ($x/D < 2$) to be approximately one-third that of the free stream, recovering in the far wake ($x/D > 2$) [47]. It was also observed that the turbulence in the near wake is highly anisotropic, suggesting isotropic turbulence models are not appropriate for modeling the flow in this region [48].

Wake expansion caused by the downstream velocity deficit is well documented in the wind turbine literature and is also observed in marine turbine experiments [45, 49, 50]. Expansion of the shear layer is shown to be proportional to the 1/3 power of the streamwise distance [45]. Mycek et al. [51] state that the wake is not axis-symmetric, an observation also made by Tedds, Owen and Poole [48], however, it's not clear if the asymmetry is a result of blockage caused by either the free surface above or the channel floor below. Chamorro et al. observed approximate azimuthal uniformity in the near wake of the turbine and wake rotation in the direction opposite the turbine [46, 47, 49, 52, 53].

Several studies included particle image velocimetry (PIV) measurements taken at a constant turbine blade phase (e.g. [46]) showing coherent blade tip vortices within 2D downstream of the turbine. Within 1D, vortices were observed to be strong and spatially stable [45], becoming less concentrated as they convected downstream [46], and decreasing in concentration and positional stability at downstream distances of 1.5D to 2D [45, 47, 52]. The distance between the adjacent helical vortex filaments in this region was observed to be fairly constant by Okulov [47] although the opposite was observed by Chamorro et al. [49]. The difference in the two observations may depend on whether or not meandering, also called *aperiodicity*, was accounted for. Using the average spatial diameter of the Q-isosurfaces, Chamorro et al. [49] observed that vortex core diameters were of the same order of magnitude as the blade chord.

Several studies have investigated the instability modes of the helical tip vortex in an effort to predict the streamwise point at which the near-wake structure begins to break down and subsequently re-energize. Widnall [54] found three instability modes: a short-wave mode, a long-wave mode, and one mutual inductance mode relating to the streamwise

distance between adjacent filaments. Predictions were confirmed for marine propellers by Felli et al. [55] who showed that the mutual inductance mode has the greatest impact on wake stability. Their observations were confirmed for wind turbines by Sherry et al. [53] who also observed that first evidence of mutual inductance occurs at the same non-dimensional downstream distance $0.6h$ where h is the helical pitch, a function of the turbine tip speed ratio and number of blades. Sherry et al. also stated that the breakdown of helical structure in the near wake was influenced by interaction between the root and tip vortices, though this was shown not to occur within 1D by Chamorro et al. [49].

In a pair of related studies, Lignarolo et al. [52, 56] posed and addressed a number of important questions regarding kinetic energy transport in the wake region. Of particular interest to the present discussion is the question of what role the tip vortices play in enhancing or inhibiting kinetic energy transport from the mean flow to the wake. They concluded that there is effectively no mixing in the near-wake, the helical tip vortex structure shielding it from re-energization within the first two turbine blade diameters downstream.

Wake characteristics have also been shown to be affected by inflow turbulence such as the wake signature of upstream turbines. Inflow turbulence was shown to increase blade loading fluctuations, shorten the downstream wake recovery distance [50], and heavily influence the shape, length, and strength of the wake [51]. The instantaneous power generated by the turbine was shown to be strongly affected by turbulent inflow features below a specified critical frequency. It was also shown that this frequency varied linearly with the angular frequency of the turbine at scales corresponding to the largest structures in the wake [49].

4.2.2 Present work

The goal of the present study is to collect high spatial resolution velocity data in the near wake of a large-scale model axial-flow hydrokinetic turbine under steady conditions. In addition to providing experimental data for computational model validation, this data can be used to corroborate, and in some cases clarify, the observations discussed in the preceding background. This knowledge can then be applied during the planning process reducing the uncertainty associated with implementation and potentially helping to reduce the cost of electricity for marine renewable energy.

4.3 Experimental details

The velocity field in the near wake of the model turbine was measured using 2-D particle image velocimetry, a technique used in previous studies (e.g. [53, 56]). The PIV camera and light arm were contained in an in-house designed and manufactured system mounted directly to the towing carriage and submerged. The system, shown in Figure 17, features two submersible housings, one forward-looking and one side-looking, both streamlined to minimize flow disturbance in the measurement region. The laser or camera can be mounted interchangeably in either submersible, providing subsurface visualization capability in vertical planes parallel to both the long and short axis of the towing tank.

For all imaging experiments, the submersibles remained fixed to the towing carriage and the turbine was translated to change the field of view. The side-looking

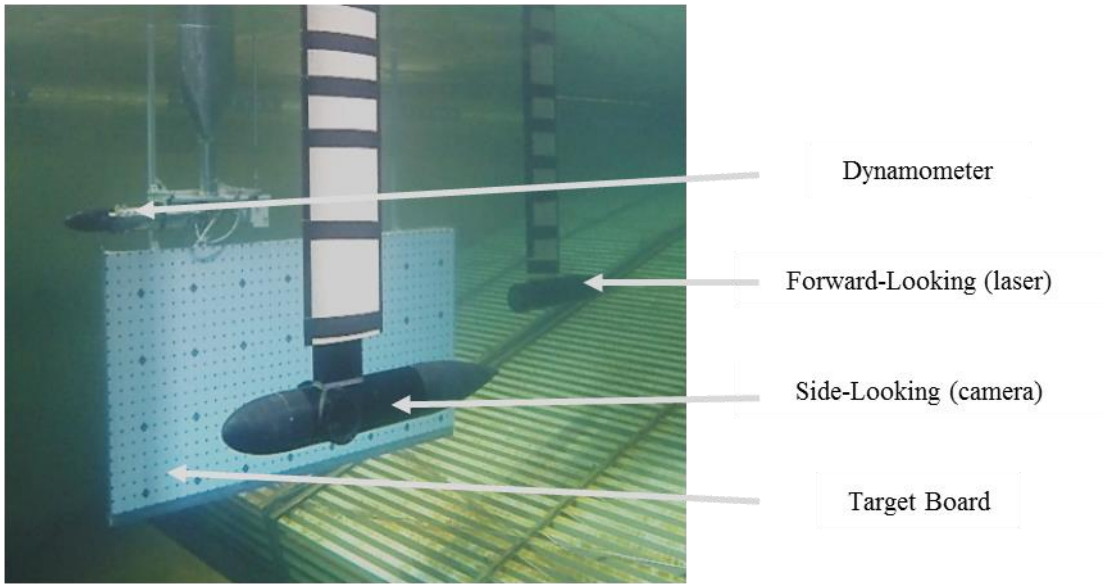

Figure 17: An underwater view of the field of investigation including the dynamometer and turbine (turned so that the blades are horizontal), the target board (included in the image for reference but removed during data acquisition), the side-looking submersible which contained the camera and remote-focus electronics, and the forward-looking submersible which contained the laser light arm and laser sheet optics. During data acquisition, flow enters from the left. The entire submersible system was designed and manufactured in-house.

submersible was mounted 1.7D from the field of view and the forward-looking submersible was mounted at least 2.6D from the field of view with the turbine in the aft-most position.

The PIV system featured a Quantel Evergreen, dual cavity Nd:YAG 200 mJ 532 nm laser capable of a repetition rate of 15 Hz. A 5 mm thick light sheet was formed using a 1000 mm spherical lens in combination with a 15 mm cylindrical lens. The camera was a TSI PowerView Plus 4 MP CCD camera with a resolution of 2048 x 2048 px providing a nominal resolution of 1.9 mm for a nominal 0.3 m by 0.3 m field of view. A 50 mm lens was used with remote focus and aperture adjustment. The camera had a maximum frame rate of 7.25 PIV image pairs per second (in Straddling Mode) and was positioned approximately 1.4 m from the light sheet to preclude interference of the submersible camera housing with the field of view. Image pair capture was triggered by the Hall Effect sensor mounted to the turbine hub so as to phase lock the image pairs with the blades

positioned horizontally. The time between laser pulses was set to 1000 μs, thus the blades rotated approximately 1.7° between images.

PIV images were captured and processed using TSI Insight 4G software. Camera exposure was set to 420 μs and the aperture and autofocus were not changed once set initially to ensure a consistent field of investigation. At each position, 50 calibration images were taken and then averaged prior to calibration and de-warping yielding an average pixel size of approximately 157 μm. Images were processed using a recursive Nyquist grid engine (50% overlap), and an FFT based correlation engine where the sub-pixel displacement was estimated using a Gaussian peak engine. Vector validation was conducted using the local median filter and bad vector replacement was accomplished by valid secondary peaks from the local correlation maps. Any remaining holes were filled using local interpolation and the resulting vector fields were then low-pass filtered using a narrow Gaussian filter to remove high-frequency noise (higher than the spatial resolution).

The resulting particle displacements ranged from a minimum of approximately 2 px to a maximum of over 18 px, but the average displacement was approximately 8 px. Final interrogation spot size was set to 24 × 24 px providing a resolution of 12 px or 1.9 mm with less than 1% of vectors interpolated. Particle image diameter was calculated to be approximately 2 px.

The seed particles used in this experiment were Potters Industries Sphericell® 110p8 hollow glass microspheres. The mean particle size was 12 μm and the density ranged from 1.05-1.15 × 10^3 kg/m^3. The seed particles were distributed using a "rake," approximately the same overall size as the turbine diameter. The towing speed and rake tine diameter were selected to maximize mixing. Perforated tubing was attached to the

rake tines through which the seed particles were pumped. The rake was towed the length of the tank each day prior to the start of data collection and the process was repeated as needed as signal quality degraded. Seed particle concentration was approximately 0.5 kg per 200 L container of water and the volumetric flow rate for the seed/water mixture was approximately 0.5 L/s.

As noted in Mycek et al. [51] inflow turbulence intensity has a significant impact on the characteristics of the near-wake region of the turbine. Acoustic Doppler Velocimetry (ADV) measurements were therefore taken using a Nortek Vectrino acoustic velocimeter placed approximately 1D upstream of the turbine at a depth approximately equal to 0.7R in order to quantify the inflow turbulence. Several runs were made at decreasing time intervals between runs. Even at the shortest possible time between runs (about 6 min), the ambient turbulence intensity in the towing tank had dropped to less than 1%. Thus the influence of inflow turbulence in the following results was assumed to be minimal.

For this experiment, the streamwise direction, parallel with the long axis of the towing tank, was defined as the x-direction with the positive direction oriented downstream (opposite the direction of towing carriage travel). The vertical direction was defined as the z-direction with positive directed upward. The corresponding velocity vectors are denoted u and w, respectively. The origin for position reference was defined as the center of the turbine hub at the same streamwise position as the turbine blades (Figure 18).

PIV measurements were performed along the x-z plane, parallel to and beneath the output shaft of the turbine as shown in Figure 18. Fields of view extended from approximately 0.11 m (0.14D) upstream of the turbine tip path to 1.57 m (1.97D)

downstream and extending downward from beneath the turbine output shaft to a distance of 0.68 m (0.85D). Each individual field of view measured approximately 0.3 m by 0.3 m with 0.05 m overlap between adjacent fields (Figure 18). Measurements were made in a region of the wake that did not include the strut or support equipment.

For each field of view position approximately 1,000 steady-state (i.e. constant carriage speed) realizations were collected over the course of five runs with each run yielding approximately 200 realizations. Image capture was initiated using a Hall Effect sensor on the turbine hub such that each image pair was captured when the two blades were oriented horizontally (i.e. parallel to the free surface). Thus the resulting flow fields are phase locked at a single blade phase, ϕ_b.

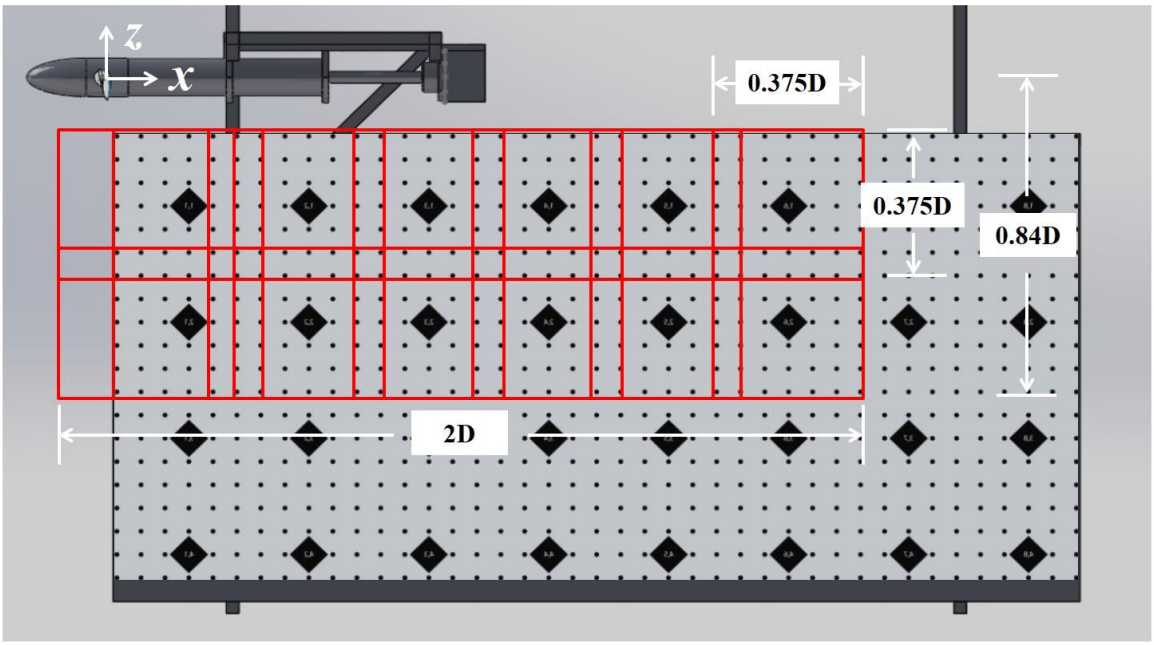

Figure 18: A schematic of the field of investigation. The red squares encompass each of the fields of view (14 total), each centered on a fiducial marker (solid diamond) and measuring approximately 30 cm by 30 cm. Flow entered from the left.

The classical Reynold decomposition of instantaneous velocity, u_i into mean and mean, $\bar{u}_i$ and fluctuating, $u_i{}'$ components [57]:

$$u_i(t) = \bar{u}_\iota + u_i{}'(t) \tag{14}$$

was modified by Reynolds and Hussain [58] to include the contribution of a reference oscillator, illuminating the contribution of the associated periodic signal to the topology of the flow. The triple-decomposition of the velocity signal, was used by Lingnarolo et al. [52] to describe the behavior of axial flow turbines as:

$$u_i(t) = \bar{u}_\iota + \tilde{u}_\iota(t + nT) + u_i{}'(t) \tag{15}$$

where the subscript i indicates the orthogonal velocity component, $\bar{u}_\iota$ is the time-average of the instantaneous signal, $\tilde{u}_\iota$ is the periodic signal associated with the reference oscillator (in this case the turbine), and u_i' is the random signal associated with turbulence. The term T is the period of the signal and n is the number of periods.

As mentioned in the previous section, the observations made in the present study were phase-locked with regard to turbine blade position, thus the phase averaging operation results in the sum of the time averaged signal and the periodic signal at a particular phase, defined as follows:

$$\begin{aligned} < u_i(x, z, \phi_b) > &= \frac{1}{N}\sum_{k=1}^{N} u_i(x, z, t_k, \phi_b) \\ &= \bar{u}_\iota(x, z) + \tilde{u}_\iota(x, z, \phi_b) \end{aligned} \tag{16}$$

where <> denotes the phase average, $N$is the number of realizations, and t_k is the time at which those realizations were captured. Likewise, the turbulence intensity, I_i at the given blade phase is calculated using the following expression:

$$< I_i(x,z,\phi_b) > = \frac{1}{N}\sum_{.}^{N}\sqrt{(u_i(x,z,t_k,\phi_b) - < u_i(x,z,\phi_b) >)^2} \tag{17}$$

The phase-averaged turbulence kinetic energy is calculated as follows:

$$\frac{1}{2}\frac{1}{N}\sum_{k=1}^{N}(u(x,z,t_k,\phi_b) - < u(x,z,\phi_b) >)^2 + (w(x,z,t_k,\phi_b) - w < x,z,\phi_b >)^2 \tag{18}$$

The Reynolds shear stress at the given blade phase was also calculated as shown:

$$\frac{1}{N}\sum_{k=1}^{N} -(u(x,z,t_k,\phi_b) - < u(x,t,\phi_b >)(w(x,z,t_k,\phi_b) - < w(x,t,\phi_b >) \tag{19}$$

In order to verify that approximately 1,000 realizations were sufficient to provide a statistically-independent phase average for all statistics, a cumulative average including 200, 400, 600, images, etc. was calculated and plotted for a single field of view (Figure 19). The selected field of view, located furthest downstream ($1.6 < x/D < 2.0$), was chosen because it included the shear layer and was in the region where the vortex meandering was most pronounced, thus representing the likely worst-case-scenario in terms of repeatability of velocity measurements. The first-order statistics were normalized

by the towing carriage speed and the second-order statistics are normalized by the towing carriage speed squared.

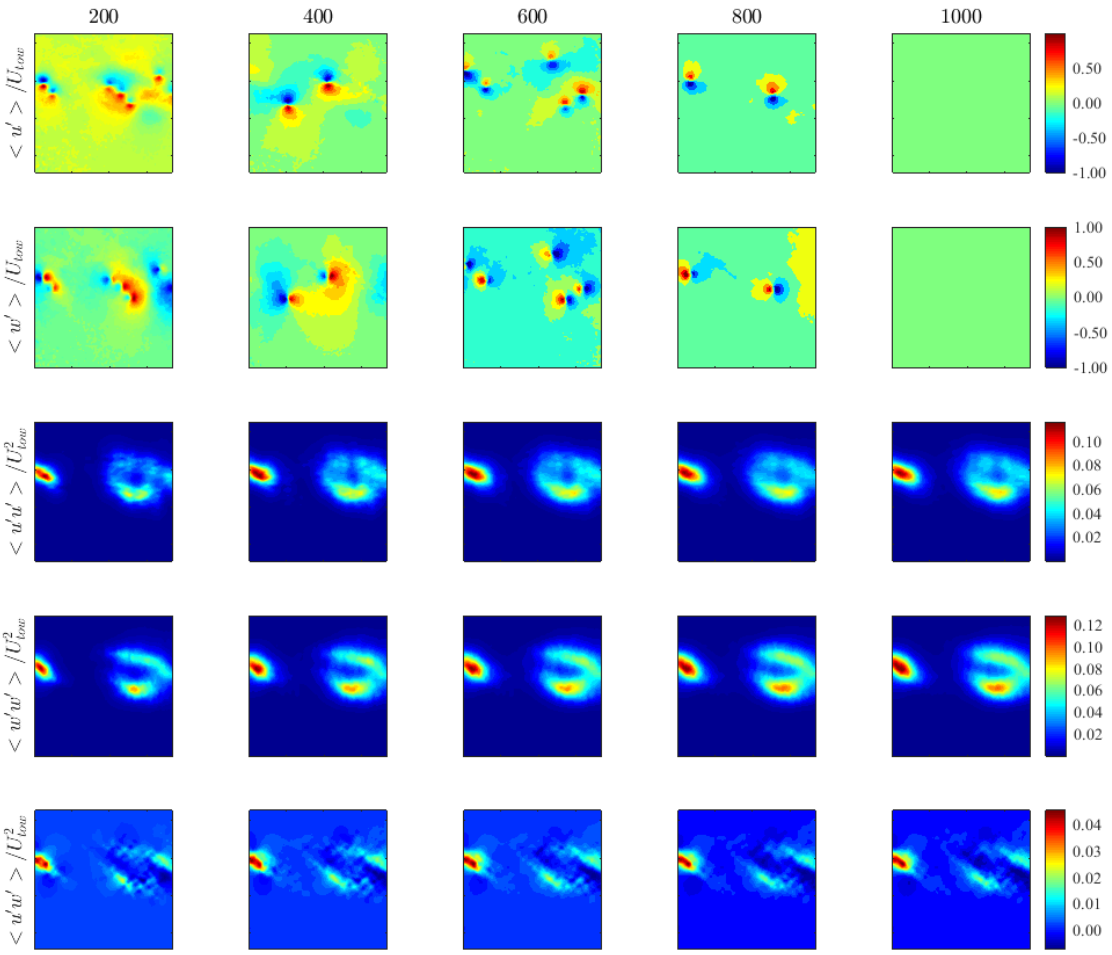

Figure 19: Cumulative average fluctuating velocity for u' (first row), w' (second row), $u'u'$ (third row), $w'w'$ (fourth row), and $u'w'$ (fifth row) for the number of realizations indicated in the column header. First-order statistics are normalized by the towing carriage speed, U_{tow} and Reynolds stress terms normalized by U_{tow}^2. Field of view located 1.6 < x/D < 2.0 and -0.45 < z/D < -0.85 from the turbine origin.

The fluctuating streamwise and vertical velocity components, u' and w' respectively, shown in the first two rows of Figure 19, average to 0 by 1,000 realizations indicating a statistically-independent phase average (i.e. $\overline{u_i'} \equiv 0$). Since the fluctuations were smaller for all other fields of view, these were assumed to have converged as well. The Reynolds stress terms, $u'u'$, $w'w'$, and $u'w'$, shown in the last three rows of Figure 19

converge with fewer realizations as indicated by the similarity between adjacent columns in each respective row.

Although unconditioned observations were also made (i.e. observations made at 7.25 Hz, independent of blade phase), the inherent challenge of towing tank testing precluded observations of sufficient number to also achieve a statistically-independent temporal average. Thus the time averaged signal (i.e. $\overline{u_i}$) could not be separated from the periodic signal (i.e. $\widetilde{u_i}(t + nT)$) for this analysis.

An uncertainty analysis was conducted using the image matching algorithm developed by Sciacchitano, Wieneke, and Scarano [59]. The algorithm is an *a posteriori* approach which analyzes the displacement field and original images using a discrete window offset technique to calculate the matched particle image disparity. A statistical analysis of this disparity returns the estimate for the velocity vector measurement uncertainty. The algorithm was applied to images from the same field of view shown in Figure 19. The maximum error was less than 2% for both velocity components, quoted at 60% confidence. It should be noted that the peak-locking errors and truncation errors in time are not detected with the image matching approach. However, as stated previously, the particle image diameter was greater than 2 px, thus peak-locking was not anticipated.

4.4 Results and discussion

A transform was created to map the center of each field of view, indicated by the center of the fiducial marker (see Figure 18), to the flow field origin. All x and z coordinates for each field of view were then transformed and plotted simultaneously. For adjacent fields of view, the x and z coordinates were not identical in the overlap region. When plotted, this artifact is manifested as a discontinuity in the overlapping region.

The tip vortices shed by the turbine blades are one of the most prominent features of the wake. They serve as useful markers for observing the evolution of the shear layer. More fundamentally, however, the interaction between adjacent helical vortex filaments is thought to be the primary mechanism for initiating momentum transport into and re-energization of the wake [52, 53, 55, 60]. Characterization is therefore critical to informing this discussion.

The λ_{ci} criterion developed by Zhou et al. [61] was used to estimate the vortex center position. However, using this method, the centroid could only be found within the measurement resolution of the interrogation window, approximately 1.9 mm. Moreover, as stated by Bhagwat and Ramasamy [62], measurement in the region of the core of a vortex is inherently difficult due to a seed particle void created by the strong swirling motion and variations in local velocity due to turbulence. Thus, using the methodology they developed for helicopter rotor research a vortex model was fit to the experimental observations in order to more accurately identify the vortex properties. Three vortex models – the Lamb-Oseen model generally used for laminar vortices, the Scully Vortex model generally representative of turbulent vortices, and the model developed by Vatistas et al. generally describing vortices in the transition region, all described by Leishman [63]

– were applied to each vortex in each realization using a non-linear least-squares fit algorithm as described in Ramasamy, Paetzel, and Bhagwat [64]. The fit was applied to a subregion of 21 by 21 elements (approximately 40 mm by 40 mm) centered on the location of maximum λ_{ci}. The core radii were then averaged for each vortex in each realization. The resulting average vortex core diameter was approximately 0.7 times the tip chord length of 24 mm (18 mm or 9 elements) in agreement with [49]. The model selected, of the three that were fit to a particular vortex, was based on which of the models produced the smallest residual norm in consideration for the changing nature of the vortices with streamwise distance. Each of the three models have been shown previously to predict the same centroid position [64]. This was also observed in the present study. Model results were compared to experimental results and are presented in Figure 22.

4.4.1 Mean flow

Figure 20a shows the phase-averaged streamwise velocity, $< u(x, z, \phi_b) >$ normalized by the carriage speed, U_{tow} for the entire field of investigation extending from 0.14D upstream of the turbine tip path to 1.97D downstream and to a depth beneath the output shaft of 0.85D. The velocity decreases just upstream of the turbine to approximately 75% of the towing carriage speed, the result of the slight rise in the static pressure of the free stream flow approaching the turbine. The tip vortices are rotating counter-clockwise (i.e. in the negative y-direction). Wake expansion, indicated by the position of the vortex centers, is modeled reasonably well by a 1/3 power law expansion (i.e. $z = ax^{1/3} + b$) with an R^2_{adj} correlation value of 0.95. This agrees well with theory and observations from horizontal axis wind turbine studies as well as the marine current turbine literature (e.g. [45]). Inside the wake, the velocity deficit is largest coincident with 0.3-0.4D radial

location from the output shaft (approximately 0.7R). The streamwise velocity reaches a minimum value, for this field of investigation, of approximately 1/3 the free stream flow velocity at approximately 2D downstream as predicted by Froude and previously observed (e.g. [47, 48]). As mentioned in the introduction, the maximum velocity deficit occurs downstream of the turbine because the static pressure, at its lowest immediately downstream of the turbine, recovers by extracting energy from the wake at the expense of velocity. Not accounting for losses or energy transferred to the wake from the mean flow, the streamwise location of the maximum velocity deficit marks the location where the static pressure has returned to that of the pressure far upstream.

Vortex meandering or *aperiodicity* as it will be referred to is defined as the random variations in the spatial location of the vortex centers. This is shown to increase with increasing wake age or the angular travel, in degrees, of the blade that created the helical vortex filament. Aperiodicity is thought to be the first manifestation of helical instability [53]. By approximately 1.6D, the aperiodicity is so pronounced as to make it impossible to identify individual vortices in a phase-locked regime, thus they are not labeled. However, the separation between the two point clouds downstream of $x/D = 1.8$ indicates that a level of coherency is maintained. A detailed discussion of vortex characteristics is included in the next section.

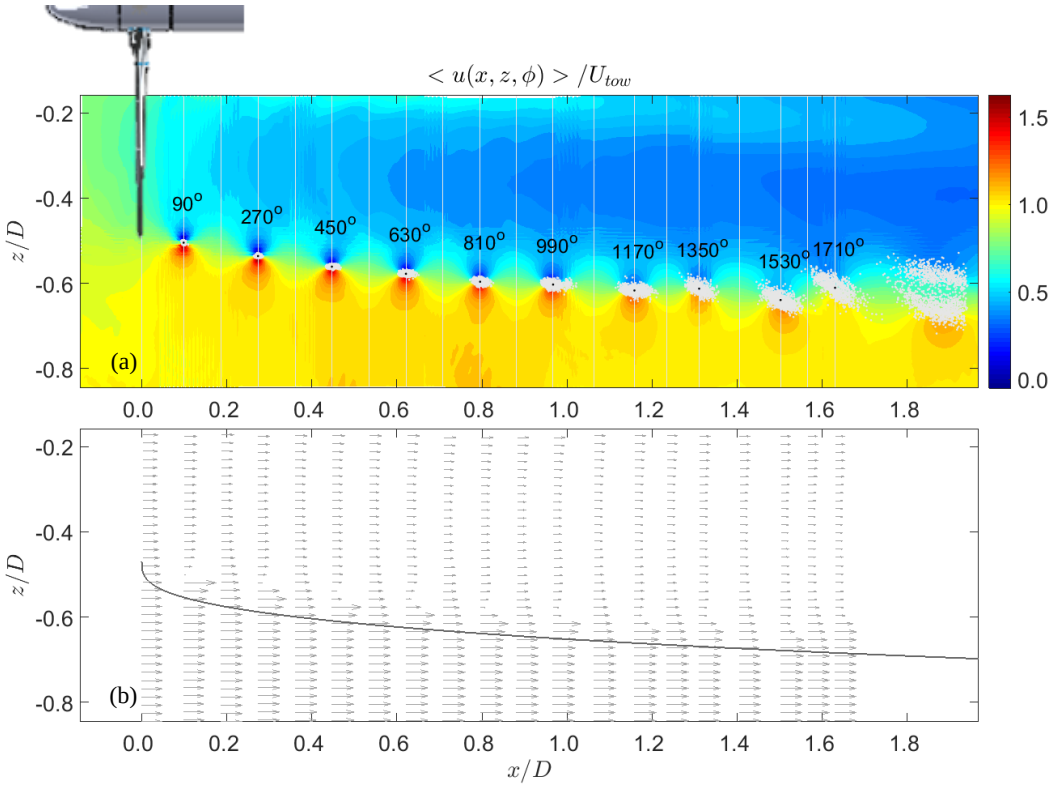

Figure 20: (a) Phase averaged velocity in the streamwise direction for the entire field of investigation. The annotations above each vortex indicate the wake age in degrees of turbine rotation. Light gray dots indicate vortex center positions for approximately 14,000 realizations. The black dots indicate the mean centroid position. The vertical lines indicate the position of the velocity profile shown in (b). The free stream velocity is from left to right and the turbine is shown to scale in the upper left-hand corner. Figure (b) shows the streamwise vertical velocity profiles for vertical cuts located at the mean centroid positions and positions between adjacent vortices. The solid line is a 1/3 power-law fit to the 0.99U_{tow} contour representing the wake boundary.

The vertical lines on Figure 20a correspond to the phase-averaged streamwise velocity profiles shown in Figure 20b. These vertical "cuts" pass through the turbine tip path, each mean vortex center position, and at the midpoint between adjacent vortices. The number of velocity vectors shown has been significantly reduced for clarity. The dark gray line indicates the wake width, δ, defined as $< u(x,z,\phi_b) > /U_{tow} \approx 0.99$.

For further confirmation of mean flow measurements, the drag on the turbine, approximately equal to the thrust, was calculated in terms of the deficit of momentum flux across in the wake at a distance of approximately 1.4D downstream (profile shown in

Figure 20b) where wake expansion had effectively ceased. The wake was also assumed to be axisymmetric. Since the field of investigation was displaced from the output shaft by approximately 0.16D (i.e. no data were recorded in this region) the velocity profile was estimated to be constant at the observed velocity nearest the output shaft. This is likely a low estimate since the streamwise flow in this region is likely to be slower. The calculated value of the wake drag was found to agree within approximately 5% of the independently-measured thrust coefficient value of 0.84, giving confidence in the observed results.

Figure 21a shows the phase-averaged vertical velocity, $< w(x, z, \phi_b) >$ also normalized by the carriage speed, U_{tow}. Just upstream of the turbine, there is a small negative vertical velocity component in the negative z-direction (i.e. radially outward), the result of wake expansion beginning upstream of the turbine. Wake expansion, as described by the vertical velocity, persists until approximately 1D after which there is very little vertical velocity outside of the vortices as indicated by the flattening of the wake boundary. This is consistent with what was shown by Chamorro et al [45]. The counter-clockwise rotation of the vortices is also clearly shown. The signature of several blade root vortices also appear in the upper left-hand corner of Figure 21a.

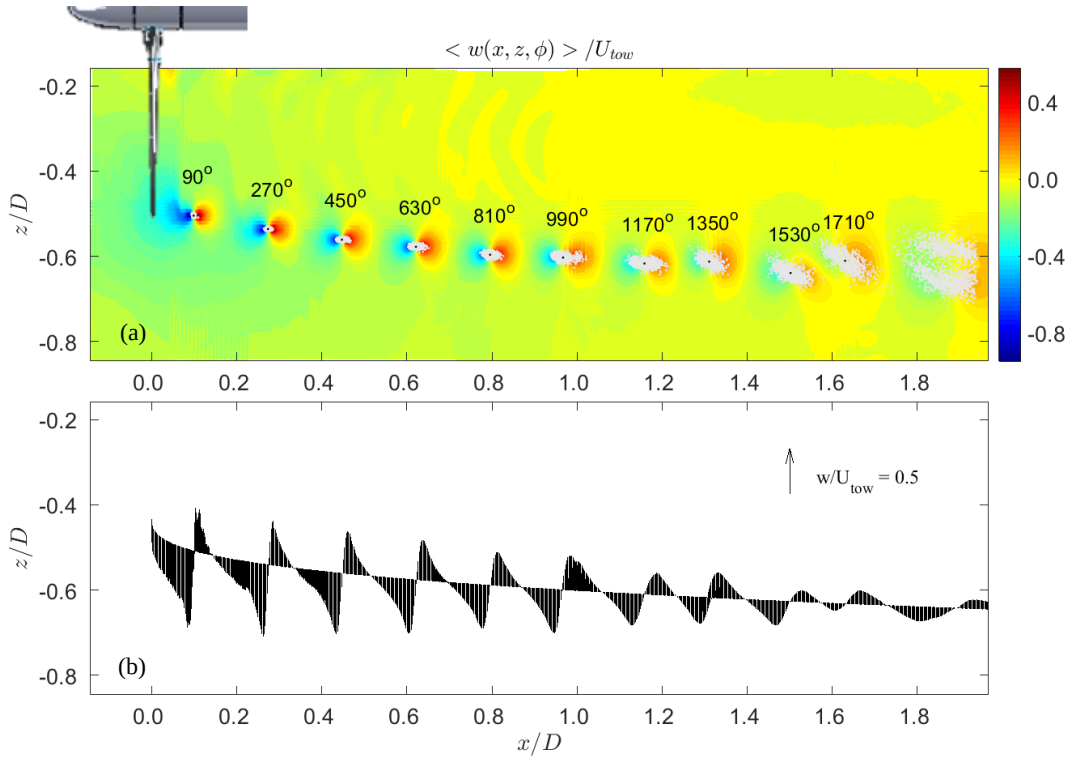

Figure 21: (a) Phase-averaged velocity for the entire field of investigation in the vertical direction. The annotations above each vortex indicate the wake age in degrees of turbine rotation. The light gray dots markers indicate vortex center positions for approximately 14,000 realizations. The black dots indicate the mean centroid position. The free stream velocity is from left to right, and the turbine is shown to scale in the upper left-hand corner. Figure (b) shows the vertical velocity profile plotted along the wake boundary, shown in Figure (a). The black arrows indicate the magnitude of the vertical velocity at that position, according to the scale indicated in the upper right-hand corner of the figure

In Figure 21b the phase-averaged vertical velocity is shown along the wake boundary, giving a sense of the magnitude of the flow across the wake boundary. Keeping in mind that velocities shown above are phase averaged over nearly a thousand realizations and that the wake boundary location is estimated, the figure approximates the swirl velocity profile for a horizontal "cut" through each of the tip vortices. It appears that the swirl velocity is decreasing with downstream distance. It also appears that the vortex core radius (i.e. half the distance between adjacent peaks) is increasing with streamwise distance, however, this is primarily a result of increasing aperiodicity, rather than core radius dilation, as discussed in a later section. Both Figure 21a and Figure 21b indicate that aside from the negative vertical velocity associated with wake expansion within the first

diameter, there is very little vertical velocity across the wake boundary, potentially indicating little exchange between the mean flow and the wake in terms of bulk fluid motion.

4.4.2 Vortex characterization

As shown previously, the turbine tip vortices feature prominently in any visualization of the phase-averaged wake and interaction between adjacent vortex helices is thought to be the primary mechanism for initiating breakdown of the coherent wake structure and subsequent wake re-energization [52, 53, 55, 60]. In Figure 22a, the vortex center positions for each realization are again indicated by the light gray dots and the average center position is marked with a black dot. The mean aperiodicity, $\overline{r_A}$ or variability of vortex center position from the mean position, is defined as:

$$\overline{r_A} = \frac{1}{N}\sum_{k=1}^{N}\sqrt{\left(x_{c,k} - \overline{x_c}\right)^2 + \left(z_{c,k} - \overline{z_c}\right)^2} \qquad (20)$$

The aperiodicity was calculated for each vortex over all associated realizations. The results are shown on the left y-axis of Figure 22b. At a wake age of 90° the vortex center positions are tightly grouped and thus the aperiodicity is low (i.e. the vortex center positions are highly periodic). As wake age increases aperiodicity also increases, indicated qualitatively by the expanding scatter of the gray dots in Figure 22a and quantitatively by the trend shown on the left y-axis of Figure 22b. On the right y-axis of Figure 22b it is shown that at wake ages less than approximately 990° vortex center spacing was fairly constant at 0.18D. However, for wake ages greater than 990° mean streamwise spacing increases and decreases alternately. This likely indicates the start of mutual induction. The interaction becomes more pronounced as the 1350° vortex is shifted upward in the positive

z-direction. The upward movement of the vortex is likely due to interaction between the upturning flow on the downstream side of the 1170° vortex and the down-turning flow on the upstream side of the 1350° vortex. Moreover, as the 1350° vortex is pushed into the slower-moving wake, it is slowed in the streamwise direction and its presence forces the 1170° vortex down into the faster-moving flow, furthering the counter-clockwise rotation of the now-grouped helices. This phenomenon is also shown in similar studies [52, 53]. The interaction is even more pronounced for the 1530° and 1710° vortices, which are clearly entangled and rotating around a common saddle point in a motion classically referred to as *leapfrogging*. The scatter associated with aperiodicity is also increasingly inclined relative to the horizontal, a manifestation of the underlying shear layer. In the case of the vortices detected downstream of approximately 1.7D, the aperiodicity was so great that individual vortices could not clearly be identified as being of a particular wake age. However, a close inspection shows that there is a slim, horizontally-oriented region of low vortex center density, suggesting that the 1890° vortex is being subducted beneath the 2070° vortex such that the two adjacent helices are now oriented vertically having gone through 90° of rotation together.

The vortex core radius, r_c was calculated for each vortex in each realization using two *cuts* – one horizontal (0^o) and one vertical (90^o) – through the element nearest the vortex center indicated by the vortex model. Each cut provided a velocity profile from which the vortex core radius and peak swirl velocity were calculated as discussed in Ramasamy et al., [65]. The resultant core radius values were averaged for each vortex and are shown as closed circles plotted on the left y-axis of Figure 22c. The vortex core radii, calculated using the vortex model fit methodology described in a previous section, were

also averaged for each vortex and also plotted on the left y-axis of Figure 22c as open circles for comparison. The two are shown to be in close agreement (maximum difference of 6%) giving confidence in the model results. The radii are non-dimensionalized by the turbine blade tip chord length, c and indicate that vortex core diameter is of the same order of magnitude, as previously observed [45, 53]. Vortex core radius is fairly constant at approximately 0.35c, in reasonable agreement with previous studies [53] until a downstream distance of $x/D \approx 1$, after which the core radius begins to decrease.

On the right y-axis of Figure 22c the mean peak swirl velocity is shown for each vortex with model results indicated with open squares and experimental results shown with closed squares. Again, there is close agreement between model predictions and experimental results (maximum 5% difference). The alternating swirl velocity values may be due to a slight difference blade manufacturing or base pitch. It appears that in the region of interaction, $x/D > 1$, the core radii decrease slightly as the swirl velocity increases slightly. Interestingly, this is contrary to what was observed in Sherry et al. [53] and may be a Reynolds number effect as low Reynolds number contributes to enhanced diffusion of vortical structures.

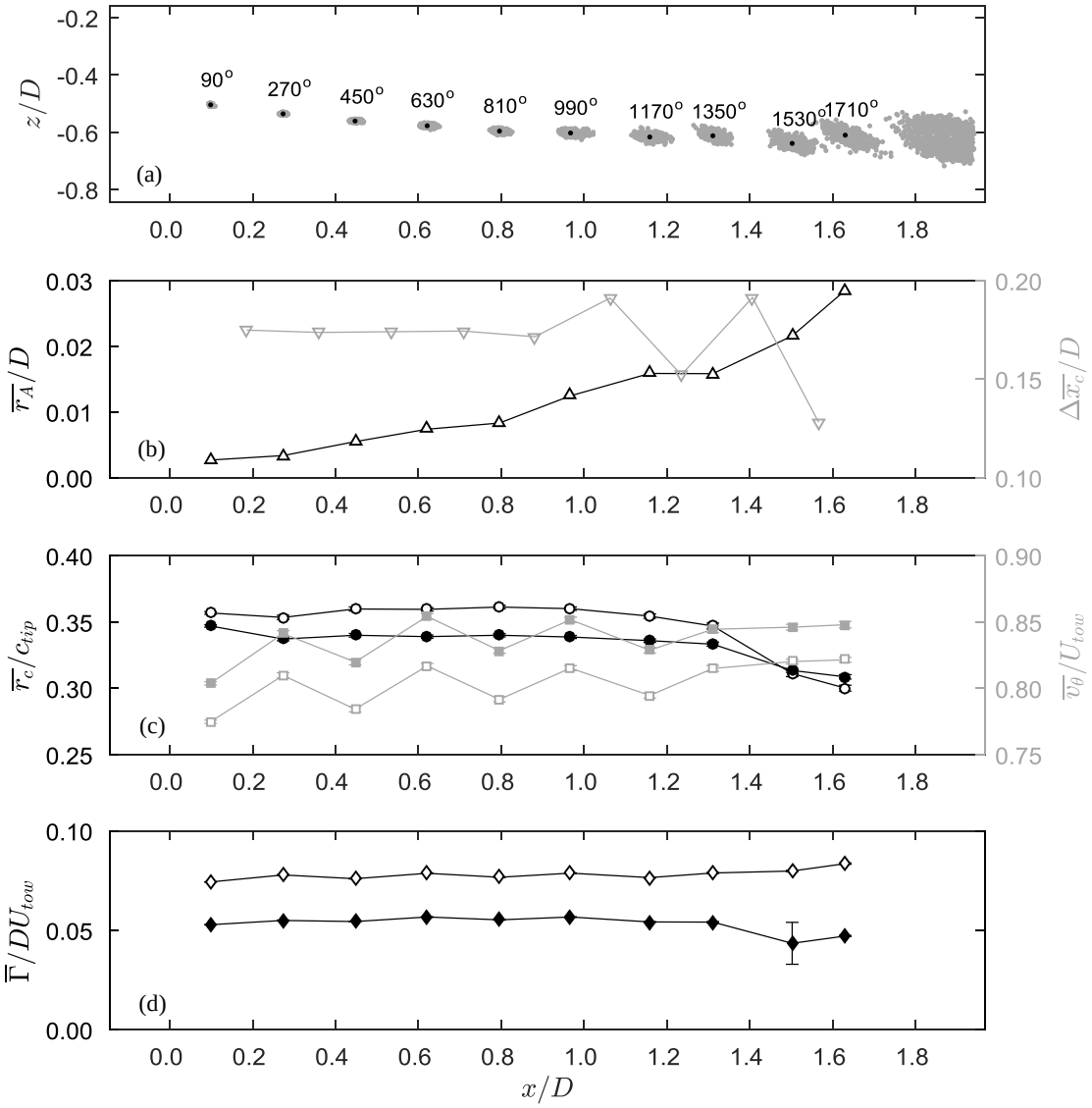

Figure 22: (a) Vortex center positions for each traceable vortex. The light gray markers represent the vortex centroid positions for each realization. The black markers represent the average centroid position. The left y-axis of Figure (b) shows the aperiodicity non-dimensionalized by the turbine diameter. The right y-axis shows the streamwise spacing between adjacent mean centroid positions. The left y-axis of Figure (c) shows the vortex core radius calculated from experimental data (closed circles) and determined from the vortex model fitting methodology (open circles). Both are normalized by the turbine blade tip chord length. The right y-axis of Figure (c) shows the mean swirl velocity calculated from experimental data (closed squares) and determined from the vortex fitting methodology (open squares). Figure (d) shows the average vortex circulation calculated for only the vortex core region from experimental data (closed diamonds) and determined for the entire vortex using the model fitting methodology (open diamonds). Both are non-dimensionalized by the turbine diameter and the towing carriage speed. Error bars are included in (c) and (d) with bar length equal to two times the standard deviation of the associated quantities, quoted at 95% confidence.

Figure 22d shows the mean circulation for each vortex, normalized by the turbine diameter and towing carriage speed, with the open diamond symbols representing the model output and the closed diamonds representing the experimental results. The circulation was calculated from the experimental data using the line integral[9] along the circular vortex core boundary. The vortex core radius was calculated from the data using the method of cuts, as previously described. The velocity values along the circle were interpolated when necessary using cubic spline interpolation. Neither data set shows significant variation in the near wake. Experimental values are approximately 70% of experimental values. This is because model values include all circulation associated with the vortex, assumed to be in otherwise quiescent flow. Experimental values only include the vorticity in the vortex core which accounts for approximately 70% of the total vorticity in laminar vortices and 40% in turbulent vortices [53, 64]. Indeed, the experimental circulation values for the present experiment are approximately 70% of the model values, suggesting that the vortices in this region are primarily laminar. There is also a slight disagreement between the two results in the interaction region at $x/D > 1.4$. This is likely due to the model assumption that the surrounding flow is quiescent.

[9] The area integral was also used to calculate the circulation and the two observations were found to be in very close agreement. Only the line integral results are included for brevity.

4.4.3 Turbulence statistics

The turbulence kinetic energy components of the 2-D Reynolds stress tensor were calculated using Equation 18 and are shown in Figure 23a. The Reynolds shear stress component was calculated using Equation 19 and is shown in Figure 23b. The turbulence intensity was calculated for streamwise and vertical components using Equation 17 and are shown in Figure 23c and Figure 23d, respectively.

Wake expansion is again clearly shown by the locations of the tip vortices. There is surprisingly little activity, in terms of any of the turbulence statistics, outside of the vortex core region. Intensity increases with wake age from the barely visible 90° vortex, to the region of strong interaction beginning with the 990° vortex ($x/D \approx 1$). Downstream, intensity decreases again as the area increases with increasing aperiodicity. Downstream of x/D = 1.8 the smeared, circular path of the leapfrogging vortices is clearly visible.

Figure 23a shows the turbulence kinetic energy normalized by the towing carriage speed, squared. It appears that the turbulence kinetic energy increases in magnitude with wake age although this is likely exaggerated by the increasing aperiodicity, as it is for all other turbulence statistics shown in Figure 23. Reynolds shear stress, also normalized by the square of the towing carriage speed and shown in Figure 23b, is similarly restricted to the region immediately surrounding the tip vortices. In the wake expansion region from the turbine downstream to a distance of $x/D = 1.2$, there appears to be a fairly even distribution of positive and negative Reynolds stress, which one might expect from a vortex with the upstream side transporting momentum from the wake to the mean flow and the downstream side transporting momentum in the opposite direction. Further downstream,

however, in the region of vortex interaction, the Reynolds shear stress is primarily negative. The turbulence intensity, normalized by the towing carriage speed and shown in Figure 23d and Figure 23e, appears very similar to the other turbulence statistics in that the activity is almost entirely restricted to the vortices though the expanding shear layer is shown more prominently. Both turbulence intensity components are plotted with the same contour range for quantitative comparison. The vertical component appears stronger, perhaps a function of increasing vertical movement of the vortices in the leapfrogging region. Also of note, the inflow turbulence intensity is negligible, in agreement with ADV measurements.

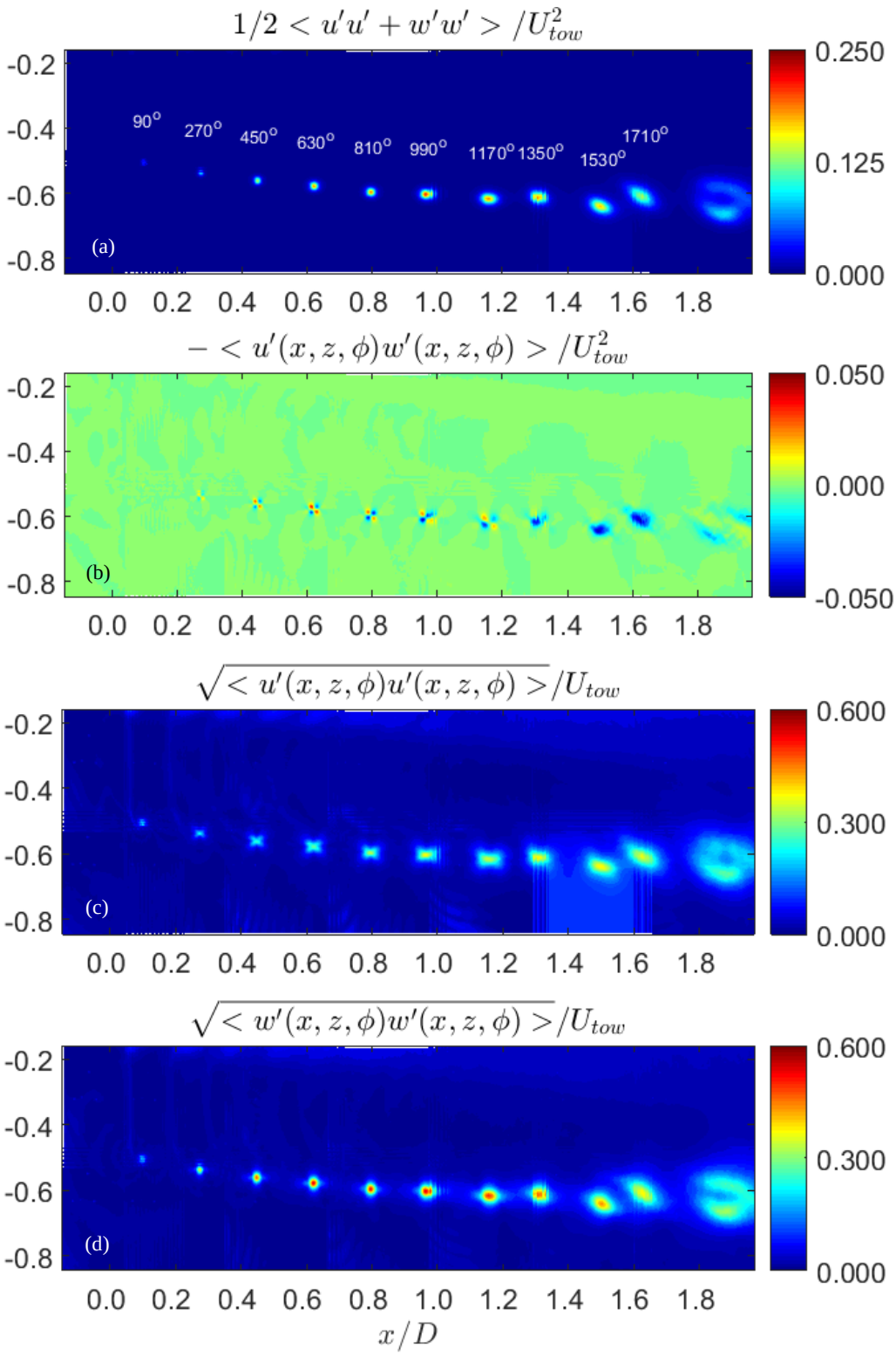

Figure 23: (a) The turbulence kinetic energy, (b) Reynolds shear stress, (c) streamwise velocity component turbulence intensity, and (d) vertical velocity component turbulence intensity. Reynolds stress components are normalized by U_{tow}^2 and turbulence intensity components are normalized by U_{tow}. Flow is from left to right.

All turbulence statistics shown in are blade phase averaged. As previously mentioned, aperiodicity results in an artificial contribution to the fluctuating velocity components, incorrectly interpreted as turbulence. Following the individual average methodology described in Ramasamy, Paetzel, and Bhagwat [64], a subregion (again, 21by 21 elements or about 40 mm by 40 mm) surrounding the nearest point to the vortex model-identified center was extracted for each vortex in each realization. These subregions were then overlaid, aligning the vortex centers, and the turbulent statistics were then recalculated. Representative results are shown in Figure 24.

The three vortices included in Figure 24 were selected because they show vortex development over a range of wake ages. Also, although every effort was made to faithfully tile adjacent fields of view together, there were small variations in the overlapping region, thus vortices were selected from outside the overlapping region so as not to be influenced by any potential misalignment.

The results in Figure 24 show that the majority of the turbulence shown in Figure 23 is due to random variation in the vortex center position. For example, for the 810° vortex, the maximum turbulence kinetic energy of the aligned subregion is approximately 10% of what it is for the phase-averaged case. The aligned Reynolds shear stress is roughly 9% of the unaligned for the same vortex. The individually averaged values are 48% and 30% of the phase-averaged values for the streamwise and vertical turbulence intensity components, respectively.

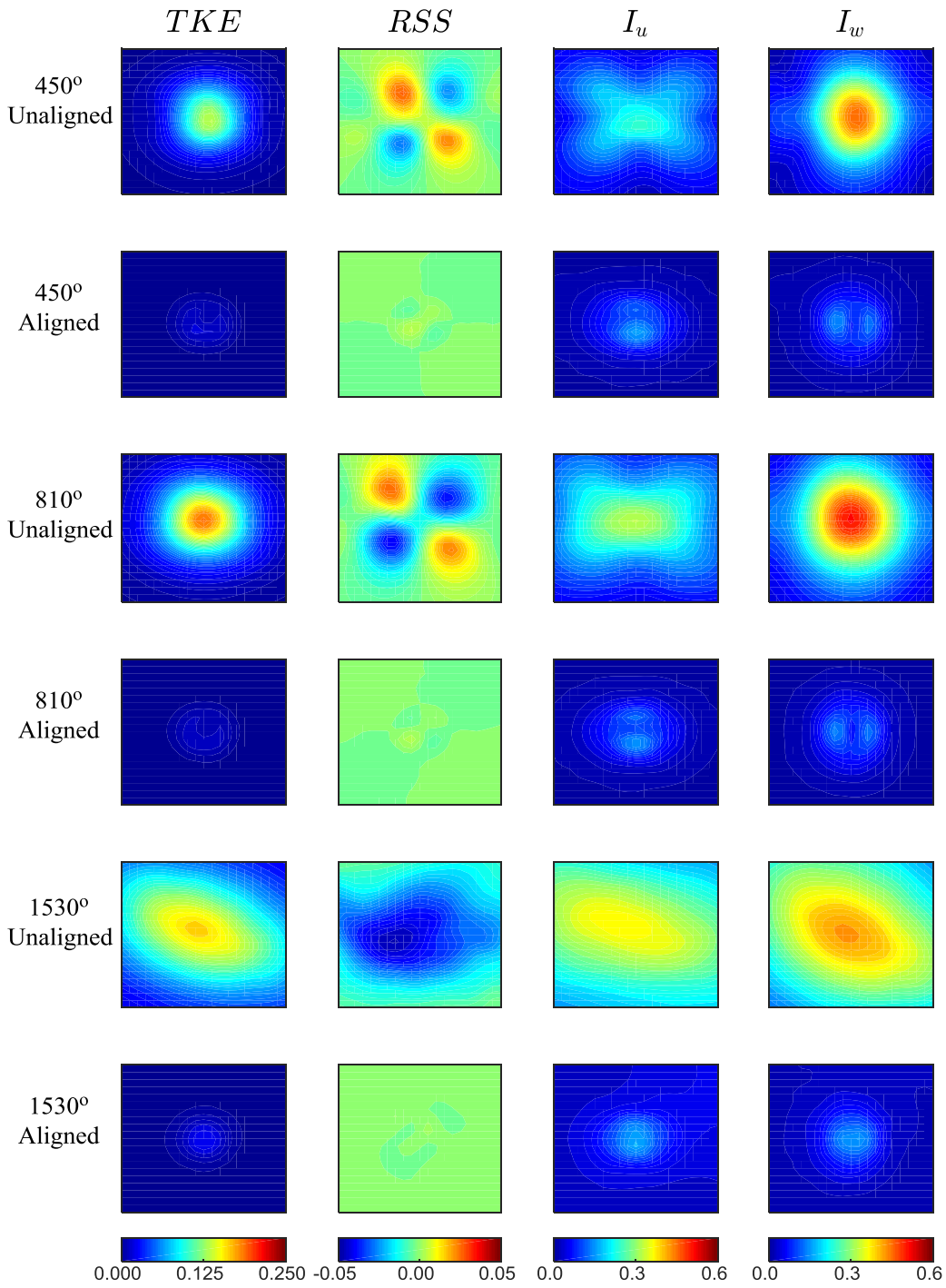

Figure 24: The results of individual averaging on turbulence statistics are shown for three individual vortices: 450º (top two rows), 810º (middle two rows), and 1530º (bottom two rows), respectively. In the columns, each of the turbulence statistics are presented: turbulence kinetic energy (TKE), Reynolds shear stress (RSS), Streamwise Turbulence Intensity (I_u), and vertical turbulence intensity (I_w). The first row of each pair shows the phase-averaged (unaligned) vortex core. The second row of each pair shows the individual average (aligned) result.

An alignment correction cannot be applied to the entire field of investigation because the aperiodicity is different for each vortex. Even in cases when there are two vortices in a single field of view, the correction for one is not the same as for the other. However, to better show trends in the individually averaged turbulence statistics, the effect of aperiodicity was removed by aligning the centers for each vortex in each realization, recalculating the turbulence statistics, and calculating the maximum value (or in the case of the Reynolds shear stress the maximum and minimum values) for the subregion. These results are shown in Figure 25.

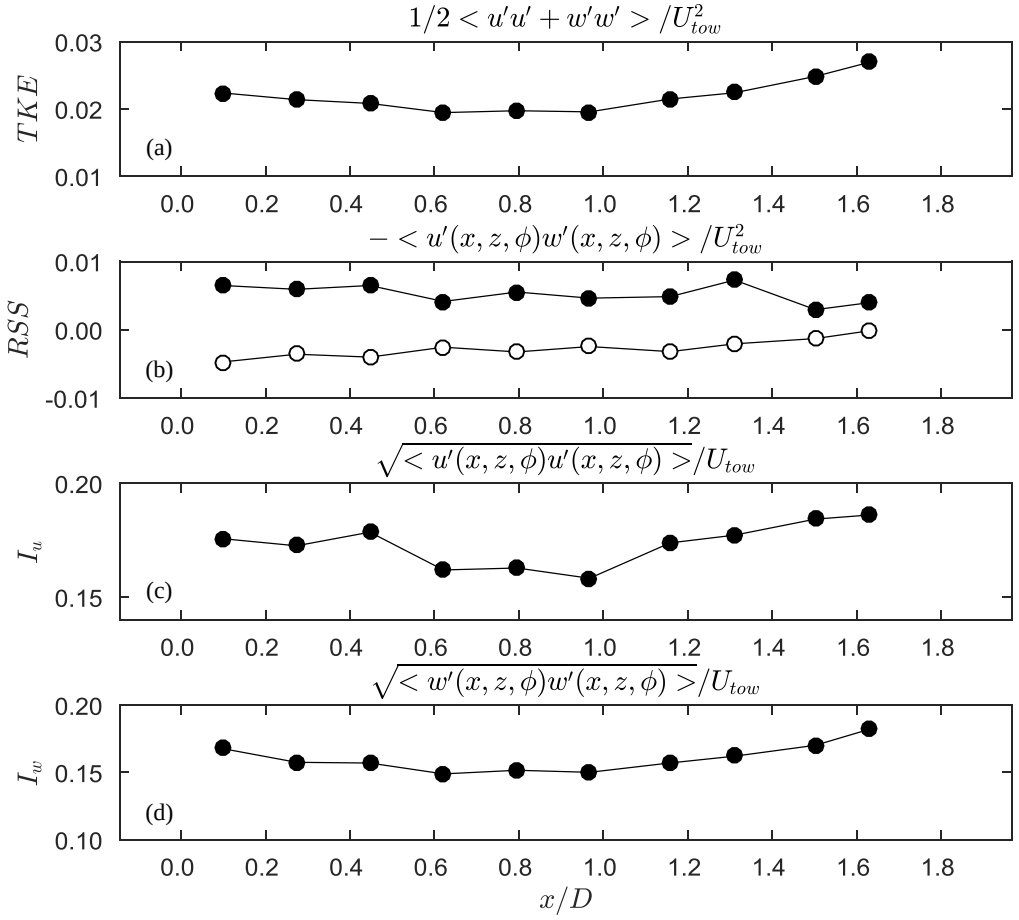

Figure 25: The maximum value for the subregion surrounding each vortex, individually averaged for the (a) turbulence kinetic energy, (b) Reynold shear stress, also including the negative component shown as open circles, (c) the streamwise component of turbulence intensity, and (d) the vertical component of turbulence intensity.

Once the effect of the aperiodicity is removed, the interpretation of the turbulence statistics, as shown in Figure 23 changes significantly. The maximum values for the aligned averages are much lower as seen by comparing Figure 23a and Figure 25a. Moreover, where the phase-averaged results show an increase in turbulence kinetic energy followed by a decrease in the leapfrogging region, the individually averaged results show the opposite trend with turbulence kinetic energy increasing in the leapfrog region, once the contribution of aperiodicity is accounted for. Comparing Figure 23b and Figure 25b, the phase-averaged results indicate a change of sign in the Reynolds shear stress occurring just downstream of $x/D = 1.2$ in the vortex interaction region. This, however, is in contrast to the individually averaged results which show a persistent and stronger positive value, decreasing slightly in the leapfrogging region but not changing to wholly negative, as shown in Figure 23b. Even more surprising is the comparison of the components of the turbulence intensity. In Figure 23c and Figure 23d, the vertical component is shown to be stronger, however, referring to Figure 25c and Figure 25d, this is likely due to greater center location variability in the vertical direction. In the individually averaged case, the two components are roughly equal.

These results emphasize the need to view the phase-averaged turbulence statistics with caution. Their interpretation is perhaps in some way based on the definition of turbulence itself. Are the random movements of the vortex filaments turbulence in the classical sense? For example, is the Reynolds stress indicated by the phase average values indicative of momentum transport? Or is aperiodicity a component to be addressed separately in the form of the decomposition suggested by Reynolds and Hussein:

$$u_i(t) = \overline{u_i} + \widetilde{u_i}(t + nT) + u_i'(t) + u_{A_i}'(t) \qquad (21)$$

where $u_{A_i}'(t)$ represents the random fluctuations associated with aperiodicity. This question represents an opportunity for future study under conditions in which 3D time-resolved data could be obtained to calculate the specific contribution of each term in Equation 21 and momentum transport could be determined.

Regardless, it is surprising how little the turbulence statistics change in the near-wake region. Outside of the instability manifested by vortex meandering or aperiodicity, the near wake appears to be very stable, in keeping with the observations made by Lignarolo et al. [52, 56].

4.5 Conclusions

A study was conducted of the near-wake of a two-bladed, 0.8 m diameter, near-Reynolds number independent axial flow hydrokinetic turbine in steady flow conditions, one of the largest-scale wake surveys to date. The field of investigation extended from approximately 0.1D upstream of the turbine to 2.0D downstream, and radially outward to a distance of 0.85D. High resolution flow field observations were made using 2-D planar

PIV enclosed in an in-house designed and manufactured submersible housing system. Phase-averaged flow field results supported many previous observations made for smaller-scale models. These included the slowing of the flow just upstream of the turbine to 75% of the free stream velocity due to the increase in static pressure, wake expansion well-described by the 1/3 power of the streamwise distance, and the velocity deficit reaching a maximum of 1/3 the free stream velocity. Turbine blade root vortices were also observed but to a very limited extent given the limits of the field of investigation.

Tip vortex characterization techniques developed for helicopter rotor research were applied to calculate relevant vortex parameters. Spacing of adjacent vortex filaments was relatively constant as was vortex core radius to a streamwise distance of approximately 1.0D. Further downstream vortex interaction and mutual induction were observed followed by the first 90° rotation of leapfrogging, the phenomenon that likely initiates wake re-energization.

Phase-averaged turbulence statistics were calculated for the entire field of investigation and compared to individually averaged results in the active region immediately surrounding each vortex. Individually averaged turbulence statistics were lower by as much as an order of magnitude and were shown not to follow the same trends as the phase-averaged results. This demonstrates that vortex center aperiodicity can have a profound effect on the interpretation of results and should be considered in their evaluation.

5 Wake survey under unsteady conditions

5.1 Introduction

Even as the technology matures and the installed capacity increases, the design of a marine hydrokinetic turbine installation is likely to be unique to the installation site, reflecting the wide variation in environmental factors such as bathymetry, wind and tidal currents, the presence of flora and fauna, and proximity to shipping traffic, to name but a few. If presence in the associated literature is any indication, the impact of waves in particular is at best a secondary concern. However, in previous studies (e.g. [26, 38]) it has been shown that a small induced wave velocity, compared to the local current speed, can have a significant impact on the instantaneous performance characteristics of the turbine ultimately affecting power quality and the structural longevity of the turbine. Moreover, a significant effort has been expended to characterize the wake of marine hydrokinetic turbines, singly and in an array of multiple turbines, in an effort to maximize power production and minimize installation and maintenance costs. However, to date no work has been done on examining the impact of surface waves on wake characteristics to determine the extent to which they impact wake breakdown and subsequent re-energization, a process critical to determining array position and spacing.

5.2 Abstract

Flow field results are presented for the near-wake of an axial-flow hydrokinetic turbine in the presence of surface gravity waves. The turbine is a 1/25 scale, 0.8 m diameter, two bladed turbine based on the U.S. Department of Energy's Reference Model 1 tidal current turbine. Measurements were obtained in the large towing tank facility at the U.S. Naval Academy with the turbine towed at a constant carriage speed, with a tip speed

ratio selected to provide maximum power. The turbine has been shown to be nearly scale independent for these conditions. The selected wave form was intended to represent oceanic swell encountered off the U.S. eastern seaboard. The resulting model wave is a deep water wave, in terms of relative depth, traveling with the "current", in the opposite direction of the towing carriage. Velocity measurements were obtained using an in-house designed and manufactured, submersible, planar particle image velocimetry (PIV) system at streamwise distances of up to two diameters downstream of the rotor plane. PIV ensembles were obtained for phase locked conditions with the reference blade at the horizontal position. Phase averaged results for steady and unsteady conditions are presented for comparison showing further expansion of the wake in the presence of waves as compared to the quiescent case. The impact of waves on turbine tip vortex characteristics is also examined showing variation in core radius, swirl velocity, and circulation with wave phase. Some aspects of the highly coherent wake observed in the steady case are recognized in the unsteady wake, however, the unsteady velocities imposed by the waves, particularly the vertical velocity component, appears to convect tip vortices into the wake, potentially enhancing energy transport and accelerating the re-energization process. A new characteristic length scale, the shear layer half width, is proposed to describe the spatial extent of the unsteady wake.

5.2.1 Literature review

A review of performance testing for axial-flow marine hydrokinetic turbines in steady conditions is included in Section 2.2.1. A review of performance testing for turbines in the presence of surface gravity waves is included in Section 3.2.1. A review of turbine wake surveys under steady conditions is provided in Section 4.2.1.

To the author's knowledge no studies have yet been published on the influence of surface gravity waves on the near-wake of an axial-flow marine hydrokinetic turbine.

5.2.2 Present work

The goal of the present study to assess the impact of surface gravity waves on the near-wake of an axial-flow marine hydrokinetic turbine, to compare characteristic length scales, describe wake evolution through the change in turbine tip vortex characteristics, and to consider the difference in energy and momentum transport as compared to the steady case. In several previous studies [52, 53, 55, 60] it was shown that adjacent vortex filament interaction is likely the mechanism that initiates the breakup and subsequent re-energization of the wake. It is as yet unclear what impact surface waves might have on tip vortex helical pitch and the downstream distance at which this occurs.

5.3 Experimental details

The towing tank, turbine, and performance measurement equipment are discussed in detail in Section 2.2. A description of the PIV system, including development, dimensions, settings, and details regarding processing and post-processing is included in Section 4.3.

The same deep-water wave (h/λ = 0.6) featuring a significant wave height of 0.18 m and a period of 2.3 s used in a previous study [26] was also used in the present experiment to allow for quantitative comparison. A description of the wave, including scaling considerations and associated velocities is included in Section 3.3. The group speed of the waves was in the same direction as the simulated current, opposite the direction of the towing carriage (i.e. head seas).

As described in Chapter 4, for the wake survey under steady conditions, the PIV equipment (i.e. the forward and side-looking submersibles containing the laser light-arm and optics, and the camera, respectively) was fixed in position relative to the towing carriage and the position of the turbine was changed in order to change the field of view. This was accomplished by moving the surface-piercing strut relative to the towing carriage. In the case of the present study, the turbine was fixed in position and the PIV equipment (i.e. side-looking submersible) was moved relative to it in order to change the field of view in order to maintain the same wave-induced velocity shear for each field of view. The target board, indexed to the turbine, was used to provide absolute position reference between fields of view.

Due to limitations on the depth at which the PIV equipment could be positioned, the turbine was positioned as close to the free surface as possible while remaining below the depth at which the free surface impacts performance, also allowing for the amplitude of the wave. See Section 2.3 for details on the determination of the critical depth. The horizontal and vertical velocity profiles for the maximum wave-induced velocity are shown as solid black lines in Figure 26, with the gray horizontal band representing the vertical extent of the turbine and position within the water column, thus indicating the anticipated velocity

shear. The maximum horizontal and vertical wave velocities seen by the turbine was about 5% of the towing carriage speed, slightly higher than previous experiments[10] due to the reduced distance between the turbine and the free surface.

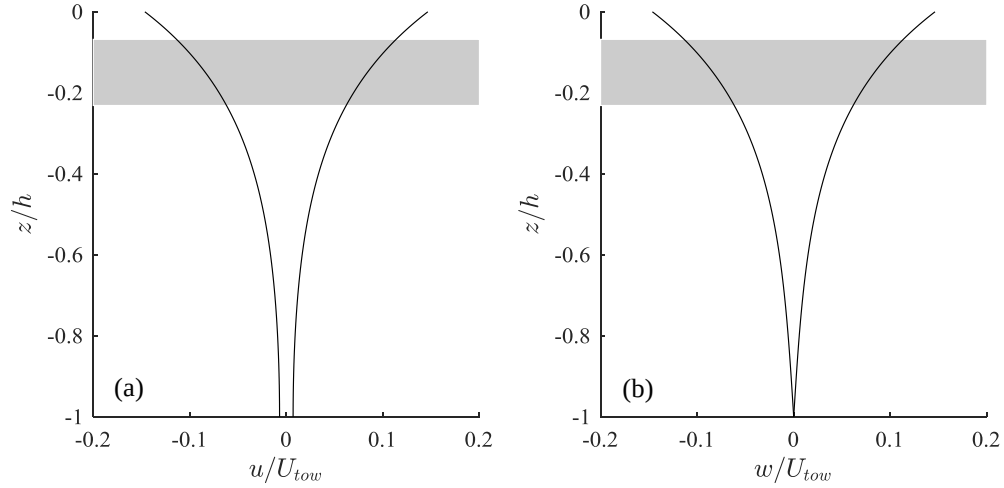

Figure 26: (a) Wave induced velocity shear in the horizontal and (b) vertical direction, normalized by the towing carriage speed. The gray shaded region indicates the vertical extent of the turbine relative to the tank depth and thus the velocity shear experienced by the turbine, approximately 5% of U_{tow} for the horizontal wave velocity.

Two regions were selected for measurement: one just adjacent to the rotor plane ($0.0 < x/D < 0.4$) and one in the region of vortex interaction, as noted in the steady case ($0.1.3 < x/D < 2.0$). Ten traverses of the towing tank were made at each of the six fields of view resulting in approximately 1,000 realizations at each position. Each traverse provided approximately 30 s of data including the passage of approximately 20 waves. As with the wake survey in steady conditions, blade position was used to trigger image capture, thus all realizations are blade-phase averaged with the turbine oriented horizontally.

[10] The maximum horizontal wave velocity component experience by the turbine in the previous study was 9% of U_{tow}. The maximum vertical velocity component was 3.5% of U_{tow}.

5.4 Results and Discussion

5.4.1 Turbine blade phase average

Velocity field measurements were averaged at each field of view and then tiled together using the methodology described in Section 4.3, yielding a blade phase average, $< u(x, z, \phi_b) >$, which was normalized by the towing carriage speed, U_{tow}. Results from the steady case are shown in Figure 27a (repeated from Figure 20a) for comparison to results from the unsteady case, shown in Figure 27b. Wave 1 (h/λ = 0.6) was used in the unsteady case.

The two fields are similar with regard to the general shape of the wake and range of velocities, however, there are a number of striking differences. Vortex center position, highly repeatable in the steady case, is substantially less so in the unsteady case, with positional stability decreasing rapidly with streamwise distance even in the region nearest the turbine. By x/D = 1.3, the individual vortices are completely obscured; smeared beyond recognition. The wake width (i.e. $\delta_W(x)$ where $u(x) = 0.99U_{tow}$) is also notably larger and the area of minimum velocity shifted significantly inward toward the rotor centerline.

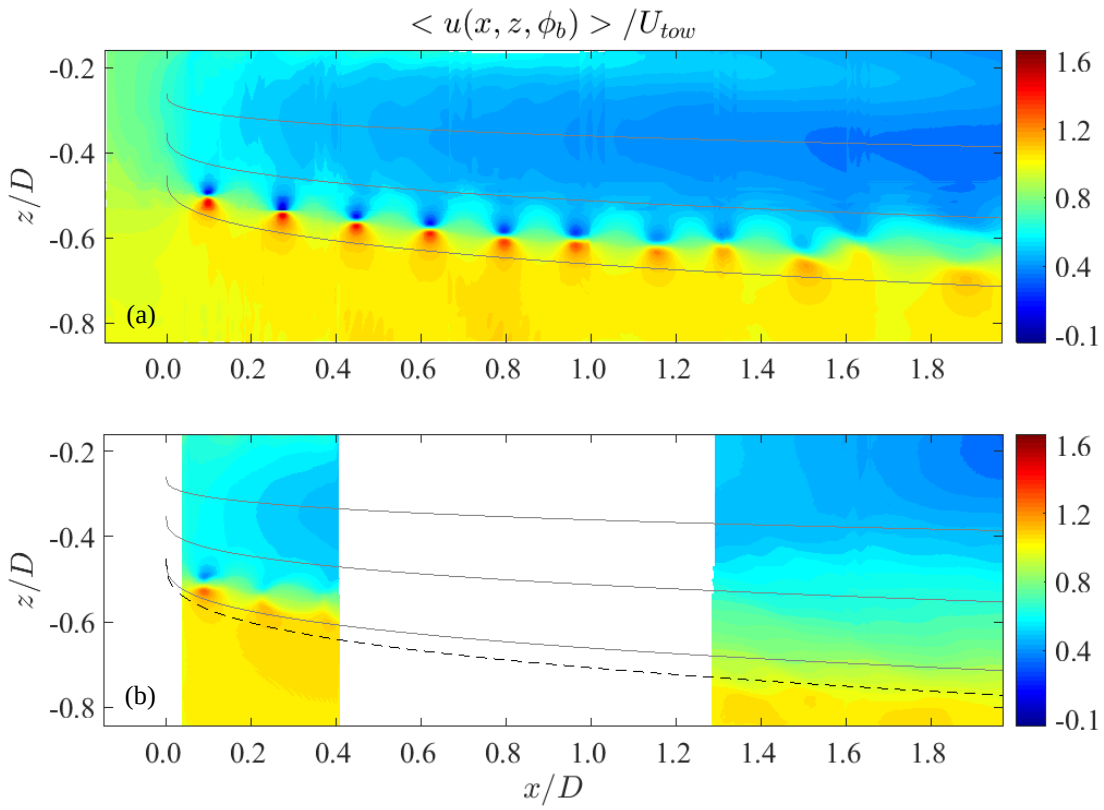

Figure 27: (a) Blade phase average streamwise velocity in steady and (b) unsteady conditions. Figure (a) is a repeat of Figure 20a, included for comparison. The gray profile lines indicate, from top to bottom, the maximum velocity deficit contour, the wake half-width, and the wake width for the steady case, respectively. The length scales are repeated on (b) for comparison. Additionally, the dashed black line indicates the wake width for the unsteady case. Wave 1 (h/λ = 0.6) was present in the unsteady case. Flow is from left to right.

The solid gray lines shown in Figure 27a indicate several characteristic length scales, originally developed to describe the canonical axisymmetric wake formed behind round objects such as spheres and disks, but employed here to describe the spatial extent of the turbine wake with good effect. The upper-most contour describes the length, δ_S at which maximum velocity deficit:

$$U_s(x) = \max(U_{tow} - u(x)) \qquad (22)$$

occurs. The bottom-most line in Figure 27a is the wake width or wake boundary, δ_W as defined above. The contour between them is defined in Pope [57] as the wake half width,

$\delta_{1/2}$ or the the length at which the velocity is equal to $U_{tow} - \frac{1}{2}U_s(x)$. In this case, the wake half width reasonably represents the dividing line between the wake core above and the shear layer below. Contours were created by extracting streamwise velocity profiles at streamwise locations midpoint between vortices in order to minimize their influence. For each streamwise velocity profile, the z-coordinate location was identified corresponding to $U_S(x)$ and $0.99U_{tow}(x)$. These points were then fitted with a 1/3 power-law fit, proportional to the velocity deficit flow rate [57], and shown in previous studies (e.g. [45]) to accurately represent the wake velocity profile. An additional contour, the mean vortex center contour, δ_V – a 1/3 power-law fit made to the mean vortex center positions in the steady case – is proposed, as discussed below.

The wake width for the unsteady case was calculated using the method described above. Comparing the two contours in Figure 27b, the steady case, depicted as the bottom-most solid gray line, and the unsteady case, depicted as a dashed black line, the wake boundary in the unsteady case is expanded slightly outward (in the negative z-direction) compared to the steady case. Identifying δ_S and $\delta_{1/2}$ for the unsteady case, however, is much more problematic because the region of maximum velocity deficit is shifted inward toward the turbine output shaft, making the contour created by mapping it less useful as a descriptor. As it depends on the location of δ_S, $\delta_{1/2}$ could not be calculated either. To illustrate why this is, the streamwise velocity profiles for several downstream distances were calculated are shown in Figure 28b.

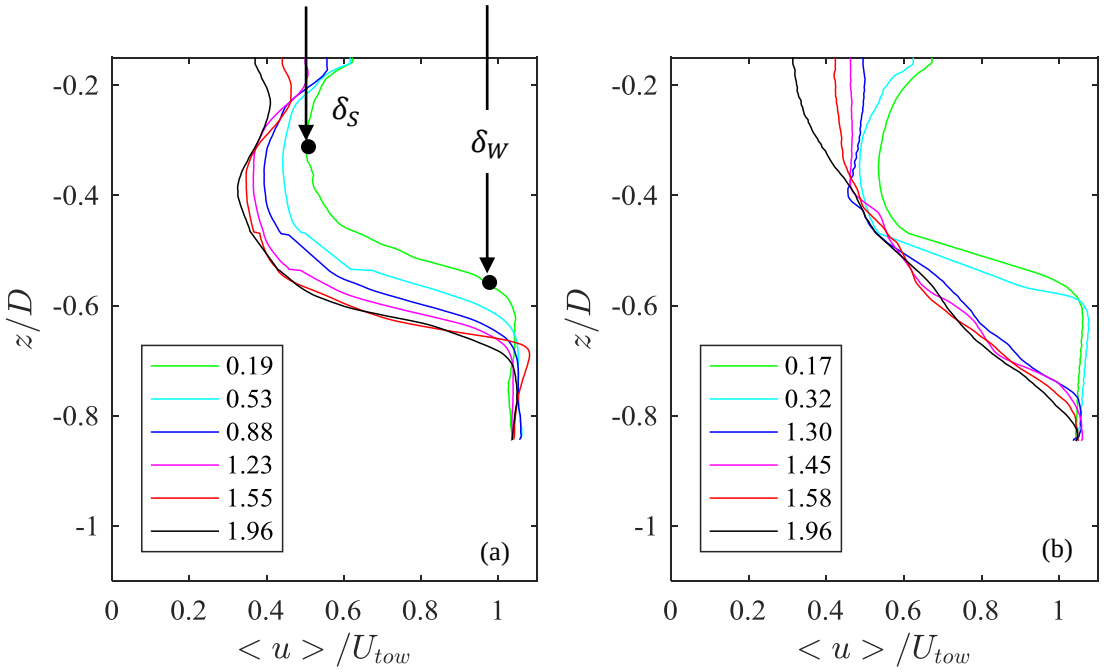

Figure 28: (a) Turbine blade phase-averaged velocity profiles for the steady and (b) unsteady cases. Legend values indicate the non-dimensional downstream distance from the turbine, x/D. Wave 1 (h/λ = 0.6) was present in the unsteady case. Annotations indicate the maximum velocity deficit location, δ_S and wake width, δ_W.

The velocity profiles depicted in Figure 28a look very much like the classical axial-flow turbine wake with U_S, δ_S, and δ_W all increasing with streamwise distance due to wake expansion.

The first two velocity profile contours in Figure 28b are similar to those in the steady case showing relatively high velocity shear just inside the wake boundary. However, further downstream ($x/D > 1.3$) the wake has become nearly self-similar in all but the inner wake core region, the wave action again having smeared out the comparatively strong velocity shear shown in the steady case.

Likewise in the vertical direction, Figure 29 shows the blade phase-averaged vertical velocity $< w(x, t, \phi_b) >$ for the steady (Figure 29a) and unsteady (Figure 29b) cases. Similar to the figures describing the streamwise velocity (Figure 20b), the much of

the positional stability of the tip vortices shown in the steady case, is lost in the wave case. In fact, there is almost no bulk motion in the vertical direction in the downstream region of Figure 29b. However, as with previous experiments, the average value, in this case the turbine blade phase average value, obscures the rich dynamic action of the system, as discussed shortly.

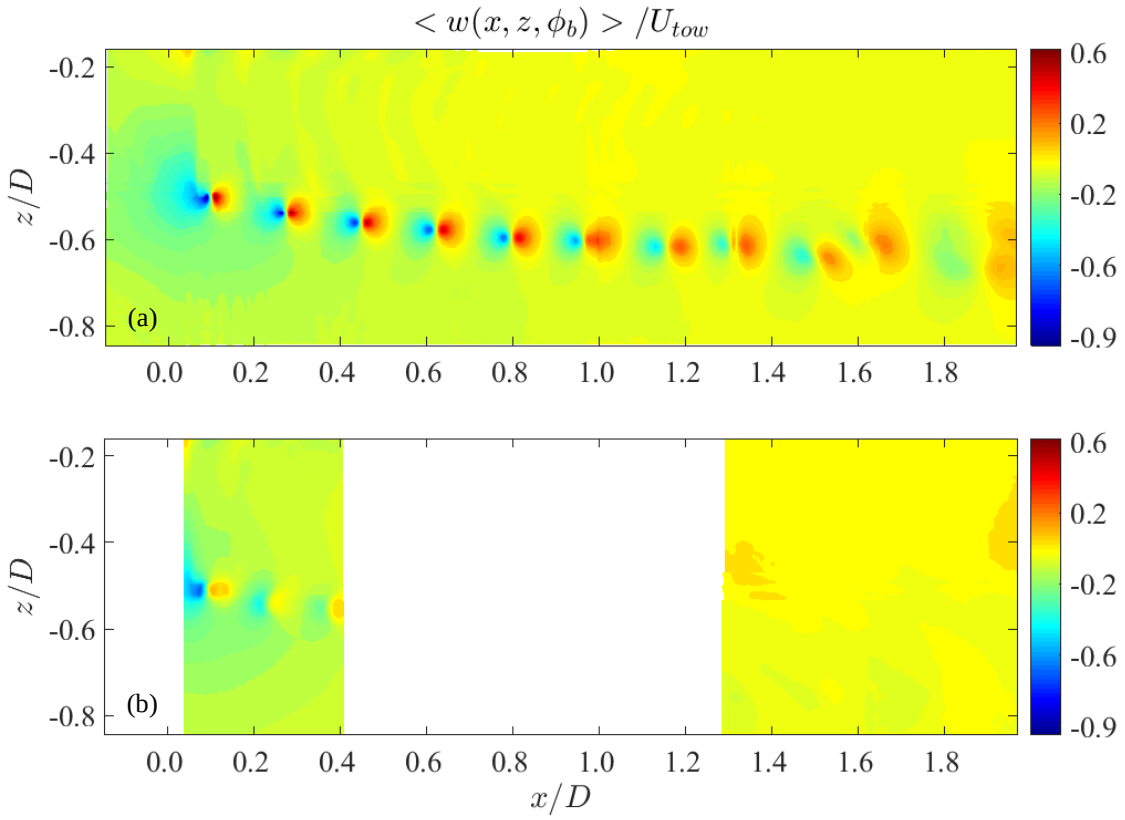

Figure 29: (a) Blade phase average vertical velocity in steady and unsteady (b) conditions. Figure (a) is a repeat of Figure 21a, included for comparison. Wave 1 (h/λ = 0.6) was present in the unsteady case. Flow is from left to right.

5.4.2 Blade and wave phase average velocity

In order to assess the impact of wave phase, the data was transformed from time- to phase-space using the Hilbert transform as discussed in Section 3.3. Each realization

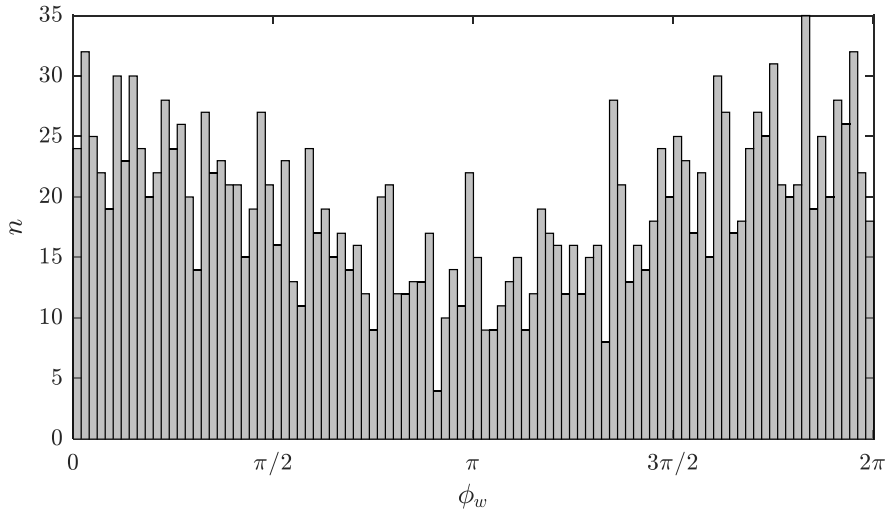

Figure 30: Histogram of wave phase at the turbine to the number of realizations recorded at that phase for a representative field of view. Bin width is $\pi/50$ radians (3.6°).

was correlated with a wave phase from 0 to 2π referenced to the turbine location where the wave height sensor was located.

Figure 30 shows a histogram of the number of realizations captured at each wave phase for a representative field of view. PIV image capture was initiated via a Hall Effect sensor on the rotor nacelle, as previously discussed. As shown in Figure 13b, the shaft-rotation speed (non-dimensionalized as TSR) varies considerably with wave passage, thus the distribution of images was not even across all wave phases. In other words, the phase average values included in Figure 28b and Figure 29b are more heavily weighted toward realizations captured near peak shaft speed than near the lowest shaft speed. Although approximately 1,000 realizations were captured for each field of view, recall that in Figure 19 it was shown that approximately 800 realizations were needed for a statistically meaningful blade-phase average, thus turbulence statistics were unobtainable. However, examining many of the wake characteristics as a function of wave phase does provide useful insight into the complex wake environment.

The blade and wave phase averaged streamwise velocities were calculated and are shown in Figure 32 and Figure 33 at wave phase angles[11] from 0 to $3\pi/4$ and π to $7\pi/4$ in increments of $\pi/4$ radians, respectively. Each field of view is composed of an average of approximately 20 realizations. For reference, the Figure 31shows the surface elevation profile for an entire wavelength for each wave phase. The rectangle in the lower left-hand corner represents the field of investigation. Its depth relative to the free surface (shown as a horizontal solid black line), and its length compared to the wavelength are all shown to scale. The wave amplitude has been enlarged by a factor of five for the sake of clarity.

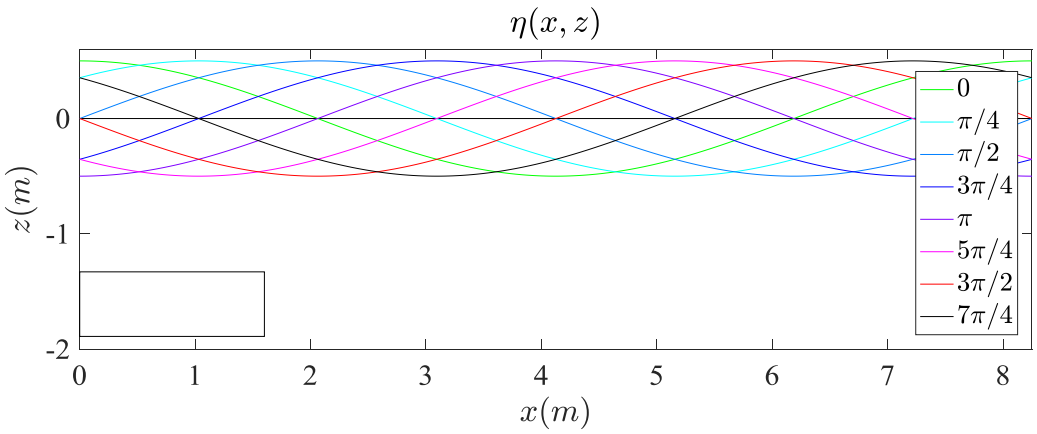

Figure 31: Free surface elevation versus wave phase. The field of investigation, to scale relative to the depth and wavelength, is shown in the lower left-hand corner. Wave heights are exaggerated by a factor of five for clarity.

In the downstream region nearest the turbine ($0 < x/D < 0.4$), wave influence is minimal as expected from the relative coherence of the vortices shown in Figure 27b. There is, however, a small undulation in the wake boundary and the tip vortices can be seen to trace an elliptical path similar to what would be expected for a submerged particle influenced by waves.

[11] Each bin was +/- $\pi/36$ or 2.5°.

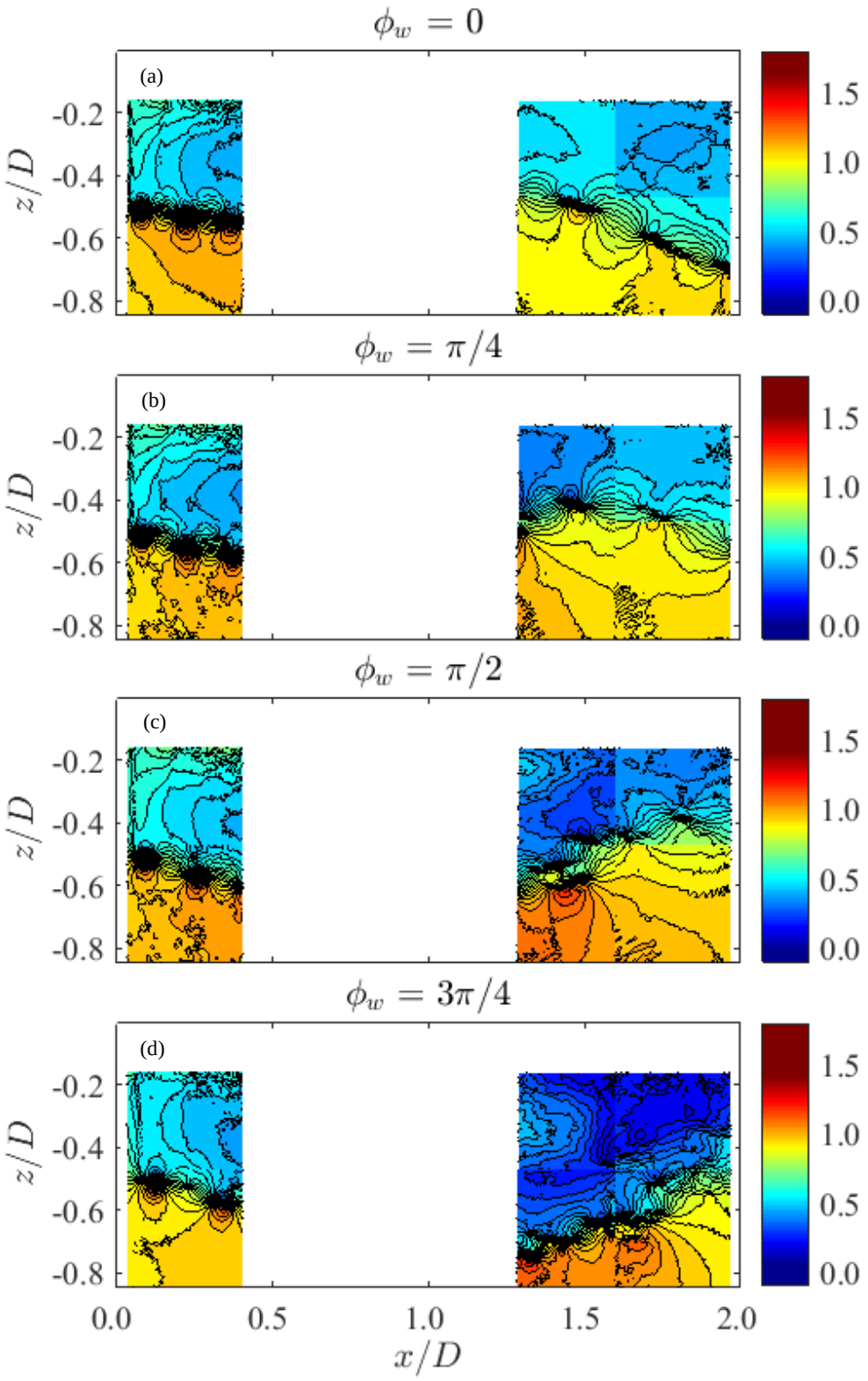

Figure 32: Blade and wave phase averaged streamwise velocity contours for wave phase angles from 0 to $3\pi/4$. Wave phase is referenced to the location of the turbine. Flow and wave propagation direction is from left to right.

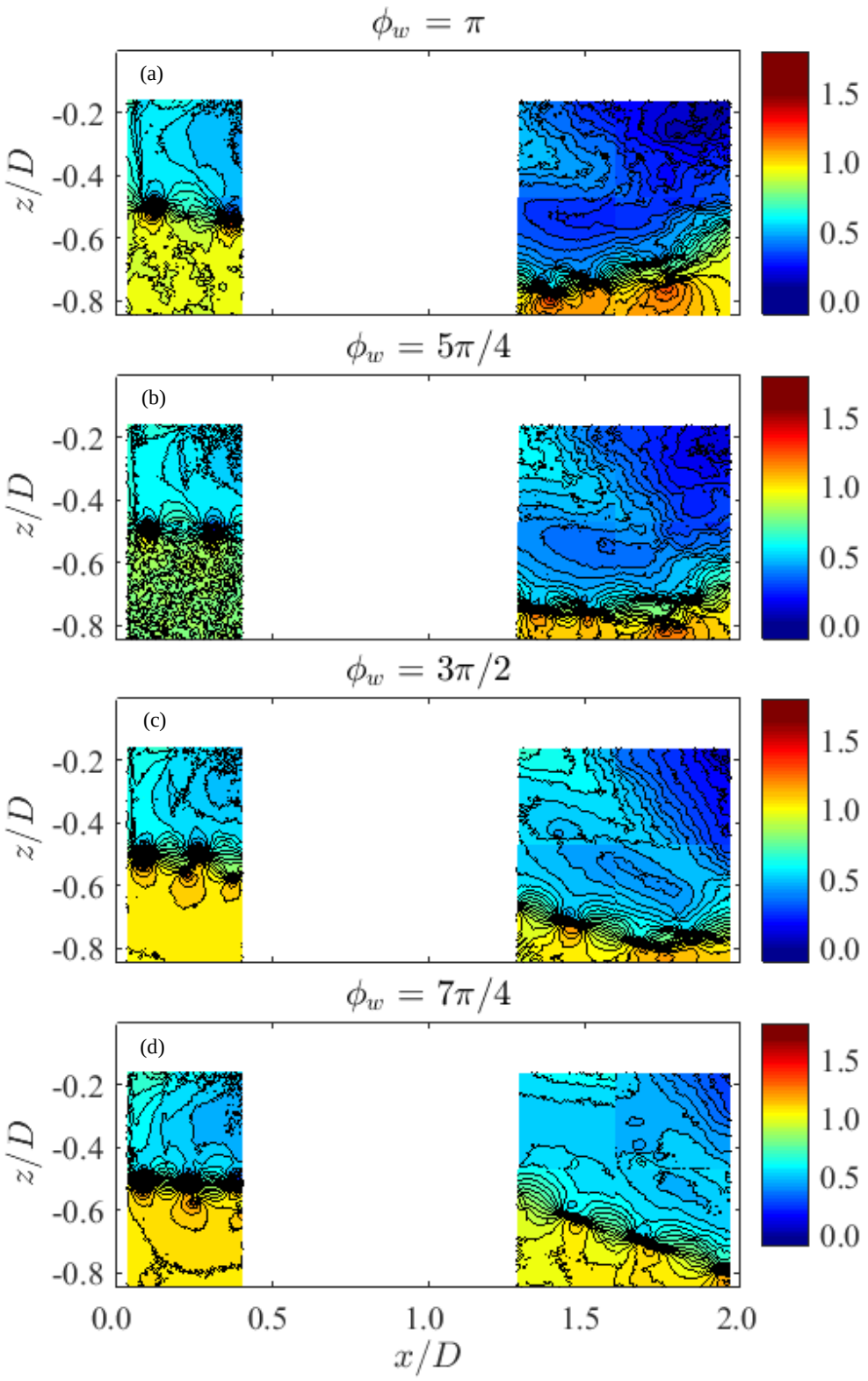

Figure 33: Blade and wave phase averaged streamwise velocity contours for wave phase angles from π to $7\pi/4$. Wave phase is referenced to the location of the turbine. Flow and wave propagation direction is from left to right.

Upon first inspection, vortex center positions may seem counterintuitive in the case of $\phi_w = 0$ (Figure 32a). At the wave peak the horizontal component of the velocity is also at its peak value, thus the turbine sees the highest horizontal velocity at this wave phase. One might reasonably expect this to drive the vortex centers apart. However, it should be noted that as horizontal velocity increases, turbine rotation speed also increases, thus decreasing the pitch of the tip vortex helix. The opposite is true with wave trough passage at $\phi_w = \pi$ (Figure 33a). Though the magnitude of the horizontal velocity is at its lowest with trough passage, vortex helix pitch is greatest due to a commensurate decrease in turbine rotation speed. This is significant because it has been observed that the downstream distance at which adjacent vortex filaments interact and the stable helical tip vortex structure begins to break down is a strong function of the vortex helix pitch [55, 53]. It might reasonably be assumed that as the adjacent vortex filaments are moved closer together by the horizontal wave velocity, that this may decrease the downstream distance at which mutual induction occurs.

In the region further downstream ($1.3 < x/D < 2.0$) the blade and wave phase averaged field of view appears much clearer, comparing more closely with Figure 27a than Figure 27b. Granted, there are only approximately 20 realizations incorporated to each field of view. However, this suggests that, like the overall average performance measures discussed in Chapter 3, blade phase averaging is likely not a full description of this periodic phenomenon. The wake boundary is shown to undulate with the passing wave reaching its highest vertical extent of approximately -0.65D at $x/D = 2$ and $\phi_w = \pi/2$[12] (Figure 32c).

[12] The wavelength of wave 1 is 8.25 m, thus 2D downstream is slightly less than 1/4 of the wave length. The wave phase is referenced to the turbine, thus the peak height of the boundary layer lags the turbine by approximately 1/4 of a wave period or $\pi/2$.

The wake boundary continues to move downward in the negative z-direction until the passing of the wave trough at x/D = 2 and $\phi_w = 3\pi/2$ (Figure 33).

Unfortunately, the wake boundary is out of the field of view under these conditions, however, if the vertical extent of the wake boundary movement can be estimated by the movement of the vortices, the total vertical displacement of the wake boundary layer at $x/D = 2.0$ is approximately 0.4D. For comparison, the vertical displacement of a particle located at the same depth under the same wave conditions would be 0.05D.

5.4.3 Vortex characterization

Although they do not likely describe the flow with a high degree of fidelity, tracking vortex centers as they traverse the near wake can provide a useful estimate for the length scale of the shear layer, especially in unsteady conditions. Moreover, the spatial change of vortex parameters such as core radius, peak swirl velocity, and circulation can provide additional insight into the complex interactions in the near wake.

Using the same methodology described in Section 4.4, the center position of each vortex present in approximately 6,000 realizations was determined along with relevant characteristics. These vortex center positions were plotted at their respective spatial location with the color of each marker indicating the wave phase at the turbine (Figure 34). Again, $\phi_w = 0$ represents a crest, $\phi_w = \pi$ represents a trough, and $\phi_w = 2\pi$ represents the next crest. The vortex center positions for the steady case are plotted in gray for reference.

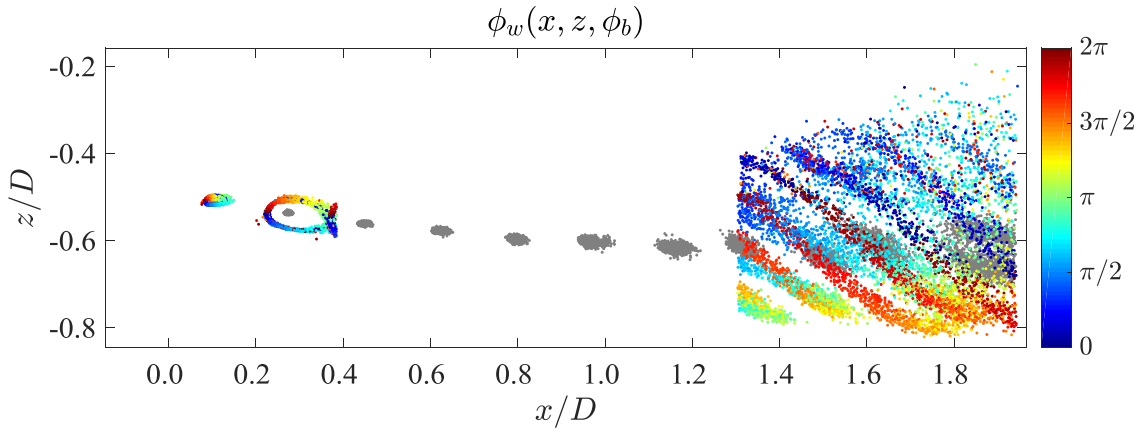

Figure 34: Blade phase-locked vortex center positions for the unsteady case. Marker color indicates wave phase from the wave crest (ϕ_w = 0) to trough ($\phi_w = \pi$) and to peak again ($\phi_w = 2\pi$). Blade phase-locked vortex center positions for the steady case included as gray markers for reference. Flow is from left to right.

The vortices are created at approximately $x/D = 0$. Even over a comparatively short streamwise distance, the impact of the wave and wake can be seen in the elongated elliptical shape of the vortex center locations for the 90° [1st group of] vortices. This effect is even more pronounced for the 270° [2nd group of] vortex centers, showing a significantly larger stretched elliptical path. In addition to expanding and stretching, the vortex centers associated with the 270° vortex also appear to be rotating the clockwise (the negative y-direction) with downstream distance. This deformation is due to the influence of the uniform stream, wake shear layer, and wave velocity. The effect is even more pronounced at a downstream distance of $x/D > 1.3$ where the ellipse has rotated to approximately -45° from the x-axis, the rotation angle a function of the magnitude of the streamwise velocity shear, $\partial u/\partial z$, and has collapsed into something like a highly-stretched figure-eight. Following the passage of the wave crest (dark blue markers), the vertical component of the wave induced flow is negative and the vortex filaments are pushed down into the mean flow, which also accelerates them in the streamwise (positive x-direction). With the passage of the trough at the turbine, the vertical velocity changes from negative to positive, and the vortices are drawn upward into the slower moving wake, decelerating them in the

streamwise direction as compared to the mean flow. Even the vortex center positions for the steady case exhibit this effect, albeit to a lesser extent, as indicated by the gray markers. This can be seen more clearly referring back to Figure 22a.

As the cloud of associated vortex centers rotates, one can see that the vortices created during crest passage, shown dark blue and dark red in Figure 34, convect inward (positive z-direction) toward the slower moving wake and the output shaft above, whereas the vortices created during trough passage (shown light blue, green, and yellow in Figure 34) convect outward toward the wake boundary and the mean flow below. The figure-eight pattern, most prominent in the region of $1.3 < x/D < 1.8$, is created when the faster moving trough vortices overtake the slower moving mid-phase vortices (i.e. $\phi_w \approx \pi/2$ and $3\pi/2$) but the slower moving crest vortices do not.

Being familiar with the orbital path of a particle in a progressive wave, one might reasonably expect the vortex centers to follow the same path. However, it is important to note that the vortex center locations shown in Figure 34 don't represent the path of a single vortex filament, but the path of *successive* vortex filaments, thus adjacent symbols do not represent a time history of vortex center position. In fact, the points are entirely uncorrelated in time, the experiment spanning multiple runs over multiple days.

Perhaps the best way to consider the position of adjacent vortices shown in Figure 34 at any given instant in time is to compare clouds or bands of points of the same wave phase (i.e. color). For example, two adjacent vortex filaments represented by two symbols in the adjacent red-orange bands in the downstream region of $1.3 < x/D < 1.6$ were likely

separated by approximately the distance between the bands, which is comparable to the spacing shown in the steady case, indicated by the underlying gray symbols.

More generally, there is a noticeable gap in the downstream region of $1.3 < x/D < 1.6$, between the vortex center point clouds for what are likely the 1350° and 1530° [8^{th} and 9^{th} groups of] vortices, especially noticeable for vortex centers associated with the same wave phase (shown in the same color). The relative coherency in this region suggests that vortex interaction is not appreciably aided by wave action. In other words, the unsteady velocities imposed by the waves appear to change the streamwise spacing between adjacent helices as shown in Figure 32 and Figure 33, yet this does not appear to cause mutual induction to occur at an appreciably shorter distance downstream. This is in contrast to what might reasonably be inferred by the relative disorder of the blade-phase average velocity field (Figure 27b and Figure 28b). The strong helical structure shown in the steady case appears to remain intact, even in the presence of waves, at least at $x/D < 2.0$. As shown in previous studies [52, 53] and in agreement with the results shown in Chapter 4, the presence of a strong helical vortex structure precludes wake breakdown and re-energization.

That said, the vertical distribution of vortex center positions shown in Figure 34 suggests that vortex filaments, mainly restricted to the shear layer in steady flow, may be transported into the wake by the vertical wave velocity component at a higher rate as compared to the steady case, enhancing kinetic energy transport. In this way, the vortex filaments act as energy carriers, pushed into the wake to be devoured by turbulence.

Studying the spatial change in vortex parameters such as core radius, peak swirl velocity, and circulation in the unsteady case and comparing them to the steady case provides further insight as to how waves affect the wake. All data presented in this section is empirical as opposed to vortex model data that was calculated using the methods described in Section 4.4.

Figure 35a shows the spatial distribution of vortex center position with marker color corresponding to the vortex core radii, for the steady case as compared to the unsteady case (Figure 34b). The vortex core radii are normalized by the radius of the subregion used to calculate vortex parameters, r_0 (19 mm). As expected, Figure 35a shows the same trend as Figure 22c. The vortex core radius is essentially constant until the interaction region ($x/D \approx 1$) after which it decreases slightly.

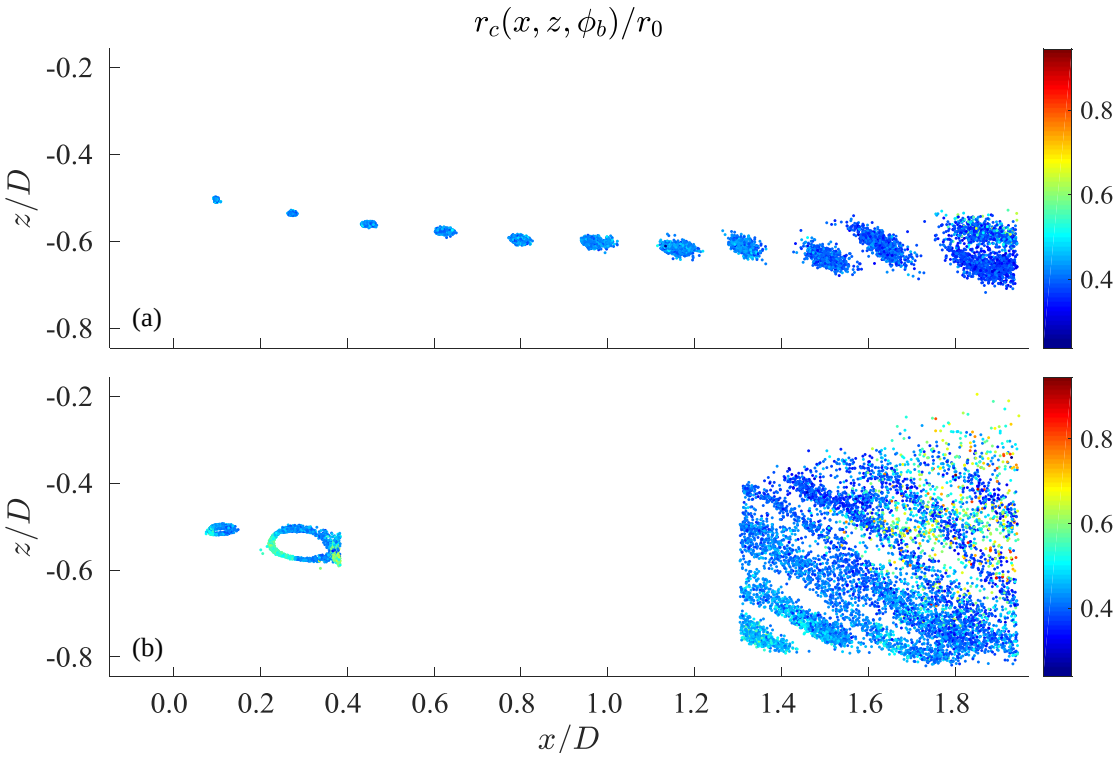

Figure 35: (a) The spatial distribution of vortex center positions with symbol color corresponding to the vortex core radius normalized by the subregion radius, r_0 for the steady and (b) unsteady cases. In both cases the mean flow is from left to right. In (b) the wave is wave 1 ($h/\lambda = 0.6$).

Shown in Figure 35b, there is a notable variation in vortex core radius with wave phase for the 90° [1st group of] and 270° [2nd group of] vortices. The largest radii, located on the upstream side of their respective orbital ellipse, correspond to the wave crest as shown in Figure 34, when the streamwise wave velocity is nearly at its peak[13] and the vertical velocity is approximately zero. The turbine blade produces increased lift under these conditions, which manifests as an increase in core radius. The same correlation seen in Figure 34 between the wave phase at which a tip vortex was created and its relative position in the wake can also be seen in Figure 35b. It is observed that the vortices appear to decrease in size by about 10% between the upstream and downstream regions.

In the region of $1.6 < x/D < 2.0$ there is a group of vortices (colored green to red) whose radii are 50-100% larger than those vortices in the region just adjacent. It is hypothesized that these vortices have interacted with an adjacent filament, are in the process of leapfrogging, and that this interaction has dissipated some of their energy to turbulence, dispersing the vortices spatially.

Many of the trends observed for the vortex core radius correlate to those observed for the peak swirl velocity, shown in Figure 36. Figure 36a depicts the spatial distribution of vortex centers with symbol color corresponding to peak swirl velocity, u_θ normalized by the free stream velocity, U_{tow}. Mirroring Figure 22c, the peak swirl velocity is shown to remain fairly constant for $x/D < 1.0$, decreasing slightly in the region of interaction. Coupled with a corresponding decrease in vortex core radius, this suggests angular momentum is lost as result of kinetic energy being transferred from the vortices to

[13] Recall that the wave phase is referenced to the streamwise location of the turbine, thus the vortices, located downstream of the turbine are slightly phase lagged.

turbulence. Indeed, there is a slight rise in the vortex center averaged turbulence kinetic energy, shown in in Figure 25 supporting this hypothesis.

Figure 36b depicts the spatial distribution of vortex center peak swirl velocity in the unsteady case. Similar to what was observed for the vortex core radii, in the upstream region, $0 < x/D < 0.4$, the peak swirl velocity is shown to vary with wave phase. Again, in the region were significant interaction and leapfrogging was observed for the steady case, $1.6 < x/D < 2.0$, a notable decrease in peak swirl velocity is observed, on the order of 50%. Likewise, it is hypothesized that this is the result of interaction between adjacent vortices.

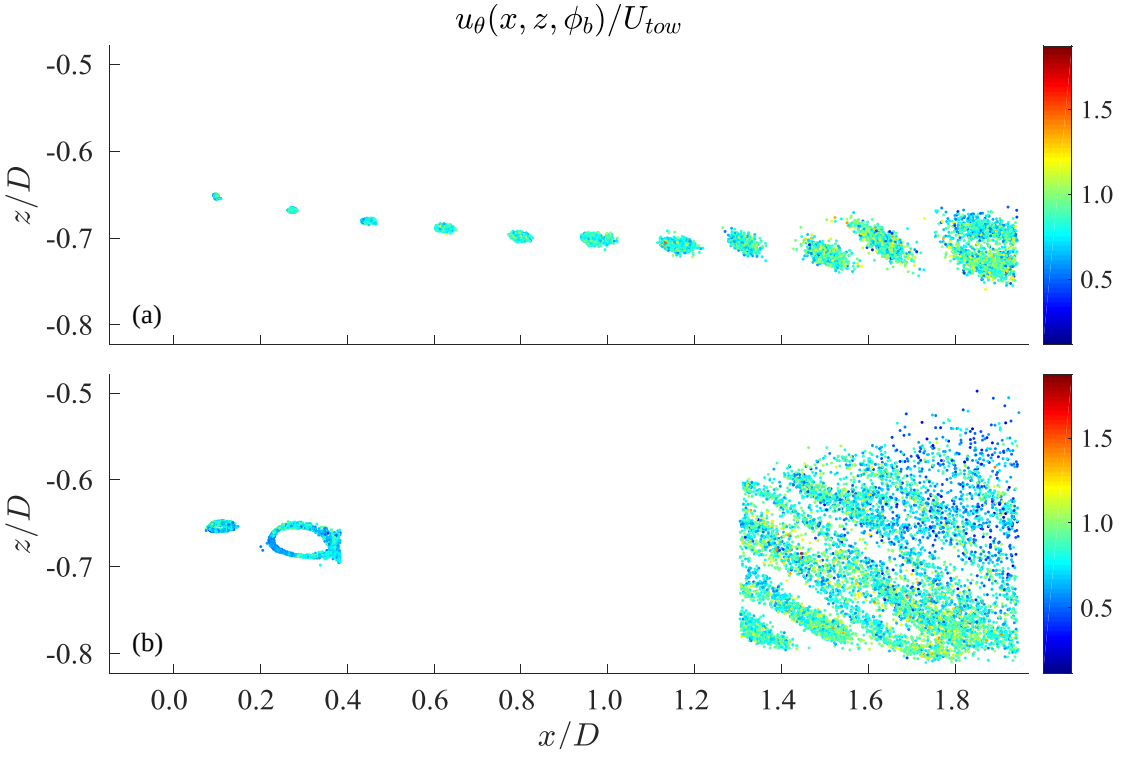

Figure 36: (a) The spatial distribution of vortex center positions with symbol color corresponding to the peak swirl velocity normalized by the turbine towing carriage speed for the steady and (b) unsteady cases. In both cases the mean flow is from left to right. In (b) the wave is wave 1 ($h/\lambda = 0.6$).

For further corroboration, the spatial distribution of vortex centers with marker color corresponding to the circulation, calculated using the line integral[14] and normalized by the towing carriage speed multiplied by the turbine diameter, is shown for the steady case in Figure 37a and the unsteady case in Figure 37b.

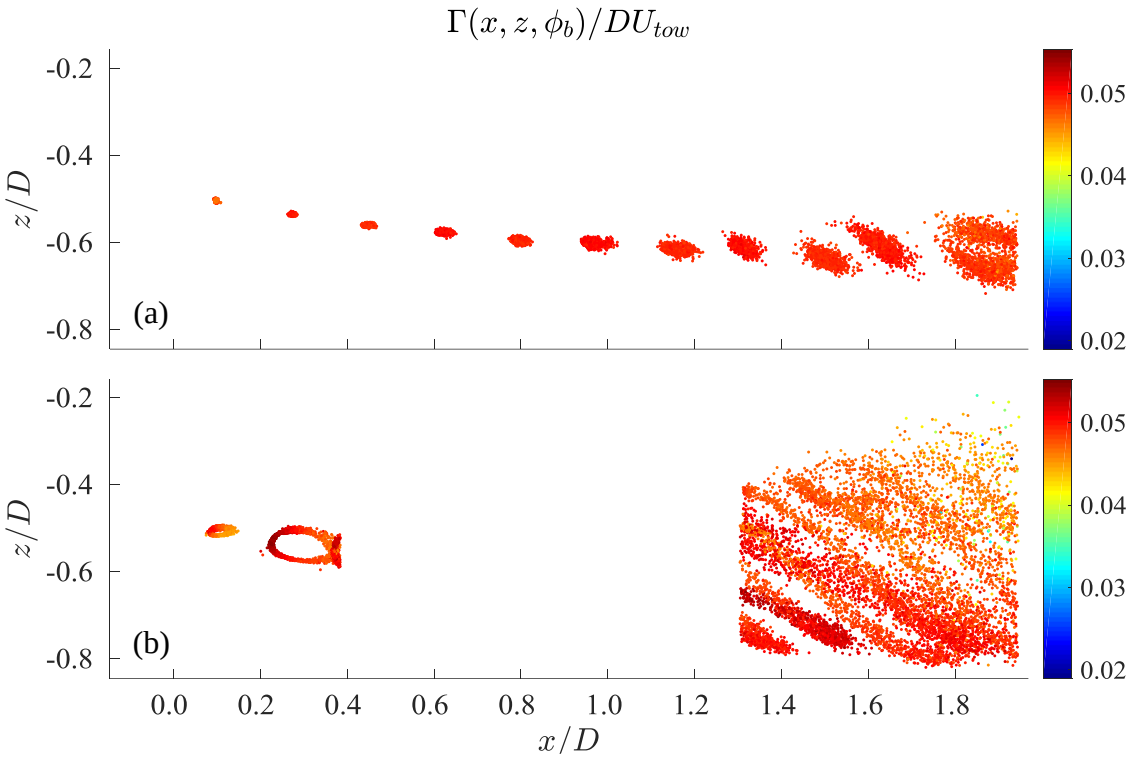

Figure 37: (a) The spatial distribution of vortex center positions with symbol color corresponding to the vortex circulation, calculated using the line integral method, normalized by the towing carriage speed multiplied by the turbine diameter. In both cases the mean flow is from left to right. In (b) the wave is wave 1 ($h/\lambda = 0.6$).

Again mirroring what is shown in Figure 22d, a slight, alternating variation in the circulation can be observed in the steady data (Figure 37a), likely due to a small mismatch in blade root pitch or a slight asymmetry in manufacturing which results in one blade producing vortices with slightly more circulation than the other. In the region of interaction, the circulation decreases slightly, corresponding with the trend shown in the

[14] The area integral was also calculated and is in very close agreement. For brevity, only the line integral results are shown.

empirical data in Figure 22d and the core radius and peak swirl velocity observations made above.

Like vortex core radius and swirl velocity, the circulation is shown to vary with wave phase (Figure 37b). In the upstream region, $0 < x/D < 0.4$, the circulation at $\phi_w = 0$ and 2π is observed to be approximately 20% higher than at the $\phi_w = 0$. This is due to the increased lift generated by the higher relative velocity, increasing bound circulation and thus increasing the circulation of vortices shed into the wake. The same convection patterns for vortices created at similar wave phase for core radius and peak swirl velocity are also observed for circulation, as is the decrease in circulation for vortices convected inward toward the wake core in the downstream region.

5.4.4 Vortex convection model

There are clear patterns in the vortex center distribution. In the upstream region the distribution is elliptical, stretching and rotating with streamwise distance from the turbine. In the downstream region, some coherency remains though it is difficult to say definitively how the patterns evolve as there is no data between $0.4 < x/D < 1.3$. Moreover, because adjacent points aren't correlated in time, it's difficult to determine how a vortex center, created at the turbine tip, subjected to a uniform stream, wake velocity field, and wave velocity field, gets from its origin at the turbine tip to where it was imaged. In an attempt to address these challenges, a simple model was developed to describe the trajectory of a given vortex center in space and time.

If one were to approximate the wake as being incompressible, inviscid, and irrotational, the wake could be modeled as a uniform stream, a source, and waves combined using linear superposition with the general form:

$$\Phi_{\text{combined}} = \Phi_{uniform\,stream} + \Phi_{source} + \Phi_{waves} \qquad (23)$$

where Φ is the velocity potential. Modeling the steady turbine wake as a uniform stream and source left a great deal to be desired in terms of representing the approximate velocity shear in a spatial sense that was recognizable as the turbine wake. In an effort to more faithfully represent the steady wake for direct comparison, a piece-wise velocity contour map was created instead of the uniform stream and sink as shown in Figure 38.

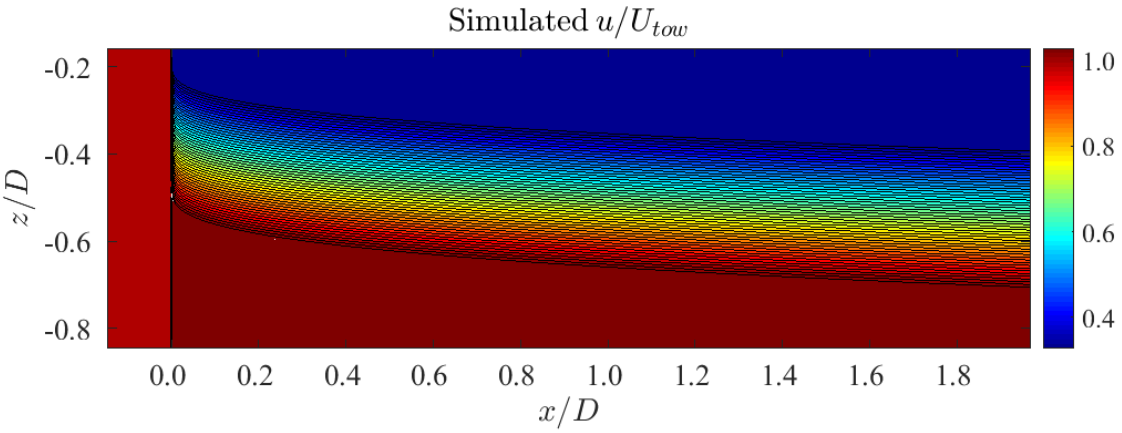

Figure 38: Simulated streamwise velocity, non-dimensionalized by the towing carriage speed, approximating a turbine wake at steady state including wake expansion. The simulated vertical velocity is not shown. Simulated flow is from left to right.

The region upstream of the turbine was not included in the simulation but is shown in Figure 38 set to a non-dimensional velocity (u_{wake}/U_{tow}) of 1. The velocity contours follow a 1/3 power-law model:

$$z = ax^{1/3} + b \qquad (24)$$

where x and z are the spatial coordinates and a and b are coefficients fit to empirical velocity contours. The upper-most contour, closest to the turbine output shaft, is the maximum velocity deficit contour for the steady case, shown in Figure 27a. The region above this contour was set to the minimum velocity in the field of investigation

($u_{wake}/U_{tow} \approx 0.33$). The bottom-most contour is the wake width for the steady case, also shown in Figure 27a. The region below the wake width was set to the blockage-induced maximum velocity of ($u_{wake}/U_{tow} \approx 1.02$). The contour lines representing the shear layer were created at intervals between the maximum velocity deficit contour and the wake width (i.e. linearly interpolating the coefficients a and b given in Equation 24 between the two contours). The velocity at each x, z position was then interpolated to create an evenly-spaced array of velocity values, $u_{wake}(x, z)$ and $w_{wake}(x, z)$. The simulated wake was assumed to be steady in time. The vertical velocity of the wake was assumed to vary only in the x-direction (i.e. $dw_{wake}/dz = 0$), based on observations of the downstream region in Figure 29b. A vertical velocity array was made by determining the vertical velocity along the mean vortex center contour, δ_V and fitting those results (w_{wake} vs. x) with an exponential expression of the form $w_{wave} = ax^b + c$ to simulate the exponential decay of the vertical velocity with downstream distance.

A time vector of n elements was defined from 0 to t seconds in equal increments of Δt. At each instant in time, t_i and given some initial wave phase angle, $\phi_{w,0}$ the wave phase angle at the turbine, $\phi_w(t_i)$ was calculated. From $\phi_w(t_i)$, the wave velocity components, $u_{wave}(x, z, \phi_w(t_i))$ and $w_{wave}(x, z, \phi_w(t_i))$ were calculated. The wave velocity components were then added to the steady wake velocity components, $u_{wake}(x, z)$ and $w_{wake}(x, z)$. Thus the combined velocity field (i.e. wake plus waves), for both velocity components $u_{comb}(x, z, t_i)$ and $w_{comb}(x, z, t_i)$ were calculated at each moment in time.

The vortex centers were approximated as massless particles, deposited every m time steps, where $m = 1/(\Omega\, \Delta t)$. Currently, the model does not capture the variation of

turbine rotation speed as a function of wave phase (i.e. the turbine "rotates" at constant speed). The position of each deposited vortex center (i.e. particle) was taken from the 90° [1st group of] vortices, including the random distribution associated with aperiodicity. A discretized, forward-difference time-step model:

$$x_c(t_{i+1}) = u_{comb}\big(x_c(t_i), z_c(t_i)\big)\,\Delta t + x_c(t_i) \tag{25}$$

$$z_c(t_{i+1}) = w_{comb}\big(x_c(t_i), z_c(t_i)\big)\,\Delta t + z_c(t_i) \tag{26}$$

was used to simulate movement of the vortex centers through the wake at any instant in time. The position of each particle in the field of investigation was saved at every simulated blade passage (i.e. every m time steps), simulating PIV image capture. The model results were superimposed on the blade phase averaged streamwise velocity data for the unsteady case and are included in

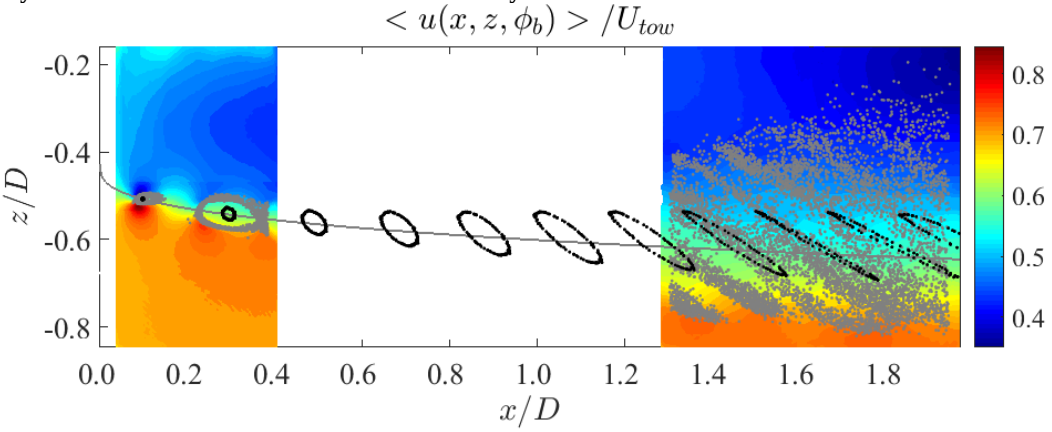

Figure 39.

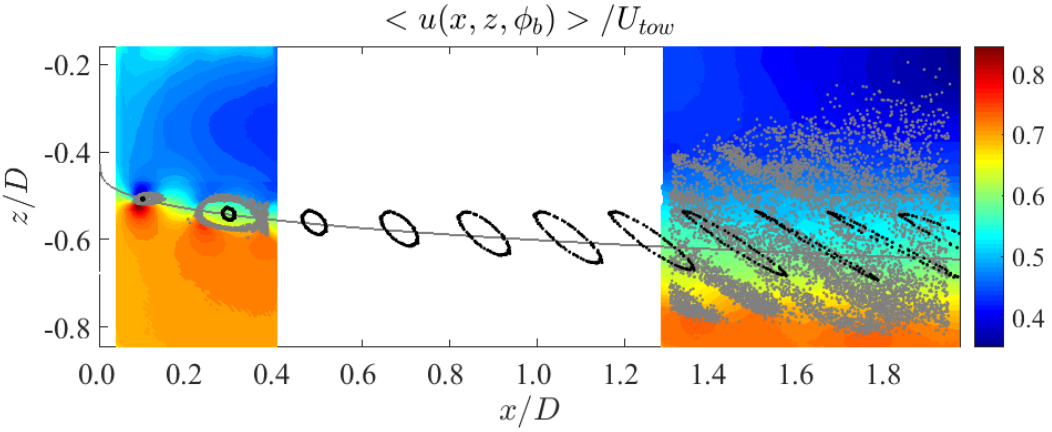

Figure 39: Blade phase averaged streamwise velocity for the unsteady case, overlaid with vortex convection model results (black symbols). Vortex center locations are shown in gray symbols for the unsteady case. The solid gray line indicates the mean vortex center contour for the steady case. Flow is from left to right.

The vortex center convection model, as described, is a highly simplified representation of the complex unsteady wake. Yet for all its simplifications it does appear to demonstrate several important characteristics of the experimental data in the unsteady case. It approximates the elliptical pattern created by the vortices as they are inserted at locations tightly but randomly distributed around the first vortex position. It demonstrates the effect of the shear layer, stretching and rotating the elliptical pattern clockwise as some vortices are pushed outward (in the negative z-direction) and accelerated by the mean flow, while others are pushed inward (in the positive z-direction) and decelerated in the wake core. It captures the spacing between adjacent vortex center point clouds and even reasonably captures the angle of rotation in the downstream region. It agrees well with the general shape of the expanding wake, and shows how the upstream and downstream sides of the elliptical pattern collapse into a single line in the downstream region.

It is also instructive to examine the discrepancies between the model and the underlying empirical data, specifically between the predicted and observed vortex center positions for the unsteady case. To begin, it should be pointed out that the steady wake velocitity field was only intended to be a qualitative representation of the empirical data. A greater effort could be made to represent the streamwise component of the steady wake velocity field more accurately, perhaps with a non-linear least-squares fit routine, but this will always be problematic because of the presence and influence of the vortices. Likewise, it was assumed that the velocity was invariant in the vertical direction (i.e. $dw_{wake}/dz =$

0). A more accurate rendering of the vertical velocity could increase the accuracy of the model, particularly the vertical extent of the vortex center distribution. The simulated wave velocity components are likely accurate to a first approximation, though it was assumed that the two components – the wake and the waves – could be superimposed, neglecting any non-linear effects. It would be difficult to capture these effects in a simple model, but their absence may at least partly explain the mismatch between the model and the data.

In the upstream region ($0.2 < x/D < 0.4$), there is a significant discrepancy between the circular orbital path of the model and the highly-elliptical pattern described in the data. This is likely due to several factors. First, the vortex centers were modeled at massless particles in an inviscid and irrotational flow field. It is unclear what effect these phenomena have on vortex filament location, but it is hypothesized that including vortex circulation may improve the accuracy of vortex center position predictions. Second, as mentioned in the description, the turbine rotation speed is modeled as steady in time, thus the tip vortex spacing is initially equal. The highly elliptical orbital pattern observed in the upstream region ($0 < x/D < 0.4$) is likely due to the change in helical pitch with wave phase. This can be seen in Figure 34 with the vortex centers associated with the wave peak clustered at the upstream end of the pattern and those associated with the trough clustered at the downstream end of the pattern. It is hypothesized that including variation of the turbine rotation speed in the model (i.e. "inserting" vortices at unequal intervals according to wave phase) would better capture the elliptical shape of the vortex center pattern. Including this consideration in the model may also better capture the "lazy eight" pattern show in the downstream region where the vortex centers associated with the wave peak pass

downstream of those associated with the trough near the mean flow but do not further in toward the wake core.

Qualitatively, if the model can be assumed to reasonably represent wake evolution, at least in terms of characteristic length scales, it was hypothesized that a parametric study might be telling in terms of which parameters have the most impact on those length scales. The datum case, shown in

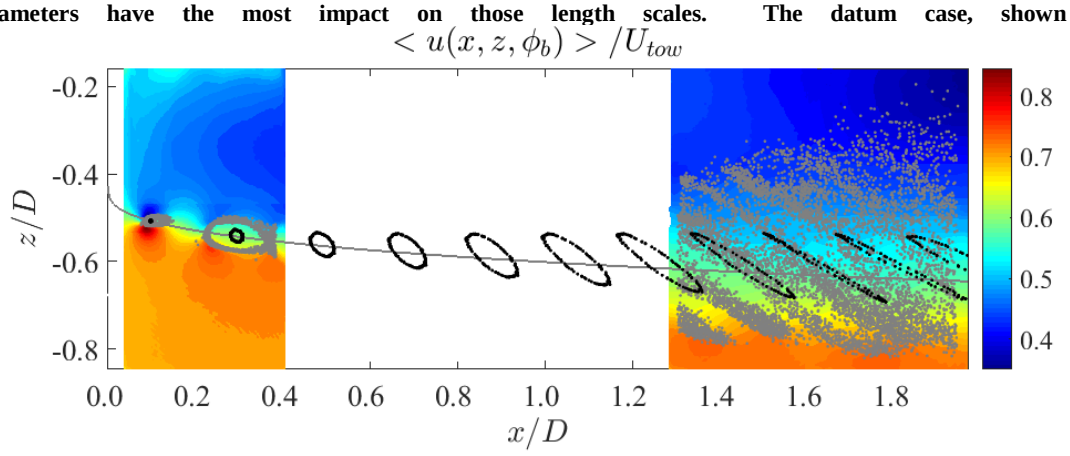

Figure 39, included wake parameters, as described above, and a wave modeled after the one used in the experiment (H = 1.8 m, T = 2.3 s). The parameters included in the study were the towing carriage speed, U_{tow}, the spread of the contour lines used to create the streamwise velocity array, the vertical velocity component of the wake, w_{wake}, and the vertical velocity component of the wave, w_{wave} (i.e. the wave amplitude). Each parameter

was increased systematically by 25% while the other parameters were held constant[15]. The results of the parametric study are depicted graphically in Figure 40.

Each of the parameters is compared to the base case and the dashed gray line indicates the particle path in the steady (no wave) case. The base case is symmetric around the mean vortex center contour. Comparing first the case of increasing, w_{wake} (shown

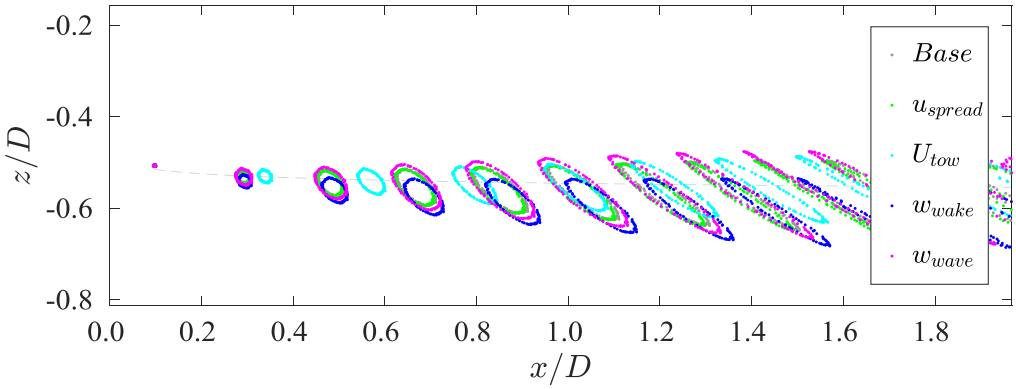

Figure 40: Model results for the parametric study. Gray markers represent the base case, green markers represent the effect of increased wake spread, light blue markers represent the effect of increased towing carriage speed, blue markers represent the effect of increasing the vertical velocity component of the wake, and purple markers represent the effect of increasing wave amplitude. The dashed gray line represents the mean vortex center contour for the steady case.

with blue markers) it is observed that the only associated effect is to shift the vortex centers in the negative z-direction. The vertical extent of the vortex center cloud for each wake age is the same as for the base case, indicating that w_{wake} influences wake width, δ but not the extent of the shear layer. Next, comparing the vertical component of the wave velocity, w_{wave} (shown with purple markers) the vertical extent is increased, by 6% compared to the base case, centered around the steady case vortex center path, thus the shear layer thickness is dependent on the significant wave height (i.e. w_{wave}), but not the mean vortex center contour. The effect of increasing the uniform stream speed (shown in

[15] For the vertical component of the wake velocity, this meant multiplying the coefficient a by a constant such that the vertical velocity component of the wake was 25% higher as compared to the base case. The spread of the contour lines was increased similarly, by increasing the coefficient a by 25%, which resulted in a decrease in velocity shear.

light blue markers) was only to move the orbital paths further in the streamwise direction over the same time period, as compared to the base case. Neither the wake width nor the vertical extent of the shear layer was not affected. Finally, changing the streamwise velocity gradient of the wake, in both the horizontal ($\partial u/\partial x$) and vertical ($\partial u/\partial z$) directions (shown in green markers) did not affect either length scales appreciably. Thus, the results of the parametric study suggest that it is the wake vertical velocity, w_{wake} that has the most influence in defining the wake width, δ and the wave vertical velocity, w_{wave} that most influence in defining the height of the shear layer.

As previously discussed, the wake boundary is typically described by a 1/3 power law fit. This can also be non-dimensionalized by the turbine diameter, but will be left in dimensional form for the following discussion.

Starting from the idealized model paradigm in which the wake in the no-wave case is essentially steady in time, one could imagine that the unsteady wake could be modeled by superimposing a wave-induced shear layer on mean vortex contour in order to arrive at something a kin to the model results shown in

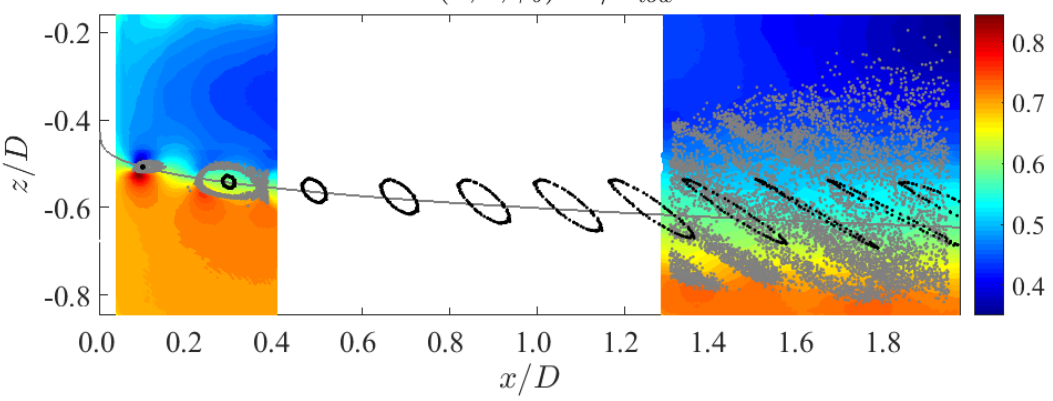

Figure 39. Assuming that the vertical extent of the vortex center displacement is indeed most influenced by the wave vertical velocity, a new length scale, the shear layer half width, $\delta_{SL,1/2}$ is proposed. Symmetric about the mean vortex center contour, the shear layer half width is proposed as the integral of the wave vertical velocity over time:

$$\delta_{\mathrm{SL},1/2} = \int_0^t w_{wave}\, dt \qquad (27)$$

In order to map the time dependent results to the spatial representation shown in $< u(x, z, \phi_b) > /U_{tow}$

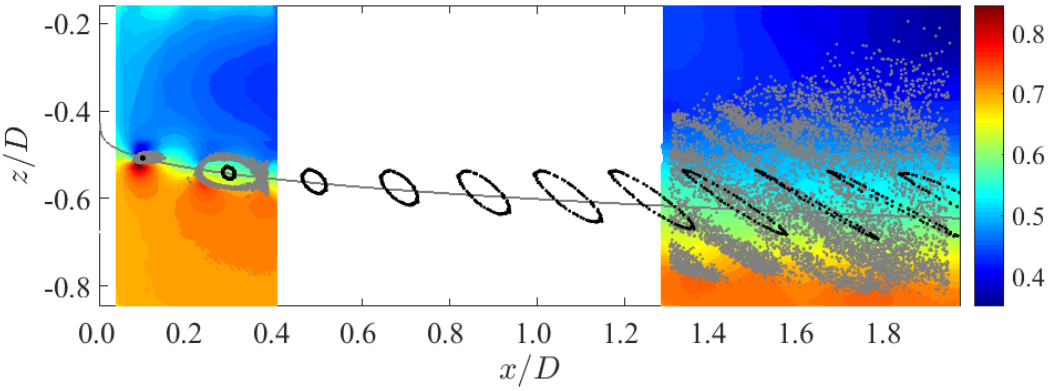

Figure 39, a detailed understanding of the velocity field (i.e. u and w as a function of x, z, and t) is needed, thus negating the need for a model. Instead, if it is assumed that the horizontal components of the wake and wave have negligible effect on the vertical extent of the shear layer, as indicated by the parametric study, then time could be approximated by $dt = dx/U_{tow}$. This would provide the opportunity to transform Equation 27 from a function of time to a function of downstream distance, x:

$$\delta_{SL,1/2} = \frac{1}{U_{tow}} \int_0^x w_{wave}\, dx \tag{28}$$

Inserting the expression for the wave vertical velocity (Equation 12) yields:

$$\delta_{SL,1/2} = \frac{1}{U_{tow}} \int_0^x \frac{H}{2} \sigma \frac{\sinh k(h+z)}{\sinh kh} \sin(kx - \phi_w)\, dx \tag{29}$$

The majority of the integrand is simply the maximum vertical wave velocity. It is extracted as a constant and the remaining function integrated and simplified yielding:

$$\delta_{SL,1/2} = \frac{w_{wave,max}}{U_{tow}} \left(\frac{\cos(kx - \phi_w)}{k} + C \right) \tag{30}$$

where ϕ_w is the wave phase at which the maximum shear layer thickness occurs, and C is a constant of integration with units of length. In this case, the constant of integration was taken to be half the vertical displacement between wake width and the wake half width for the steady case, as depicted in Figure 27a. Under these conditions, Equation 30 yields the result shown in Figure 41.

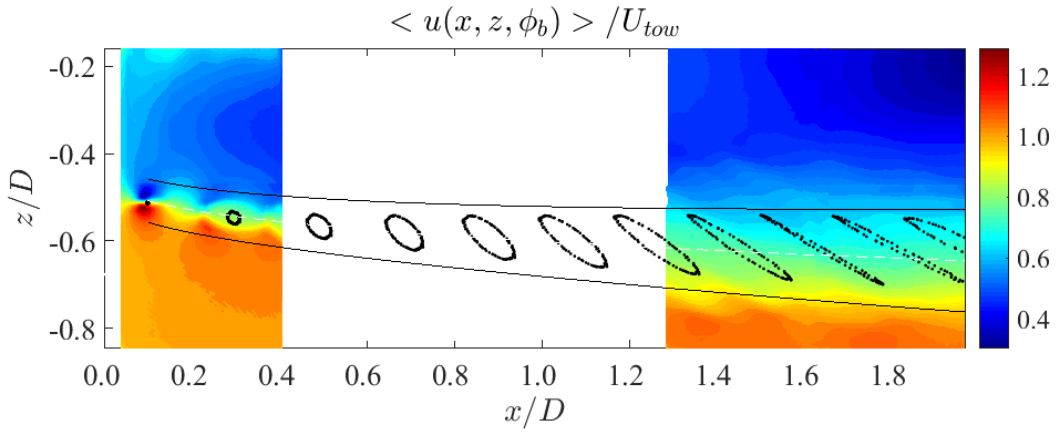

Figure 41: Turbine blade phase averaged velocity with models overlaid. The black markers represent the results of the "potential flow" model. The gray dashed line represents the mean vortex center contour for the steady case. The black solid lines represent the shear layer half width. Mean flow is from left to right.

The shear layer boundary as defined by the mean vortex center contour and the shear layer half width appears to bound the shear layer reasonably well, including the 90° (1st) vortex in the upstream region, and follows the wake boundary, as previously defined, in the downstream region. The fit of the upper boundary is qualitatively comparable to the wake half width, $\delta_{1/2}$ as applied to the steady case (Figure 27a). Agreement with the vortex center convection model is fair but not expected considering the two results were achieved by different if related methods.

5.5 Conclusions

A 1/25th scale model axial-flow hydrokinetic turbine, based on the U.S. Department of Energy's Reference Model 1 tidal current turbine, was tested in the large towing tank facility at the U.S. Naval Academy to assess the impact of waves on near-wake characteristics. To the author's knowledge, there are no wake surveys in the presence of waves mentioned in the literature at any scale or resolution. The model wave, having a relative depth of h/λ = 0.6, is intended to represent oceanic swell encountered of the U.S. east coast.

Blade phase averaged results were compared for the steady (no wave) and unsteady (wave) cases. Wake stability in terms of the size and position of coherent structures such as the tip vortex helix, high in the steady case, was significantly reduced in the unsteady case. Length scales traditionally used to describe the canonical axisymmetric wake, were found to describe the steady wake well. These same length scales could not, however, be applied to the unsteady case due to a considerable decrease in coherency.

Blade and wave phase averaged results were included for the streamwise velocity component, showing a high degree of coherency, in contrast to blade phase only results. The wake boundary, was shown to undulate with wave passage, and vortex center positions were shown to move in a periodic motion with the unsteady wave velocity. Vertical travel of the wake boundary was shown to be on the same order of magnitude as the elliptical path of a particle under the same conditions.

Vortex center positions were presented as a function of wave phase and were also used to illustrate how vortex parameters such as core radius and circulation, evolved in the

near wake. Aspects of the unsteady wake such as adjacent vortex spacing are comparable to the steady case, however, it appears that the vertical wave velocity is enhancing the vertical convection of vortices into the wake core, potentially acting as energy carriers, accelerating wake breakup and re-energization.

A vortex center convection model was created to help interpret the results described above, agreeing reasonably well with experimental observations. A parametric study using the model was conducted and suggests that the primary parameter affecting the wake boundary length is the vertical component of wake expansion and the primary parameter affecting the unsteady shear layer development is the wave vertical velocity. A new length scale was proposed to describe the unsteady shear layer and was shown to agree well with empirical observations, though additional studies will be needed to confirm and refine the description.

6 Conclusions, contributions, and future work

6.1 Conclusions

A near-scale independent axial-flow marine hydrokinetic turbine based on the U.S. Department of Energy's Reference Model 1 tidal current turbine was tested in the large towing tank facility at the U.S. Naval Academy in steady (no-wave) conditions and unsteady (wave) conditions. For the steady case, baseline performance parameters – C_P and C_T – were calculated as a function of TSR and found to be in good agreement with previous studies. A BEM model was developed and was also found to be in good agreement with experimental observations. Tests were performed to determine the minimum operating depth below which turbine performance would not be affected and a detailed uncertainty analysis was conducted.

Tests were also conducted for each permutation of two wave forms and two turbine operating depths. Model waves were selected to represent oceanic swell potentially encountered off the U.S. east coast. Wave steepness, defined as the wave height to the wavelength, was held constant for both waves, while the relative depth, defined as the water column depth to the wavelength, was varied from near-intermediate ($h/\lambda = 0.6$) to deep ($h/\lambda = 1.2$). Operating depth was varied from $L/D = 1.3$ to 2.25. In the presence of waves, the time average value for the performance parameters, taken over the entire run, was found to be equivalent to the no-wave case. This time average value was not affected by the relative depth of the wave or the operating depth of the turbine for the waves and depths tested. The instantaneous values, however, were shown to vary significantly with wave phase. The range of performance parameter response was inversely proportional to the relative depth of the wave and the operating depth. With regard to the operating depth,

the result was unsurprising considering wave influence increases with proximity to the free surface. With regard to the effect of wave relative depth, it is unclear if the difference in the magnitude of the response was related to the wave relative depth or the difference in the wave energy per unit width, which was not held constant and was nearly eight times higher for one wave form compared to the other. Regardless, given seemingly disproportionate response of power and thrust variations to comparatively small waves, it is advocated that wave characterization should be included in the site installation survey for a grid-power scale turbines as waves are likely to have significant impact on power quality and structural loading.

A survey of the near wake (<2D) was conducted under steady conditions. The field of investigation extended from approximately 0.1D upstream of the turbine to 2.0D downstream, and radially outward to a distance of 0.85D. High resolution flow field observations were made using 2-D planar PIV enclosed in an in-house designed and manufactured, towed submersible housing system. Phase-averaged flow field results supported many previous observations made for smaller-scale models. These included the slowing of the flow just upstream of the turbine to 75% of the free stream velocity due to the increase in static pressure, wake expansion well-described by the 1/3 power of the streamwise distance, and the velocity deficit reaching a maximum of 2/3 the free stream velocity. Turbine blade root vortices were also observed but to a very limited extent given the limits of the field of investigation. Tip vortex characterization techniques developed for helicopter rotor research were applied to calculate relevant vortex parameters. Spacing of adjacent vortex filaments was found to be relatively constant as was vortex core radius to a streamwise distance of approximately 1D. Further downstream vortex interaction and

mutual induction were observed followed by the first 90° rotation of leapfrogging, the phenomenon that likely initiates wake re-energization. Phase-averaged turbulence statistics were calculated for the entire field of investigation and compared to individually averaged results in the active region immediately surrounding each vortex. Individually averaged turbulence statistics were lower by as much as an order of magnitude and were shown not to follow the same trends as the phase-averaged results. This demonstrates that vortex center aperiodicity can have a profound effect on the interpretation of results and should be considered in their evaluation.

A companion study was conducted to assess the impact of waves on near-wake characteristics. To the author's knowledge, there are no wake surveys in the presence of waves mentioned in the literature at any scale or resolution. Blade phase averaged velocities were presented for the steady and unsteady cases. Wake stability in terms of the size and position of coherent structures such as the tip vortex helix, high in the steady case, was significantly reduced in the unsteady case. Length scales traditionally used to describe the canonical axisymmetric wake were found to describe the steady wake well. These same length scales could not, however, be applied to the unsteady case due to changes in the unsteady velocity profile, upon which the length scales are based.

Blade and wave phase averaged results were included for the streamwise velocity component, showing a high degree of coherency, in contrast to blade phase only results. The wake boundary, was shown to undulate with wave passage, and vortex center positions were shown to move in a periodic motion with the unsteady wave velocity. Vertical travel of the wake boundary was shown to be on the same order of magnitude as the elliptical path of a particle under the same conditions.

Vortex center positions were presented as a function of wave phase and were also used to illustrate how vortex parameters such as core radius and circulation, evolved in the near wake. Aspects of the unsteady wake such as adjacent vortex spacing are comparable to the steady case, however, it appears that the vertical wave velocity is enhancing the vertical convection of vortices into the wake core, potentially acting as energy carriers to accelerate wake breakup and re-energization.

A vortex center convection model was created to aid in interpretation of the results described above, agreeing reasonably well with experimental observations. A parametric study using the model was conducted and suggests that the primary parameter affecting the wake width is the vertical component of wake expansion and the primary parameter affecting the vertical extent of vortex center displacement is the wave vertical velocity. A new length scale, the shear layer half width, was proposed to describe the width of the unsteady shear layer and was shown to agree well with empirical observations.

6.2 Contributions

Results are presented for a large-scale test of an axial-flow marine hydrokinetic turbine conducted under laboratory conditions. The associated data set, including performance data as well as PIV observations, is arguably the most accurate non-proprietary data set available with which to predict the performance and near-wake characteristics of a full-scale turbine. Scale dependent observations have lower C_P and C_T values for a given tip speed ratio than those of a full-scale prototype. Especially in regions of high shear such as the near wake, Reynolds number dependence can manifest as artificially high turbulence statistics [27]. For the few studies conducted on turbines of comparable scale the facilities are not commensurately large to preclude significant blockage. In contrast, blockage tends to artificially increase turbine performance, increasing turbine inflow velocity above what it would be in the free stream case. Blockage correction methodologies can be applied to performance parameters, but as in the case of scale dependence, one cannot readily discern the between turbine performance and blockage effects with regard to velocity field observations.

The related studies Luznik et al. [38] and Lust et al. [26] were the first to apply the Hilbert transform to present wave phase averaged performance data for marine hydrokinetic turbines, illuminating the significant deviation of performance parameters from their time average values.

The use of a towing tank PIV system is rare due to its considerable complexity, and if purchased from one only a few available vendors, expense. To the author's knowledge no other studies have employed a PIV system in a towing tank to take such high-resolution measurements at such a large scale. Many previous surveys were conducted with LDV or

ADV [29, 49, 48, 51] and are, as a consequence, lower resolution. As indicated in Figure 19, nearly 1,000 realizations were required to achieve statistical convergence. Few studies state the number of realizations included in their phase averages, and of those that do, only a few include enough realizations to ensure convergence [45, 56], thus it is difficult to discern the uncertainty of the associated measurements. This is also one of few surveys which focuses on the near wake [46, 45, 47, 53, 56] and the features and characteristics thereof, and only one of two rigorous studies focusing specifically on marine hydrokinetic turbines [45]. Clearly there is a dearth of such studies in the marine hydrokinetic turbine literature.

This is the first study to apply tip vortex analysis techniques developed for helicopter rotor analysis to the study of marine hydrokinetic turbines. Aperiodicity was characterized and was shown in relation to vortex filament interaction, confirming previous observations regarding the onset of wake instability. Vortex parameters including core radius, peak swirl velocity, and circulation, were used for the first time in the marine hydrokinetic turbine literature to illustrate the evolution of the near-wake. The use of a vortex center averaging scheme was used to show that Reynolds stresses as typically presented in the literature do not represent turbulence in the classical sense but instead aperiodicity, giving a false sense of the turbulence transport in the wake boundary region.

To the author's knowledge, there are no other wake surveys for turbines operating in the presence of waves in the literature. Thus, this is the first presentation of all such results including blade phase averaged, and blade and wave phase averaged results. As with steady survey results, this is the first time vortex characterization has been applied to describe the evolution of the wake of a marine hydrokinetic turbine in terms of the spatial

gradient of vortex parameters. Length scales developed to describe the canonical axisymmetric wake were applied to the wake of a marine hydrokinetic turbine with good agreement and an additional parameter was proposed to describe the shear layer expansion that is unique to unsteady turbine wakes.

6.3 Future work

A great deal of work remains to be done in the field of marine hydrokinetic turbines, some of which is unique to this particular field and some of which could potentially be applied to the study of wind turbines and helicopter rotor aerodynamics.

It is hypothesized that there is a relationship between the calculated performance parameters, C_P and/or C_T, and the wake boundary as a function of downstream distance. The 1/3 power-law relationship has been documented in the literature (e.g. [45]) but the characteristic constants are empirically derived. Given that wake expansion is driven, in part, by the change in linear momentum, and that that change is directly related to the performance parameters, it is surmised that there is a non-dimensional relationship between the measured power and thrust and the characteristic length scales of the wake in the steady case:

$$\delta = \varphi(x, C_P \; or \; C_T) \tag{31}$$

This would be another useful tool for estimating the pertinent length scales in the near-wake region.

In the present experiment the wave steepness was held constant and the relative depth was changed. The energy per unit width of the waves was therefore also different,

therefore the effect of one versus the other cannot be discerned. A separate test was conducted with the intent of constraining the energy per unit width and wave relative depth while allowing wave steepness to change. However, brake binding and wave maker limitations precluded the completion of this test. In the future, if an alternate means of controlling the turbine shaft speed such as a motor could be employed, multiple permutations could be tested to determine the specific impact of these parameters.

Further testing could be conducted with the present experimental set up, focusing on a few key fields of view in order to acquire time-resolved flow field observations. Such measurements would allow for the separation of the time-averaged velocity from the periodic velocity associated with turbine rotation. This would also provide the opportunity to address the fluctuating velocity and the fluctuations associated with aperiodicity separately (Equation 21), potentially providing more accurate observations of Reynolds stress terms.

With the experience of designing a 2D PIV system, a new stereo PIV system could be constructed which would enable the calculation of momentum and energy transport terms to further illuminate the effect of aperiodicity on turbulence statistics by enabling the calculation of transport terms. There is also the potential of modifying the towing carriage set-up such that observations should be made further downstream ($2.0 < x/D < 3.0$) to capture, at high resolution, the next stage of vortex interaction.

Based on the results of the study described above in which wave parameters are varied systematically to determine the specific influence of each, an additional wave form could be selected and an associated PIV wake survey conducted. The wake characteristics

of the two unsteady cases could be compared to provide a second perspective on the influence of waves. A second survey would also provide the opportunity to confirm observations regarding length scales proposed in the present study. The ability to measure all three components of velocity would provide the opportunity to calculate turbulent transport terms to examine more closely the role of vortex convection in wake re-energization.

7 References

[1] W. A. Hermann, "Quantifying global exergy resources," *Energy*, vol. 31, pp. 1685-1702, 2006.

[2] Z. Zhou, M. Benbouzid, J. Charpentier, F. Scuiller and T. Tang, "Developments in Large Marine Current Turbine Technologies - A Review," *Renewable and Sustainable Energy Reviews*, vol. 71, pp. 852-858, 2017.

[3] H. Todd, "DOE Reference Model Project Fact Sheet," 2015. [Online]. Available: http://energy.sandia.gov/energy/renewable-energy/water-power/technology-development/reference-model-project-rmp/. [Accessed 26 May 2017].

[4] G. S. Bir, M. J. Lawson and Y. Li, "Structural design of a horizontal-axis tidal current turbine composite blade," in *ASME 30th International Conference on Ocean, Offshore, and Arctic Engineering*, Rotterdam, The Netherlands, 2011.

[5] T. Burton, N. Jenkins, D. Sharpe and E. Bossanyi, Wind Energy Handbook, Second Edition, West Sussex: Wiley, 2011, pp. 39-41.

[6] A. Betz, Introduction to the Theory of Flow Machines, Elsevier, 2014.

[7] H. Glauert, The analysis of experimental results in the windmill brake and vortex ring states of an airscrew., HM Stationary Office, 1926.

[8] H. Glauert, "Windmills and fans," in *Aerodynamic theory*, Vols. 4, Division L, W. F. Durand, Ed., Berlin, Julius Springer, 1935, pp. 169-360.

[9] R. E. Wilson and P. B. Lissaman, "Applied Aerodynamics of Wind Power Machines," Corvalis, 1974.

[10] J. F. Manwell, J. G. McGowan and A. L. Rogers, Wind Energy Explained: Theory, Design, and Application, John Wiley & Sons, 2010.

[11] J. N. Goundar, M. R. Ahmed and Y.-H. Lee, "Numerical and Experimental Studies on Hydrofoils for Marine Current Turbines," *Renewable Energy*, vol. 42, pp. 173-179, June 2012.

[12] M. Drela, "XFOIL: An Analysis and Design System for Low Reynolds Number Airfoils," in *Lecture Notes in Engineering*, vol. 54, T. J. Mueller, Ed., Berlin, Springer, 1989.

[13] W. Koh and E. Ng, "Effects of Reynolds Number and Different Tip Loss Models on the Accuracy of BEM Applied to Tidal Turbines as Compared To Experiments," *Ocean Engineering,* vol. 111, pp. 104-115, 2016.

[14] J. M. Walker, K. A. Flack, E. E. Lust, M. P. Schultz and L. Luznik, "Experimental and Numerical Studies of Blade Roughness and Fouling on Marine Current Turbine Performance," *Renewable Energy,* vol. 66, pp. 257-267, 2014.

[15] J. Whelan, J. Graham and J. Peiro, "A Free-Surface and Blockage Correction for Tidal Turbines," *Journal of Fluid Mechanics,* vol. 624, pp. 281-291, 2009.

[16] Whelan, J. Whelan, M. Thompson, J. Graham and J. Peiro, "Modeling of Free Surface Proximity and Wave Induced Velocities Around a Horizontal Axis Tidal Stream Turbine," in *EWTEC,* Porto, 2007.

[17] C. Faudot and O. G. Dahlhaug, "Prediction of Wave Loads on Tidal Turbine Blades," *Energy Procedia,* vol. 20, pp. 116-133, 2012.

[18] P. L. Frankel, "Power From Marine Currents," *Proceedings of the Institution of Mechanical Engineers, Part A: Journal of Power and Energy,* vol. 216, pp. 1-15, 2002.

[19] A. B. S. Bahaj and L. Myers, "Fundamentals Applicable to the Utilization ofMarine Current Turbines for Energy Production," *Renewable Energy,* vol. 28, pp. 2205-2211, 2003.

[20] L. Myers and A. B. S. Bahaj, "Power Output Performance Characteristics of a Horizontal Axis Marine Current Turbine," *Renewable Energy,* vol. 31, pp. 197-208, 2006.

[21] A. S. Bahaj, A. F. Molland, J. R. Chaplin and W. M. J. Batten, "Power and Thrust Measurements of Marine Current Turbines Under Various Hydrodynamic Flow Conditions," *Renewable Energy,* vol. 32, no. 3, pp. 407-426, 2007.

[22] D. P. Coiro, U. Maisto, F. Scherillo, S. Melone and F. Grasso, "Horizontal Axis Tidal Current Turbine: Numerical and Experimental Investigations.," in *OWEMES*, Civitavecchia, 2006.

[23] W. Batten, A. Bahaj, A. Molland and J. Chaplin, "Hydrodynamics of Marine Current Turbines," *Renewable Energy,* vol. 31, pp. 249-256, 2006.

[24] W. Batten, A. S. Bahaj, A. F. Molland and J. R. Chaplin, "The Prediction of the Hydrodynamic Performance of Marine Current Turbines," *Renewable Energy,* vol. 33, no. 5, pp. 1085-1096, 2008.

[25] A. B. S. Bahaj, W. Batten and G. McCann, "Experimental Verifications of Numerical Predictions for the Hydrodynamic Performance of Horizontal Axis Marine Current Turbines," *Renewable Energy,* vol. 32, no. 15, pp. 2479-2490, 2007.

[26] E. E. Lust, L. Luznik, K. A. Flack, J. M. Walker and M. C. Van Benthem, "The Influence of Surface Gravity Waves on Marine Current Turbine Performance.," *International Journal of Marine Energy,* vol. 3, no. 4, pp. 27-40, 2013.

[27] L. P. Chamorro, R. Arndt and F. Sotiropoulos, "Reynolds Number Dependence of Turbulence Statistics in the Wake of Wind Turbines," *Wind Energy,* vol. 15, pp. 733-742, 2012.

[28] S. J. Miley, "A Catalog of Low Reynolds Number Airfoil Data For Wind Turbine Applications," U.S. Department of Energy, 1982.

[29] F. Maganga, G. Pinon, G. Germain and E. Rivoalen, "Wake Properties Characterization of marine Current Turbines," in *ICOE*, Bilbao, 2010.

[30] A. S. Bahaj, L. E. Myers, R. I. Rawlinson-Smith and M. Thompson, "The effect of Boundary Proximity Upon the Wake Structure of Horizontal Axis Marine Current Turbines," *Journal of Offshore Mechanics and Arctic Engineering*, vol. 134, pp. 1-8, 2012.

[31] H. C. Buckland, I. Masters, J. A. Orme and T. Baker, "Cavitation Inception and Simulation in Blade Element Momentum Theory for Modeling Tidal Stream Turbines," *Journal of Power and Energy*, pp. 1-7, 2013.

[32] "Evaluation of Measurement Data - Guide to the Expression of Uncertainty in Measurement," Joint Committee for Guides in Metrology, 2008.

[33] C. Ratcliffe and B. Ratcliffe, Doubt-Free Uncertainty in Measurement: An Introduction for Engineers and Students, Springer, 2014.

[34] R. G. Dean and R. A. Dalrymple, Water Wave Mechanics for Engineers and Scientists, 2nd Edition, River Edge: World Scientific Publishing Co. Pte. Ltd., 1991.

[35] N. Barltrop, K. S. Varyani, A. Grant, D. Clelland and X. P. Pham, "Investigation into wave-current interactions in marine current turbines," *Journal of Power and Energy*, vol. 221, pp. 221-233, 2007.

[36] P. W. Galloway, L. E. Myers and A. S. Bahaj, "Studies of a scale tidal turbine in close proximity to waves," in *ICOE*, Bilbao, 2010.

[37] B. Gaurier, P. Davies, A. Deuff and G. Germain, "Flume Tank Characterization of Marine Current Turbine Blade Behavior Under Current and Wave Loading," *Renewable Energy,* vol. 59, pp. 1-12, 2013.

[38] L. Luznik, K. A. Flack, E. E. Lust and K. Taylor, "The Effect of Surface Waves on the Performance Characteristics of a Model Tidal Turbine," *Renewable Energy,* vol. 58, pp. 108-114, 2013.

[39] T. A. deJesus-Henriques, T. S. Hedges, I. Owen and R. J. Poole, "The Influence of Blade Pitch Angle on the Performance of a Model Horizontal Axis Tidal Stream Turbine Operating Under Wave-Current Interaction," *Energy,* vol. 102, pp. 166-175, 2016.

[40] I. A. Milne, A. H. Day, R. N. Sharma and R. G. Flay, "Blade Loads on Tidal Turbines in Planar Oscillatory Flow," *Ocean Engineering,* vol. 60, pp. 163-174, 2013.

[41] L. Luznik, R. Durka, W. A. Nimmo-Smith, W. Zhu, J. Katz and T. R. Osborn, "Distribution of Energy Spectra, Reynolds Stresses, Turbulence Production, and Dissipation in a Tidally Driven Bottom Boundary Layer," *Journal of Physical Oceanography,* vol. 37, pp. 1527-1550, 2007.

[42] J. S. Bendat and A. G. Piersol, Random Data: Analysis and Measurement Procedure, 2nd Ed., West Sussex: John Wiley & Sons Ltd, 1986.

[43] N. E. Huang, Z. Shen, S. R. Long, M. C. Wu, H. H. Shih, Q. Zheng, N. Yen, C. C. Tung and H. H. Liu, "The Empirical Mode Decomposition and the Hilbert Spectrum for Nonlinear and Non-Stationary Time Series Analysis," *Proceedings of the Royal Society of London A: Mathematical, Physical, and Engineering Sciences,* vol. 454, no. 1971, pp. 903-995, 1998.

[44] N. E. Huang, Z. Shen and S. R. Long, "A New View of Nonlinear Water Waves: the Hilbert Spectrum 1," *Annual Review of Fluid Mechanics,* vol. 31, no. 1, pp. 417-457, 1999.

[45] L. P. Chamorro, D. R. Troolin, S.-J. Lee, R. Arndt and F. Soiropoulos, "Three-Dimensional Flow Visualization in the Wake of Miniature Axial-Flow Hydrokinetic Turbine," *Experiments in Fluids,* vol. 54, no. 2, pp. 1459-1476, 2013.

[46] I. V. Naumov, V. V. Rahmanov, V. L. Okulov, C. M. Velte, K. E. Meyer and R. F. Mikkelsen, "Flow Diagnostics Downstream of a Tribladed Rotor Model," *Thermophysics and Aeromechanics,* vol. 19, no. 2, pp. 171-181, 2012.

[47] V. L. Okulov, I. Naumov, I. Kabardin, R. Mikkelsen and J. N. Sorensen, "Experimental Investigation of the Wake Behind a Model of Wind Turbine in a Water Flume," *Journal of Physics: Conference Series,* vol. 555, no. 1, 2014.

[48] S. C. Tedds, L. Owen and R. J. Poole, "Near-Wake Characteristics of Model Horizontal Axis Tidal Stream Turbine," *Renewable Energy,* vol. 63, pp. 222-235, 2014.

[49] L. P. Chamorro, C. Hill, S. Morton, C. Ellis, R. Arndt and F. Sotiropoulos, "On the Interaction Between a Turbulent Open Channel Flow and an Axial-Flow Turbine," *Journal of Fluid Mechanics,* vol. 716, pp. 658-670, 2013.

[50] F. Maganga, G. Germain, J. King, G. Pinon and E. Rivoalen, "Experimental Characterisation of Flow Effects on Marine Current Turbine Behaviour and on its Wake Properties".

[51] P. Mycek, B. Gaurier, G. Germain, G. Pinon and E. Rivoalen, "Experimental Study of the Turbulence Intensity Effects on Marine Current Turbines Behaviour. Part I: One Single Turbine," *Renewable Energy,* vol. 66, pp. 729-746, 2014.

[52] L. E. Lignarolo, D. Ragni, F. Scarano, C. J. Simao Ferreira and G. van Bussel, "Tip-Vortex Instability and Turbulent Mixing in Wind-Turbine Wakes," *Journal of Fluid Mechanics,* vol. 781, pp. 476-493, 2015.

[53] M. Sherry, A. Nemes, D. Lo Jacono, H. M. Blackburn and J. Sheridan, "The Interaction of Helical Tip and Root Vortices in a Wind Turbine Wake," *Physics of Fluids,* vol. 25, no. 11, 2013.

[54] S. E. Widnall, "The Stability of a Helical Vortex Filament," *Journal of Fluid Mechanics,* vol. 54, no. 4, pp. 641-663, 1972.

[55] M. Felli, R. Camussi and F. Di Felice, "Mechanisms of Evolution of the Propeller Wake in the Transition and Far Fields," *Journal of Fluid Mechanics,* vol. 682, pp. 5-53, 2011.

[56] L. Lignarolo, D. Ragni, C. Krishnawami, Q. Chen, C. J. Simao Ferreira and G. van Bussel, "Experimental Analysis of the Wake of a Horizontal-Axis Wind Turbine Model," *Renewable Energy,* vol. 70, pp. 31-46, 2014.

[57] S. B. Pope, Turbulent Flows, New York: Cambridge University Press, 2000.

[58] W. C. Reynolds and A. Hussain, "The Mechanics of an Organized Wave in Turbulent Shear Flow. Part 3: Theoretical Models and Comparisons with Experiments.," *Journal of Fluid Mechanics,* vol. 54, no. 2, pp. 263-288, 1972.

[59] A. Sciacchitano, B. Wieneke and F. Scarano, "PIV Uncertainty Quantification by Image Matching," *Measurement Science Technology,* vol. 24, pp. 1-16, 2013.

[60] A. Nemes, M. Sherry, D. Lo Jacono, H. M. Blackburn and J. Sheridan, "Evolution and Breakdown of Helical Vortex Wakes Behind a Wind Turbine," *Journal of Physics: Conference Series,* vol. 555, no. 1, 2014.

[61] J. Zhou, R. J. Adrian, S. Balachandar and T. M. Kendall, "Mechanisms for Generating Coherent Packets of Hairpin Vortices in Channel Flow," *Journal of Fluid Mechanics,* vol. 387, pp. 353-396, 1999.

[62] M. J. Bhagwat and M. Ramasamy, "Effect of Tip Vortex Aperiodicity on Measurement Uncertainty," *Experiments in Fluids,* vol. 53, no. 5, pp. 1191-1202, 2012.

[63] G. J. Leishman, Principles of Helicopter Aerodynamics, New York: Cambridge University Press, 2006, pp. 586-588.

[64] M. Ramasamy, R. Paetzel and M. J. Bhagwat, "Aperiodicity Correction for Rotor Tip Measurements," Army Research Development and Engineering Command, Aviation Aeroflight Dynamics Directorate, Moffett Field, 2011.

[65] M. Ramasamy, B. Johnson, T. Huismann and J. G. Leishman, "Digital Particle Image Velocimetry Measurements of Tip Vortex Characteristics Using and Improved Aperiodicity Correction.," *Journal of the American Helicopter Society,* vol. 54, no. 1, 2009.

[66] W. Batten, A. S. Bahaj, A. F. Molland and J. R. Chaplin, "Experimentally Validated Numerical Method for the Hydrodynamic Design of Horizontal Axis Tidal Turbines," *Ocean Engineering,* vol. 34, pp. 1013-1020, 2007.

[67] M. Ramasamy, B. Johnson and J. G. Leishman, "Turbulent Tip Vortex Measurements Using Dual-Plane Stereoscopic Particle Image Velocimetry," *The Journal of the American Institute of Aeronautics and Astronautics,* vol. 7, no. 8, pp. 1826-1839, 2009.

[68] L. Gui, J. Longo and F. Stern, "Towing Tank PIV Measurement System, Data and Uncertainty Assessment for DTMB Model 5512," *Experiments in Fluids,* vol. 31, pp. 336-346, 2001.

[69] R. Adrian and J. Westerwheel, Particle Image Velocimetry, Cambridge University Press, 2011.